INVESTIGATION OF STOCHASTICALLY EXCITED SUSPENSION SYSTEMS USING AN INERTIALLY NONLINEAR VIBRATION ABSORBER WITH ENERGY HARVESTING CAPABILITIES

Ву

Joel Cosner

A DISSERTATION

Submitted to
Michigan State University
in partial fulfillment of the requirements
for the degree of

Mechanical Engineering—Doctor of Philosophy

2025

ABSTRACT

The push towards electric vehicles in modern times is complemented by mobile and renewable power technology. In automotive vehicles, ride comfort and road handling are also important metrics to consider. Energy harvesting shock absorbers (EHSA) have potential, but traditional applications have resulted in tradeoffs between ride comfort, road handling, and power generation. Hence, research involving new technologies for power generation with multi-objective performance capabilities is very valuable. This work specifically investigates a novel approach for vibration suppression and electric power harvesting in systems subjected to stochastic and broadband excitations, focusing on automotive suspensions. The proposed solution harnesses the concept of inertance to provide mass amplification via rotational inertia and also introduces inertial nonlinearity, enhancing bandwidth and overall performance.

This work specifically explores vibration suppression, energy transfer, and the qualitative change in the probability density function (PDF) with the application of a device with nonlinearity due to inertia. This device is an inerter-based pendulum vibration absorber (IPVA). The change in the PDF is called P-bifurcation. The IPVA is first applied to a single-degree-of-freedom (SDOF) spring-mass-damper system subjected to white noise excitation. A perturbation method identifies and tracks bifurcation points, revealing that the marginal PDF of the pendulum's angular displacement undergoes a P-bifurcation, transitioning from monomodal to bimodal behavior. A cumulant-neglect technique predicts the system's mean squares, demonstrating significant vibration suppression near the P-bifurcation by transferring kinetic energy from the structure to the pendulum. Results are validated via Monte Carlo simulations (MCS), approximating the PDF and mean squares.

The study extends to integrating energy harvesting into the nonlinear device, applying it to a quarter-car model under class C road conditions (average road, ISO 8608). The impact of pendulum length on power generation, ride comfort, and road handling is assessed. Near P-bifurcation, simultaneous enhancements are seen in power output (40%), ride comfort

(60%), and road handling (60%) compared to a linear benchmark. A Wiener path integration (WPI) method predicts the PDF and its second derivative, enabling efficient detection of monomodal, bimodal, and rotational PDF regions in the noise intensity-electrical damping plane. MCS confirm performance improvements of up to 43% in energy transfer and 20% in power harvested compared to optimized linear systems, alongside at least 59% gains in ride comfort and road handling. A novel bifurcation detection algorithm reduces computational demands by linking qualitative PDF changes to performance metrics.

Experimental studies verify P-bifurcation and the energy harvesting IPVA's effectiveness in vibration reduction and energy harvesting for a SDOF structure under Gaussian broadband base excitation. Various experimental scenarios help identify unknown mathematical model parameters, minimizing discrepancies between experimental and simulated results for the pendulum's velocity, with all RMS velocity differences below 3%. The fitted model predicts power, vibration suppression, and P-bifurcation boundaries in the noise intensity-electrical damping plane, corroborated experimentally. Power spectral density analyses reveal bimodal and rotational systems outperform monomodal configurations, enhancing power and suppressing resonant peaks by up to factors of four and two, respectively. Near resonance, mean square relative velocity improves by a factor of two.

These findings inform the design and manufacture of a full-scale IPVA-integrated EHSA for off-road vehicles. The shock design involves balancing durability, weight, ride comfort, energy harvesting, and road handling. The shock absorber undergoes sinusoidal testing on a hydraulic machine to fit a developed mathematical model. A nonlinear least-squares based optimization routine fits model parameters, yielding two viable parameter sets. Numerical simulations implement the shock in a quarter car model with class F road excitation (off-road; ISO 8608) and quantify energy harvesting, ride comfort, and road handling. A correlation between performance and the PDF shape is finally made.

ACKNOWLEDGEMENTS

I would like to thank my advisor Dr. Wei-Che Tai, committee (Dr. Dan Segalman, Dr. Zhaojian Li, Dr. Xiaobo Tan), lab peers (Aakash Gupta, Majid Baradaran Akbarzadeh, Guoxin Li, Jamal Ardister), and family/friends for their continued support and help during my PhD and for my professional development. Majid Baradaran Akbarzadeh also helped with the transportation and experimentation associated with the full-scale energy harvesting shock absorber. I would also like to acknowledge various undergraduate students who aided me in conducting successful experiments: Sean Lishawa, Max Weidemann, and Olivia Reyes.

TABLE OF CONTENTS

| CHAPTER 1 | INTRODUCTION | 1 |
|----------------|---|-----|
| CHAPTER 2 | ANALYSIS WITH THE NONLINEAR VIBRATION ABSORBER | 13 |
| CHAPTER 3 | ENERGY HARVESTING, RIDE COMFORT AND ROAD HANDLING IN AUTOMOBILE SUSPENSION SYSTEMS | 35 |
| CHAPTER 4 | AN EXPERIMENTAL STUDY: P-BIFURCATION, ENERGY HARVESTING, AND VIBRATION SUPPRESSION | 62 |
| CHAPTER 5 | FUTURE AND ONGOING WORK: AN EXPERIMENTAL STUDY WITH THE FULL-SCALE ENERGY HARVESTING SHOCK ABSORBER | 89 |
| BIBLIOGRAPHY | | 117 |
| APPENDIX A: DF | RIFT AND DIFFUSION COMPONENTS OF MOMENT EQUATIONS | 125 |
| APPENDIX B: CI | LOSURE TECHNIQUES | 127 |
| APPENDIX C: LI | NEAR SYSTEM RESPONSE | 129 |
| APPENDIX D: LI | NEAR SYSTEM RHI ANALYTICAL SOLUTION | 130 |
| APPENDIX E: DA | AMPING AND FRICTION FITTING IN THE TIME DOMAIN FOR THE SDOF SYSTEM EXPERIMENT | 132 |

CHAPTER 1

INTRODUCTION

1.1 Overview of the Work

This work seeks to provide a unique solution to how one might simultaneously achieve vibration suppression and harvest electric power when considering an underlying excitation that is naturally stochastic and broadband, i.e. randomly varying with a characteristically wide power spectral density (PSD) as applied to suspension systems. The solution at hand specifically involves a device that uses inertance to provide a mass amplification effect and inertial nonlinearity, which broadens the effective bandwidth of operation.

The development of a device that leverages inerter characteristics—utilizing rotational inertia instead of mass to minimize acceleration between two terminals [1]—fits well within automotive suspension systems, where vehicle size constraints are often inflexible. As further outlined in Section 1.2, the mass amplification accommodated by an inerter can provide a dramatic enhancement of vibration suppression capabilities when applied to structures with stochastic excitation, including vehicle suspension systems. This work specifically utilizes a ball screw inerter type.

As will be further discussed in Section 1.2.3, one of these inerters equipped with energy harvesting capabilities will generally fall short of providing optimal vibration suppression while simultaneously generating optimal power output, if a linear design is used. In the case of a vehicle suspension system, ride comfort and road handling may suffer simultaneously with electric power generation. Hence, in this work, a nonlinear design is used. The design chosen specifically accommodates nonlinear effects due to inertia rather than stiffness, utilizing a horizontally attached pendulum vibration absorber to the ball screw inerter device. The device is called the inerter pendulum vibration absorber (IPVA) and is coupled with a DC generator when energy harvesting is implemented. It will be shown that this IPVA accommodates random pendulum motion around more than one distinct position and with large jumps in between each position, giving a probability density function (PDF) with two

peaks (bimodal). This behavior resembles that of popular bistable harvesters with random broadband excitation found in literature such as in [2, 3, 4, 5] and [6], while those devices are stiffness based and more bulky and/or too complicated for vehicle suspension systems. Furthermore, the IPVA energy harvesting device is shown to accommodate superior vibration suppression and energy harvesting simultaneously, when compared to the comparable linear system.

Starting in Chapter 2 and thereafter, it is found that performance is linked deeply with the qualitative shape of the PDF. Performance is measured in terms of energy harvesting simultaneously with vibration suppression as applied to a single degree of freedom (SDOF) structure; as applied to a vehicle suspensions system using a quarter car model, performance is in terms of energy harvesting, ride comfort, and road handling. Hence, unique methods are developed to predict the phenomenological bifurcation involving a qualitative change in the number and locations of the local maxima of the PDF, P-bifurcation [7, 8]. P-bifurcation is further explained in Section 1.2.1.

The following details the organization of the culmination of this work hereinafter. This research is comprehensively motivated in Section 1.2. Then in Chapter 2 the IPVA is studied with applications involving a SDOF structure, comprised of a linear spring-mass-damper system subjected to white noise base excitation to quantify vibration suppression. The principle of stochastic bifurcation is explored with exciting connections between bifurcation criteria and optimal kinetic energy transfer between the structure and the pendulum.

In Chapter 3 the device is integrated into an automotive suspension system whereby a road profile defined by an ISO 8608 [9] standard power spectral density is used as the excitation. Energy harvesting, ride comfort, and road handling are quantitatively and qualitatively explored. The multi-objective performance is studied in conjunction with P-bifurcation of the PDF in an attempt to build a meaningful correlation between performance and bifurcation. A unique adaptation of the Wiener path integration (WPI) formulation originally outlined in [10] is augmented with a calculus of variations approach for the prediction of

P-bifurcation.

Finally, in Chapter 4, a culmination of the experimental work associated with the energy harvesting device applied to a SDOF system subjected to random broadband base excitation is presented and discussed in detail. The analytical treatment and simulation results of Chapter 2 directly motivate an abundance of experimental qualitative validation and quantitative verification which are presented in detail in Chapter 4. The experimental studies as well as the results of Chapter 3 further serve as a precursor to an experimental study of the full-scale inertially nonlinear Energy Harvesting Shock Absorber (EHSA) which is addressed in Chapter 5. The creative and unique experimental works coupled with the theoretical analysis are believed to solidify a significant and scientifically impactful doctoral thesis.

1.2 Motivation and Background

1.2.1 A P-bifurcation primer with literature suggestions

It is important to give further information on P-bifurcation for a more thorough understanding of the underlying theory associated with part of this work. Literature associated with stochastic dynamics such as [11], which provides an overview of the advancements in stochastic dynamics by the close of the twentieth century, defines P-bifurcation as qualitative changes in the stationary PDF and the related Markov process. For a more in-depth understanding of the mathematical methods used to examine P-bifurcations, one can refer to works such as [12], which compiles the stochastic dynamics literature from the late 20th century. A notable article in the text is one on P-bifurcation in the noisy Duffing-van der Pol equation [13]. The authors of this work noted that the random motion was fast in nature and occurred as random oscillations or rotations along the trajectories of the deterministic system. They further used this fact to justify the use of stochastic averaging [14] and then proceeded to derive the stationary PDF from the Fokker-Planck-Kolmogorov equation, where the FPE is a partial differential equation governing the PDF [15]. This allowed them to mathematically determine when the extrema in the PDF changed, indicating P-bifurcation. On the other hand, the authors in [16] begin by reviewing deterministic center manifold theory, utilizing

unfolding parameters to examine behavior around bifurcations such as Hopf, transcritical, and pitchfork types. They then derive the FPE and its solution near the center manifold to identify P-bifurcations. Analyses cover both additive noise, where noise is added to the state space; and multiplicative noise, where noise multiplies the states in the system. In addition to the aforementioned analysis methods, the authors of [17] mentioned the notion of bifurcations in the moment equations governing the statistical moments associated with the system [14, 15]. One analytical method employed in the current work involves detecting the change in stability of moment equation fixed points by determining when the determinant of the Jacobian vanishes. This method is detailed in Chapter 2 and used again in Chapter 4. Another analytical formulation is developed in this work which utilizes the WPI technique [18, 19, 20] and exploits knowledge of the curvature of the PDF at the bifurcation. The WPI method is detailed and used in Chapter 3.

1.2.2 Vibration mitigation application

The inerter is a mechanical device with two terminals, each of which exerts an equal and opposite inertial force proportional to the relative acceleration between the terminals [1]. The constant of proportionality in this case is known as the inertance. Furthermore, the transmission mechanism used by inerters commonly includes the ball screw [21] or rack-pinion [22]. These devices provide a means for conversion of linear translational motion into rotational motion. In this way, a light-weight object that rotates with the device may add an effective translational inertia manifested by the moment of inertia of the object instead of its mass. As a result, a well-chosen transmission ratio can provide an effect of mass amplification, multiplying the mass of the lightweight object by a factor of 10 or more. Therefore, the inerter is a favorable device for vibration suppression in many engineering structures and components.

Researchers have been attracted to inerters in the context of vibration mitigation involving broadband random excitation. For example, Marian and Giaralis [23] integrated the inerter with the classical tuned mass damper (TMD), known as the tuned mass damper

inerter (TMDI), to suppress the response of stochastically motion-excited structures. They concluded that the "mass amplification effect" of the inerter can enhance the performance of the classical TMD. Hu and Chen [24] proposed four types of inerter-based dynamic vibration absorber (IDVA) to suppress the response of linear spring-mass systems force-excited by white noise and evaluated their H_{∞} and H_2 performance compared with the classical TMD. Specifically, the proposed IDVAs incorporated a spring connected with the inerter in series or parallel, such that the inerter provided another degree of freedom to the DVA. They concluded that the additional degree of freedom is necessary to enhance the H_{∞} and H_2 performance and enlarge the effective frequency bandwidth of response suppression. Moreover, Joubaneh and Barry [25] studied the performance of four models of electromagnetic resonant shunt TMDI (ERS-TMDI) on both vibration suppression and energy harvesting and identified the best model. Their parametric studies showed that increasing the inertance enhances the performance of the best model in terms of both vibration mitigation and energy harvesting. On the other hand, Tai [26] integrated the inerter with a torsional mass damper, known as the tuned inerter-torsional-mass damper (TITMD), to suppress response of linear spring-mass-damper systems motion-excited by white noise. In comparison with the TMDI, the TITMD achieved 20-70% improvement in the H_2 performance when their weights were identical.

In this work, the IPVA is in fact a nonlinear dynamic absorber. Nonlinear dynamic vibration absorbers by virtue of inertial nonlinearity have been studied by many researchers to suppress vibration of structures. One specific class of nonlinear dynamic vibration absorbers, known as autoparametric vibration absorbers [27], utilize specific inertial nonlinearity to transfer the kinetic energy of a primary structure requiring reduced vibration to the vibration absorber when subject to harmonic excitation [28, 29, 30] and random excitation [31, 32]. By virtue of the energy transfer phenomenon, the autoparametric vibration absorbers have been shown to achieve vibration mitigation and energy harvesting at the same time [33, 34, 35, 36, 37].

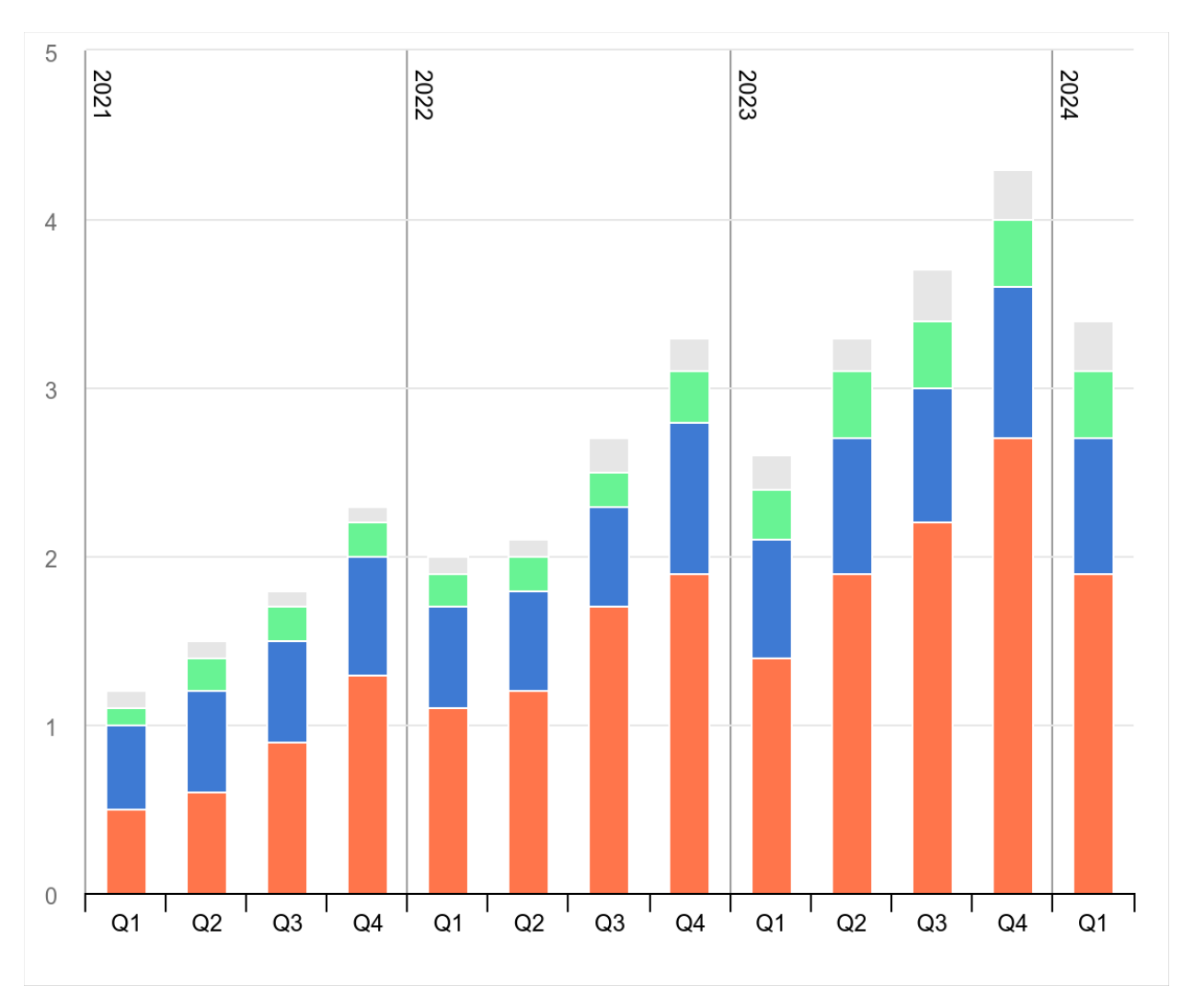


Figure 1.1 Electric vehicle quarterly sales for the years 2021-2024 in millions. The y-axis is the quantity in millions. Orange is China, blue is Europe, green is the United States, and grey is the rest of the world. The chart was taken from the International Energy Agency (IEA) [38].

1.2.3 Energy harvesting considerations

The International Energy Agency (IEA) reported quarterly sales for 2021-2024 and the result is shown in Fig. 1.1. In subsequent years a clear monotonically increasing trend is seen. The IEA specifically note a 25% increase from Q1 in 2023 to Q1 in 2024. This growth is substantiated by the fact that 2023 had a record-breaking 14 million electric vehicles sold, or 18% of all vehicles sold [39]. Furthermore, the International Council on Clean Transportation (ICCT) has reported governments that intend to phase out vehicles that are not zero-emissions by a designated year [40] and this is shown in the map of Fig. 1.2. This



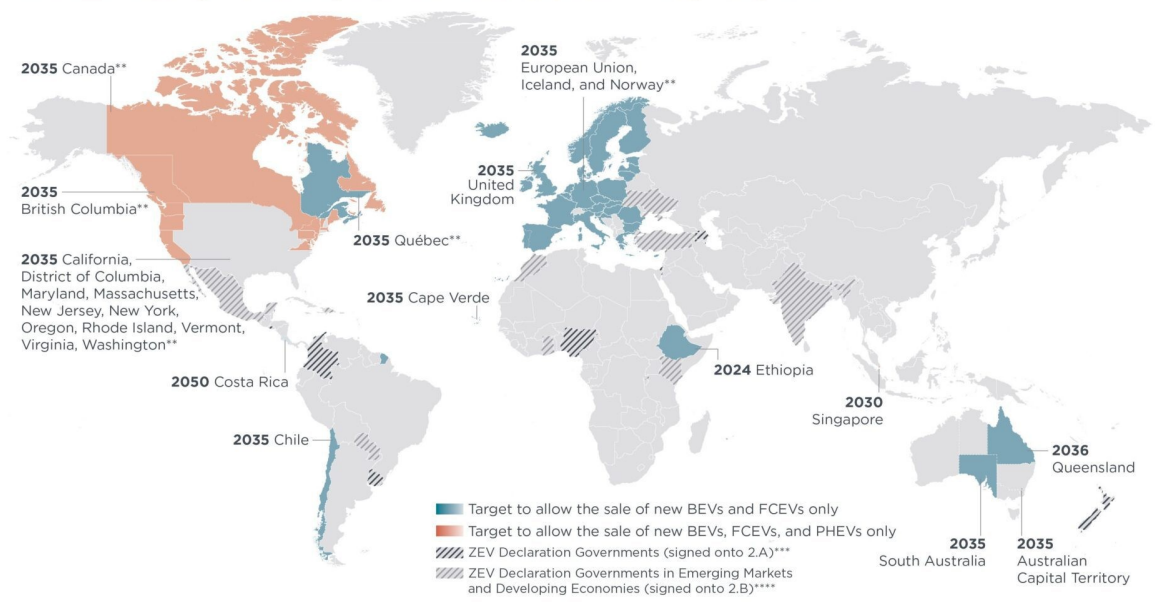


Figure 1.2 Governments with targets to only sell zero-emission vehicle by a certain date [38].

phasing out process can be coined "electrification" of the automotive industry. This "electrification" serves as motivation for research in efficient power generation in electric vehicles in order to accommodate less stringent battery charging and energy storage requirements. Other needs for efficient energy harvesting in vehicles can be realized in cases when the military wishes to remain untethered to power grids and energy independent in expeditionary environments. Energy harvesting shock absorbers (EHSAs), researched for decades for the purpose of converting vibration energy into electrical power [41, 42], could be of significant use to electrical vehicle manufacturers as well as the military as they can effectively act as a mobilized power resource. A recent review of research in the field suggests a significant power generation potential for varying degrees of road classes from ISO 8608.[43].

Recent research in the field of small-scale energy harvesting has given promise to the use of bi-stable systems to enhance energy harvesting; see the extensive reviews of [44, 45]. Other recent examples exist such as in [4], where the authors designed an electromagnetic energy harvester device with stiffness nonlinearity due to the geometry of the configuration which was shown to outperform the corresponding linear device with filtered and band-limited

stochastic excitation. Overall, while much research progress has been made regarding bistable harvesters, stiffness nonlinearities are unfortunately not easy to implement or practical in the case of vehicle suspension systems.

To understand the importance of nonlinearity in EHSAs, it is crucial to look at the abundance of research in traditional EHSA designs [46, 47, 48]. Traditional linear designs [49, 50, 51, 52] cannot achieve optimal vibration suppression and power harvesting simultaneously. In fact, research shows that linear designs trade suspension performance for energy recovery [50, 51, 52]. Additionally, peak energy harvesting performance lies in the narrowband linear resonance regime [53] whereas road irregularities are stochastic and broadband in nature [54]; hence, road tests have frequently reported unsatisfactory and unsteady energy recovery efficiency of linear EHSA designs [43]. Performance degradation in linear suspension systems when purposed to harvest energy has motivated research efforts in regard to bistable suspension systems.

One significant feature of bistable systems which contributes to improved energy harvesting has been identified as the frequent transitions between potential wells, also known as interwell oscillation [2, 3, 5]. When interwell oscillations are permitted, the multi-stability in energy harvesters in the case of random excitation manifests itself as a multimodal (multiple peaks) PDF associated with the states of the system [4, 55, 56]. As such, analysis often involves obtaining the PDF by solving the FPE with the finite element method [56, 57] or by obtaining an approximation with the WPI method [10, 18, 19, 58]. Otherwise, statistical moment equations governing the system's statistics can also be derived [59, 60] as another means of analysis. A Monte Carlo simulation (MCS) is then often used for verification purposes [58, 60, 61, 62], which allows for the determination of the necessary statistics with direct numerical simulation.

The device introduced in Chapter 2 is a specific device which in lieu of stiffness nonlinearities harnesses inertial nonlinearity and accommodates bimodality. This device is studied with stochastic excitation and it will be found that when the PDF of the system undergoes a

bifurcation from monomodal to bimodal, meaning that two equally probable equilibria exist, an energy transfer occurs between the structure and the pendulum. To this end, this energy transfer is responsible for mitigating vibrations of the structure, while the energy in the pendulum is also increased. While energy harvesting is not incorporated yet in Chapter 2, the energy transfer found serves to motivate transferring the energy to the electrical domain in an energy harvesting context.

In [62], the IPVA device was further explored when the device was implemented in a quarter-car model suspension system whereby it was used in conjunction with a planetary gear system to successfully drive a generator while simultaneously optimizing ride comfort. The authors in [62] determined that the nonlinear device outperformed the linear EHSA with an increase in power of 45% and a 45% reduction in the root-mean-square (RMS) acceleration of the sprung mass. An exhaustive Monte Carlo simulation (MCS) was used to discover and illustrate these findings. It is the intent in Chapter 3 to return attention to the quarter car model with increased suspension stiffness to accommodate off-road vehicle simulation, but this time investigate the system using knowledge of stochastic P-bifurcation [63]. While this is explored in Chapter 3, it is not a trivial task. Due to the cost of computing the PDF, Pbifurcation analysis has focused on systems with five or fewer state variables, [64, 65, 66] for example. Additional research investigating stochastic bifurcation and analytical formulations for the PDF has been done such as in [55, 67]. However, these approaches unfortunately rely on the stochastic averaging approach. The method of stochastic averaging can only produce accurate results in the case of weak excitation and weak nonlinearity, allowing one to assume a slow varying response [15]. As the suspension system has more states and weak excitation and nonlinearity cannot be assumed, an effective analysis approach remains open. To that end, an analytical formulation is developed in this work which utilizes the WPI technique [18, 19, 20] and exploits knowledge of the curvature of the PDF at the bifurcation.

The research surrounding the multi-objective performance capabilities of the nonlinear IPVA when subjected to random excitation such as in [58, 62] is very relevant to modern

research. As pointed out in a recent review of dual-objective harvesters [68], the research surrounding the use of nonlinearity to achieve multi-objective performance is still scarce. It is even more scarce when considering excitation which is stochastic in nature. The research that does exist is often associated with the longtime running research topic of nonlinear energy sinks (NES) [69] which inherently require cubic stiffness nonlinearity via the use of elastic components or magnetic arrangements. For example, the researchers in [70] theoretically coupled an NES with a giant magnetostrictive energy harvester (GMEH) and applied the device to a single degree of freedom structure subjected to Gaussian white noise excitation to achieve energy harvesting and vibration suppression objectives simultaneously. Regardless, the current work avoids stiffness nonlinearities which could make the system too bulky and impractical if applied to an automobile suspension system.

1.2.4 Experimental Investigations of Bimodal Energy Harvesting Systems with Broadband Random Excitation

The experimental exploration of bi-stable energy harvesters subjected to random excitation has accompanied much of the research in this particular field. For example, in [2] the authors qualitatively verified simulation results for a Duffing-type harvester subjected to band-limited noise excitation, investigating how the center frequency and the bandwidth of the excitation affected the output voltage in the mono-stable and bi-stable configurations. In [3], the researchers experimentally validated simulation results for a bi-stable energy harvester under band-limited white noise excitation which was transformed into a flexible bi-stable energy harvester exhibiting a variable potential energy function due to a magnet on a flexible beam. Similarly, in [4] the authors experimentally validated simulation results for a bi-stable two-degree-of-freedom harvester system and investigated the effect of varying excitation intensity, bandwidth, and center frequency. Likewise, in [5] the authors explored and experimentally validated the theoretical results for a piezoelectric bi-stable harvester subjected to wide-band random excitation, while varying excitation intensity and the separation between equilibrium positions. In short, [2, 3, 4, 5] and others like [6] all share a

common conclusion: bi-stable energy harvesting systems will outperform mono-stable counterparts under broadband random excitation precisely when the excitation is large enough to produce interwell oscillations and they all experimentally validate or verify their theoretical results. Nevertheless, prediction of the parameter values required for interwell oscillations has remained open thus far.

To understand when multiple peaks in the PDF can occur, or equivalently when interwell motion capabilities change for multi-stable systems, one can understand P-bifurcations which was discussed in the end of Sec. 1.2.2. Some approaches in the past to study bifurcations have included the numerical computation of the PDF with the finite element method [57] or deriving estimates for the PDF [57, 64, 65, 66], which have been computationally limited to systems with less than five states. Then [71] employed a technique based on Shannon Entropy, whereas this study introduces a WPI-based PDF approximation algorithm tailored for a system with seven states, as detailed in Chapter 3. With that being said, to the author's knowledge, no openly available research attempts to predict P-bifurcation pertaining to experiments with wide-band random excitation. Lastly, while many researchers have remedied interwell oscillation difficulties by studying tri-stable [72, 73] or even quad-stable [74] energy harvesters to boost energy harvesting efficiency, it is hypothesized from evidence in [62] and is shown in Chapters 2 and 3 of this work that by using inertial nonlinearity rather than stiffness nonlinearity, a bimodal PDF can still be produced without a multistable potential and is often associated with large amplitudes of oscillation just as in multi-stable systems with interwell motion. Chapter 4 exploits such a system and seek to predict changes in the number of peaks in the PDF in experiments, indicating when the large amplitude oscillations may occur.

Chapter 4 focuses on the bimodal IPVA energy harvesting device applied to an SDOF structure subjected to Gaussian broadband excitation. The objective is to experimentally investigate P-bifurcation of the PDF and the correlation with simultaneous energy harvesting and vibration suppression. Notably, this study will include the experimental parameter char-

acterization for a developed prototype to accommodate accurate predictions of energy harvesting potential, vibration suppression, and bifurcation boundaries. Adequate experimental data will be used to verify predictive capabilities, confirm the bifurcation phenomenon, and gather information regarding power harvested and vibration suppression.

CHAPTER 2

ANALYSIS WITH THE NONLINEAR VIBRATION ABSORBER

2.1 Introduction

In this chapter, we conduct a P-bifurcation analysis of a linear spring-mass-damper system (primary structure) incorporating the IPVA, which has white noise base excitation, made to an equivalent force excited system. The qualitative change in the number and locations of the maxima of the probability density function (PDF) is thereby examined as well as the correlation between P-bifurcation and kinetic energy transfer of the linear system to the pendulum.

The chapter is organized as follows. In Sec. 2.1.1, the stochastic differential equations of the structure-IPVA system are derived. In Sec. 2.2, stochastic bifurcation is investigated while implementing a bifurcation detection and tracking procedure. Numerical validation including realizations in the time domain is imposed with the aid of a Monte Carlo simulation, while an arc-length continuation scheme is developed to track bifurcation points as a function of parameters. Energy transfer from the primary structure to the pendulum is investigated in the neighborhood of bifurcation with the use of a cumulant-neglect procedure. Furthermore, the relationship between the energy transfer and vibration mitigation is investigated. In Sec. 2.3, a parametric study is conducted to study the system at bifurcation while varying pendulum length, mass ratio, noise intensity, and pendulum damping ratio. A discussion is then given in Sec. 2.4. Finally, this chapter will serve as a prelude to applications in automobile suspension systems.

2.1.1 The Inerter Pendulum Vibration Absorber

The design of the IPVA is shown in Fig. 2.1. The IPVA is attached between the ground and a linear oscillator (primary structure) of mass M, stiffness k, and damping c. Linear motion x of the mass is converted to angular motion θ of the ball screw with effective radius $R = L/2\pi$, where L refers to the lead value associated with the ball screw as a measure of

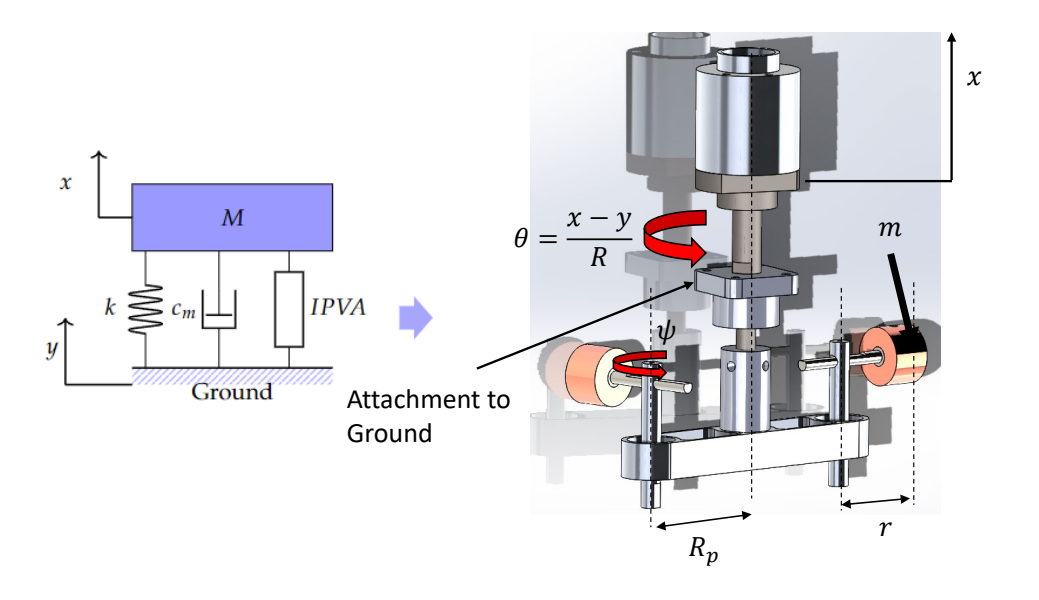


Figure 2.1 Schematic of IPVA attached to a structure of mass (M) with defined degrees of freedom θ , and ψ . The second pendulum on the left is assumed to be fixed.

the ratio of linear displacement of the nut to full rotation of the screw. More specifically, $x = R\theta$. A pendulum, of length r and mass m, is also attached perpendicular to the screw, at a radius of R_p from the center of the screw and with an angular displacement of ψ with respect to the attachment point. Note that two pendulums are shown, but one is to be fixed in place to avoid rotating unbalance. The free pendulum will oscillate and absorb energy from the primary structure, with varying magnitudes of energy transfer dependent on the parameter values of the system. F corresponds to the forcing applied to the structure, and in the present work it is defined to be a Gaussian white noise with zero mean and standard deviation $\Gamma = \sqrt{2S}$, where S is the noise intensity. In the sections that follow, we will attempt to quantitatively and qualitatively describe the effect of parameter variation of this IPVA on the bifurcation of the probability density function as well as the relationship with vibration suppression.

To derive the equations of motion using Lagrange's equations, we first derive the kinetic energy, potential energy, and virtual work associated with the system. The kinetic energy for the system is given by

$$T = \frac{1}{2} \left[M(\dot{x} + \dot{y})^2 + J\dot{\theta}^2 + \left(J_p + mr^2 \right) \left(\dot{\psi} + \dot{\theta} \right)^2 + m \left(R_p^2 \dot{\theta}^2 + 2R_p r \cos(\psi) \dot{\theta} \left(\dot{\theta} + \dot{\psi} \right) \right) \right]$$

$$(2.1)$$

where $(\cdot) = d(\cdot)/dt$ represents the first time derivatives, and J and J_p correspond to the moment of inertia about the axis of rotation of the screw and the pendulum, respectively. The potential energy is given by

$$V = \frac{1}{2}k\left(R\theta\right)^2\tag{2.2}$$

Furthermore, a torsional viscous damping coefficient c_p is introduced to account for energy loss at the pivot point of the pendulum. The virtual displacement of the mass is given by $\delta x = R\delta\theta$ and the virtual displacement of the pendulum in the direction of the pendulum damping torque is $\delta\psi$. It follows that the summed virtual work due to the mechanical damping of the primary structure motion as well as pendulum motion is written as

$$\delta Q = -cR^2 \dot{\theta} \delta \theta - c_p \dot{\psi} \delta \psi \tag{2.3}$$

With (2.1), (2.2) and (2.3), the equations of motion for the system were derived and are given here.

$$(MR^{2} + J + mR_{p}^{2} + J_{p} + mr^{2} + 2mR_{p}r\cos(\psi))\ddot{\theta} + (mr^{2} + mR_{p}r\cos(\psi) + J_{p})\dot{\psi}$$

$$+cR^{2}\dot{\theta} + kR^{2}\theta - 2mR_{p}r\dot{\psi}\dot{\theta}\sin(\psi) - mR_{p}r\sin(\psi)\dot{\psi}^{2} = F(t)R,$$

$$(mr^{2} + J_{p})\ddot{\psi} + (J_{p} + m(r^{2} + R_{p}r\cos(\psi)))\ddot{\theta} + c_{p}\dot{\psi} + mR_{p}r\sin(\psi)\dot{\theta}^{2} = 0.$$
(2.4)

where the base excitation is converted to direct forcing mathematically via $F(t) = -M\ddot{y}$.

In (4.6), $(\dot{\bullet}) = d^2(\bullet)/dt^2$ represent the second time derivatives. Let us now define \hat{M} as the effective structural mass. It then follows that $MR^2 + J = (M + \frac{J}{R^2})R^2 = \hat{M}R^2$. Thus, the moment of inertia term J can be absorbed into the effective mass term with the inertial addition given by the inertance J/R^2 . Evidently, for small R, mass amplification is large.

Next note that the pendulum shaft moment of inertia J_p is also negligible relative to the inertia $\hat{M}R^2$ and so it can be set to zero without any noticeable change in the resulting dynamics. Next, $\psi = \phi + \phi_0$, where ϕ_0 corresponds to an offset pendulum angle and ϕ is the angular displacement with respect to ϕ_0 .

To facilitate a parametric study, the following dimensionless parameters were appropriately chosen.

$$\mu_r = \frac{mR_p^2}{\hat{M}R^2}, \ \omega_0 = \sqrt{\frac{k}{\hat{M}}}, \ \eta = \frac{r}{R_p}, \ \xi = \frac{c}{2\hat{M}\omega_0}, \ \xi_p = \frac{c_p}{2\hat{M}R^2\omega_0}$$

$$\tau = \omega_0 t, \ \dot{(\cdot)} = \omega_0 (\cdot)', \ \ddot{(\cdot)} = \omega_0^2 (\bullet)''$$

$$(2.5)$$

The equations of motion for the system are then rewritten in terms of the dimensionless parameters as follows:

$$\mathbf{M}(\psi)\mathbf{x}'' + \mathbf{C}\mathbf{x}' + \mathbf{K}\mathbf{x} + \mathbf{g}(\mathbf{x}, \mathbf{x}') = \mathbf{f}$$
(2.6)

where

$$\mathbf{M}(\psi) = \begin{bmatrix} 1 + \mu_r (1 + \eta^2 + 2\eta \cos(\psi)) & \mu_r \eta (\eta + \cos(\psi)) \\ \mu_r \eta (\eta + \cos(\psi)) & \mu_r \eta^2 \end{bmatrix},$$

$$\mathbf{C} = \begin{bmatrix} 2\xi & 0 \\ 0 & 2\xi_p \end{bmatrix}, \mathbf{K} = \begin{bmatrix} 1 & 0 \\ 0 & 0 \end{bmatrix}, \mathbf{f} = \begin{pmatrix} W(\tau) \\ 0 \end{pmatrix},$$

$$\mathbf{g}(\mathbf{x}, \mathbf{x}') = \mu_r \eta \begin{pmatrix} -(2\psi'\theta' + \psi'^2)\sin(\psi) \\ \theta'^2\sin(\psi) \end{pmatrix}$$
(2.7)

In (3.2) and (2.7), $\mathbf{x} = (\theta, \psi)^T$, \mathbf{M} is the inertia matrix which is inherently nonlinear due to the Euler acceleration as a result of a rotating reference frame, \mathbf{C} is the damping matrix, \mathbf{K} is the stiffness matrix, and the vector \mathbf{f} is associated with stochastic forcing. The force term $W(\tau) = F(\tau)/\hat{M}R\omega_0^2$ is then defined to be the normalized Gaussian white noise with zero mean and noise intensity D, while ξ and ξ_p are the damping ratios associated with the structure and the pendulum respectively. Furthermore, \mathbf{g} represents the nonlinear Coriolis and centrifugal terms.

Note that the equations of motion are written in terms of the normalized time variable, τ . Any temporal results obtained will thus be on a time scale of τ . The current study is primarily associated with the response characteristics of the system as a function of η and μ_r . The value of η is a measure of the pendulum length, while μ_r is proportional to the pendulum-structure mass ratio. Both parameters quantify the nonlinear coupling associated with the system as can be seen upon inspection of \mathbf{g} .

To appropriately analyze the system with stochastic forcing, the equations of motion (3.2) are transformed into the Itô stochastic differential form [31, 75] as follows.

$$d\mathbf{y} = \mathbf{a}(\mathbf{y}) d\tau + \mathbf{\Sigma}(\mathbf{y}, \tau) dB \tag{2.8}$$

where

$$d\mathbf{y} = \begin{pmatrix} dy_1 \\ dy_2 \\ dy_3 \\ dy_4 \end{pmatrix} = \begin{pmatrix} d\theta \\ d\psi \\ d\dot{\theta} \\ d\dot{\psi} \end{pmatrix}$$

and B is a scalar zero-mean and delta-correlated Wiener vector process, with $\langle dB(\tau) \rangle = 0$ and $\langle dB(\tau)dB^{T}(\tau) \rangle = 2Dd\tau$, where $\langle \cdot \rangle$ represents the expectation operator and D is the noise intensity. Additionally, \mathbf{a} and $\mathbf{\Sigma}$ are a 4×1 drift vector and diffusion vector, respectively, namely

$$\mathbf{a}(\mathbf{y}) = -\begin{bmatrix} \mathbf{0}_{2\times2} & \mathbf{I} \\ \mathbf{M}^{-1}\mathbf{K} & \mathbf{M}^{-1}\mathbf{C} \end{bmatrix} \mathbf{y} - \begin{pmatrix} \mathbf{0}_{2\times1} \\ \mathbf{M}^{-1}\mathbf{g}(\mathbf{x}, \mathbf{x}') \end{pmatrix}$$

$$\Sigma(\mathbf{y}, \tau) = \begin{bmatrix} \mathbf{0}_{2\times2} \\ \mathbf{M}^{-1} \end{bmatrix} \begin{pmatrix} \sqrt{2D} \\ 0 \end{pmatrix}$$
(2.9)

The explicit forms of \mathbf{a} and Σ are given in Appendix A.

2.2 Stochastic Bifurcation

It is known that the pendulum may oscillate with respect to a nonzero equilibrium point when subject to harmonic excitation [76]. If such asymmetric oscillations exist when subject to random excitation, these asymmetric oscillations correspond to a nonzero mean response and indicate a change in the locations (and likely the number) of the maxima of the PDF. It is shown in Sec. 2.2.3 that such P-bifurcation indeed exists in the system and leads to a transfer of the kinetic energy of the primary structure to the pendulum.

2.2.1 Bifurcation Detection and Tracking

P-bifurcations of highly nonlinear systems are commonly predicted in the literature by computing the PDF with numerical techniques, such as the cell mapping method [7], the finite difference method [8], and the path integration method [77]. The computational cost of these methods are dependent on the number of the state variables, and can be too expensive when applied to the current system of four state variables. A perturbation method is employed instead in this work to detect and track the P-bifurcation of the system, which is based on the following principle in random vibration. It is known that when a linear oscillator is subject to zero-mean Gaussian white noises, the response is zero-mean Gaussian [78]. This implies that when subject to zero-mean Gaussian white noises, the response of a linearized nonlinear oscillator is zero-mean Gaussian with respect to a local maximum of the PDF because that is where the response spends relatively much time [79]. In other words, if the equations of motion (2.8) is linearized with respect to a local maximum, the response of the linearized system should be zero-mean. Linearization of (2.8) will nevertheless lead to a degenerate stiffness matrix because the pendulum lacks any stiffness terms, which will incur computational difficulties. A perturbation method is therefore applied to (2.8), instead of linearization, which is explained as follows. Because only asymmetric oscillation of the pendulum is of interest, a small perturbation $\phi = \psi - \phi_0$ is introduced to (2.8), where $|\phi| \ll 1$ and ϕ_0 represents the location of an unknown local maximum to be determined. After expanding with respect to ϕ_0 and retaining only linear terms of ϕ , one arrives at

$$d\hat{\mathbf{y}} = \hat{\mathbf{a}}(\hat{\mathbf{y}}, \phi_0) d\tau + \hat{\mathbf{\Sigma}}(\hat{\mathbf{y}}, \phi_0, \tau) dB$$
(2.10)

where $\hat{\mathbf{y}} = (\theta, \phi, \theta', \phi')^{\mathrm{T}}$ and

$$\hat{\mathbf{a}}(\hat{\mathbf{y}}, \phi_0) = \left[\mathbf{a}(\mathbf{y}) + \left(\frac{\partial \mathbf{a}(\mathbf{y})}{\partial \psi}\right) \phi\right]_{\psi = \phi_0}$$

$$\hat{\mathbf{\Sigma}}(\hat{\mathbf{y}}, \phi_0, \tau) = \left[\mathbf{\Sigma}(\mathbf{y}, \tau) + \left(\frac{\partial \mathbf{\Sigma}(\mathbf{y}, \tau)}{\partial \psi}\right) \phi\right]_{\psi = \phi_0}$$
(2.11)

Because (2.10) governs small oscillation in the neighborhood of a local maximum, the mean value $\langle \hat{\mathbf{y}} \rangle$ should be approximately zero. In other words, one can use (2.10) to find a nontrivial ϕ_0 such that $\langle \hat{\mathbf{y}} \rangle = 0$. To this end, the stationary moment equations of (2.10) are derived. Specifically, a moment generating function $m_{pqrs} = \langle y_1^p y_2^q y_3^r y_4^s \rangle$ up to order n = 2 is defined, where $p, q, r, s \in \mathbb{W}$ with $p+q+r+s \leq n$. With the use of m_{pqrs} , one can apply the Itô formula to (2.10) to generate stationary moment equations for the system [80], namely

$$\sum_{i=1}^{4} \left\langle \frac{\partial y_1^p y_2^q y_3^r y_4^s}{\partial y_i} \left(\hat{\mathbf{a}} \right)_i \right\rangle + \frac{1}{2} \sum_{i,j=1}^{4} \left\langle \left(\hat{\mathbf{\Sigma}} \hat{\mathbf{\Sigma}}^{\mathrm{T}} \right)_{ij} \frac{\partial^2 y_1^p y_2^q y_3^r y_4^s}{\partial y_i \partial y_j} \right\rangle = 0 \tag{2.12}$$

where $(\cdot)_i$ and $(\cdot)_{ij}$ represent the *i*-th and *ij*-th component of a vector and square matrix, respectively, and $\hat{\bf a}$ and $\hat{\bf \Sigma}$ are defined in (2.11). Because only small oscillation is of interest, the Gaussian closure technique (outlined in Appendix B) is applied to (2.12), resulting in 14 independent nonlinear algebraic equations. The resultant moment equations are very long and not given explicitly in this paper; the general form of the equations are

$$\hat{\mathbf{h}}(m_{1000}, m_{0100}, \cdots, m_{0020}, m_{0002}, \phi_0) = \mathbf{0}$$
(2.13)

where **h** represent 14 nonlinear functions of the four first order moments and ten second order moments and the unknown ϕ_0 . Note that (2.13) are underdetermined (14 equations and 15 variables). Assuming that the mean of the small pendulum angular displacement to be zero, i.e., $m_{0100} = \langle y_2 \rangle = \langle \phi \rangle = 0$, ϕ_0 can be determined. The resultant ϕ_0 will approximate the locations of maxima of the PDF.

The stationary moment equations given by (2.13), provide a means to determine the value of ϕ_0 as a function of system parameters. To accomplish this, an arc-length continuation technique is employed. Arc-length continuation provides a means for tracking the value of

 ϕ_0 while varying a parameter of interest. Denote by \mathbf{z} the vector consisting of ϕ_0 and the 13 moments excluding m_{0100} , and by $\mathbf{h} = \hat{\mathbf{h}}(m_{0100} = 0)$ the vector consisting of all the 14 nonlinear equations in (2.13) with $m_{0100} = 0$. Applying the arc-length continuation from [81] to (2.13), one arrives at the following:

$$\begin{cases} \mathbf{h}(\mathbf{z}; \lambda) = \mathbf{0} \\ \mathbf{J}_{\mathbf{z}}(\mathbf{z}; \lambda) \frac{d\mathbf{z}}{ds} + \frac{\partial \mathbf{h}(\mathbf{z}; \lambda)}{\partial \lambda} \frac{d\lambda}{ds} = \mathbf{0} \\ \frac{d\mathbf{z}}{ds} \cdot \frac{d\mathbf{z}}{ds} + (\frac{d\lambda}{ds})^2 = 1 \end{cases}$$
 (2.14)

where s represents the arc-length parameter, $\mathbf{J_z}$ is the Jacobian matrix of \mathbf{h} , while λ is a parameter of interest. The arc-length parameter is finally defined in the last of (2.14). The culmination of (2.14) define fifteen first order, nonlinear differential-algebraic equations that can be numerically integrated to obtain the maximum location $\phi_0(\lambda)$ as a function of λ , given with initial conditions that satisfy (2.13).

According to Sharif-Bakhtiar and Shaw [76], asymmetric oscillation of the pendulum is induced by a pitchfork bifurcation which belongs to limit point bifurcation. To determine the limit point, the first equation in (2.14) are differentiated with respect to the bifurcation parameter λ , resulting in

$$\frac{\partial \mathbf{h} \left(\mathbf{z}; \lambda \right)}{\partial \mathbf{z}} \frac{d\mathbf{z}}{d\lambda} = -\frac{\partial \mathbf{h} \left(\mathbf{z}; \lambda \right)}{\partial \lambda} \tag{2.15}$$

Limit point bifurcation occurs when any component of $d\mathbf{z}/d\lambda \to \infty$ or when the determinant $|\partial \mathbf{h}(\mathbf{z}; \lambda)/\partial \mathbf{z}| = 0$. The limit point and critical value of the bifurcation parameter can be determined by solving the first equation in (2.14) together, i.e.,

$$\begin{cases} \mathbf{h}(\mathbf{z};\lambda) = \mathbf{0} \\ \left| \frac{\partial \mathbf{h}(\mathbf{z};\lambda)}{\partial \mathbf{z}} \right| = 0 \end{cases}$$
 (2.16)

To track the limit point in the parameter space, (2.16) is augmented with the arc-length

continuation scheme, namely

$$\begin{cases} \mathbf{h}(\mathbf{z}; \lambda, \gamma) = \mathbf{0} \\ \left| \frac{\partial \mathbf{h}(\mathbf{z}; \lambda, \gamma)}{\partial \mathbf{z}} \right| = 0 \\ \mathbf{J}_{\mathbf{z}}(\mathbf{z}; \lambda, \gamma) \frac{d\mathbf{z}}{ds} + \frac{\partial \mathbf{h}(\mathbf{z}; \lambda, \gamma)}{\partial \lambda} \frac{d\lambda}{ds} + \frac{\partial \mathbf{h}(\mathbf{z}; \lambda, \gamma)}{\partial \gamma} \frac{d\gamma}{ds} = \mathbf{0} \\ \frac{d\mathbf{z}}{ds} \cdot \frac{d\mathbf{z}}{ds} + (\frac{d\lambda}{ds})^2 + (\frac{d\gamma}{ds})^2 = 1 \end{cases}$$

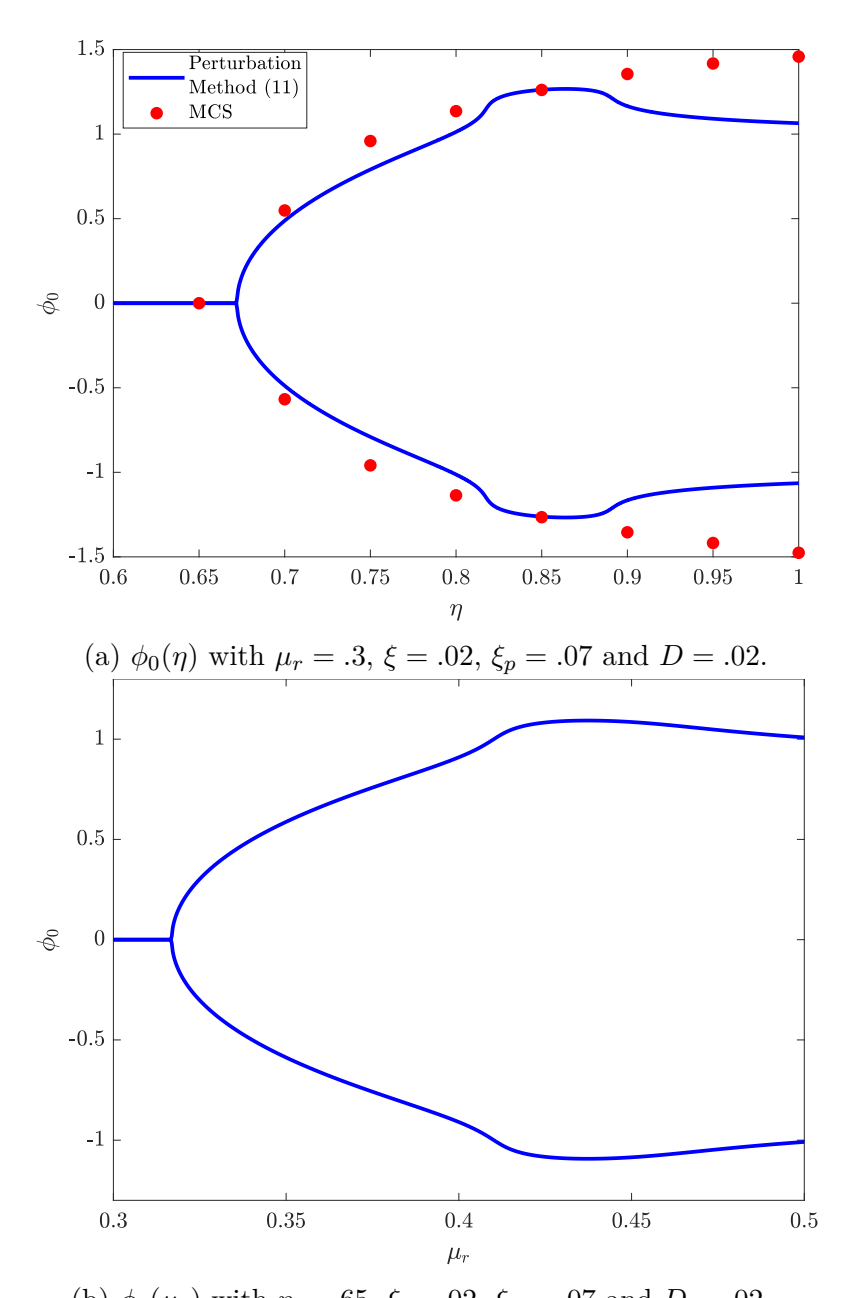
$$(2.17)$$

where γ is a second bifurcation parameter of interest. Since the limit point occurs with $\phi_0 = 0$, $\phi_0 = 0$ is substituted in (2.17), which annihilates three first order moments $m_{1000} = m_{0010} = m_{0001} = 0$ and two second order moments $m_{1010} = m_{0101} = 0$. Solving (2.17) yields the limit point curve $\phi_0(\lambda, \gamma) = 0$ in the $\lambda - \gamma$ plane, which describes the values of λ and γ for which the limit point bifurcation occurs.

2.2.2 Numerical Validation

Using (2.14), $\phi_0(\mu_r)$ and $\phi_0(\eta)$ were determined as a function of μ_r and η , respectively, for specific parameter values. The results are shown in Fig. 2.2. There are several things worth noting in Fig. 2.2. First, as seen in Fig. 2.2(a), $\phi_0(\eta)$ bifurcates into two solution branches around $\eta = 0.65$. For η values smaller than this critical value, only one solution branch $\phi_0 = 0$ exists, which indicates that the pendulum symmetrically oscillates with respect to $\phi_0 = 0$. This is expected because when η or μ_r are small, the nonlinear terms \mathbf{g} in (4.10) are weak; thus, the system behaves similar to a linear system. As η increases and exceeds the critical value, the nonlinearity becomes sufficiently strong such that asymmetric oscillation occurs. In the context of random vibration, coexistence of two local maxima means a bimodal PDF; that is, the pendulum can symmetrically oscillate with respect to either maximum location and randomly "jump" between each other. The same bifurcation is observed in $\phi_0(\mu_r)$; see Fig. 2.2(b).

To validate the prediction in Fig. 2.2, a Monte Carlo simulation (MCS) was used to numerically compute the marginal PDF of ϕ for various η values. Numerically integration of (2.8) was specifically done by ItoProcess of Mathematica 12.1, which is a stochastic differential equation solver. The time step was chosen to be 10^{-3} units to ensure accuracy.



(b) $\phi_0(\mu_r)$ with $\eta = .65$, $\xi = .02$, $\xi_p = .07$ and D = .02.

Figure 2.2 Bifurcation diagram of ϕ_0 against (a) η and (b) μ_r .

An integration time of 500 units was found to be sufficiently long so as to ensure stationarity as it allowed for asymmetric pendulum oscillation to occur. Furthermore, a sufficiently large number of realizations (around 4×10^5) were recorded to ensure accuracy. SmoothK-ernelDistribution of Mathematica 12.1 was then used to compute the marginal PDF of the realizations. The result for various values of η and specified parameter values corresponding to Fig. 2.2(a) is plotted in Fig. 2.3. There are two things worth noting in Fig. 2.3. First, it is evident that around $\eta = .65$ a bifurcation occurs as the distributions become bimodal afterwards, which matches the prediction in Fig. 2.2(a). Second, it is apparent that an increase in the pendulum length parameter η leads to an increase in the distance between the maximum locations. The maximum locations predicted by Monte Carlo simulation are plotted as dots for comparison in Fig. 2.2(a). In comparison with the Monte Carlo simulation, the prediction by (2.14) matches well until $\eta = 0.8$. Afterwards the nonlinearity becomes too strong such that the perturbation method is no longer accurate. The implications of this bifurcation are further addressed in the sections that follow.

In order to provide additional insight and verification for the determined marginal PDFs, realizations in the time domain for the pendulum position and velocity are also shown in Fig. 2.4. The realizations were produced with η values before, near and after bifurcation. The duration of time was chosen to be from 500 to 1000 units as it is assumed that the system is stationary after 500 units of time. The first remark is that the mono-modal oscillation around $\phi = 0$ is apparent before bifurcation. Near bifurcation we also start to see a drift in the oscillation away from $\phi = 0$ accompanied by larger amplitude spikes in the angular displacement and velocity. Lastly, after bifurcation we see the pendulum tends to oscillate about one equilibrium angle for a more significant amount of time before making a jump to another equilibrium angle.

2.2.3 Stochastic Bifurcation and Energy Transfer

In this section, the mean square velocities of the primary structure and pendulum oscillation are investigated. Specific attention is paid to investigating how the bifurcation influences

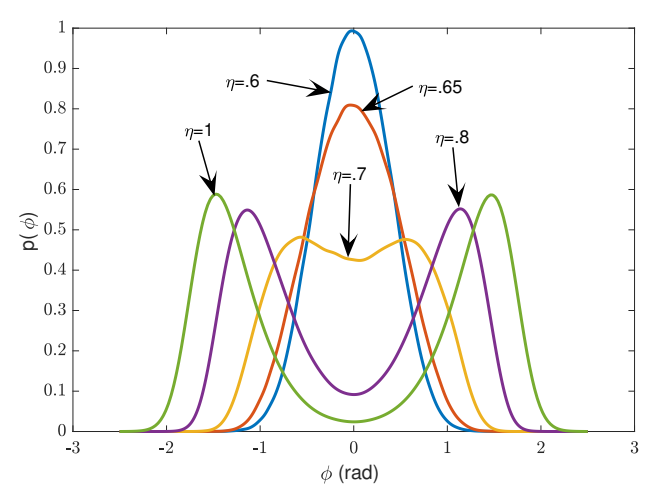


Figure 2.3 Monte Carlo simulation of the marginal PDF for ϕ evaluated with values of η around bifurcation and with $\mu_r = .3$, $\xi = .02$, $\xi_p = .07$, and D = .02.

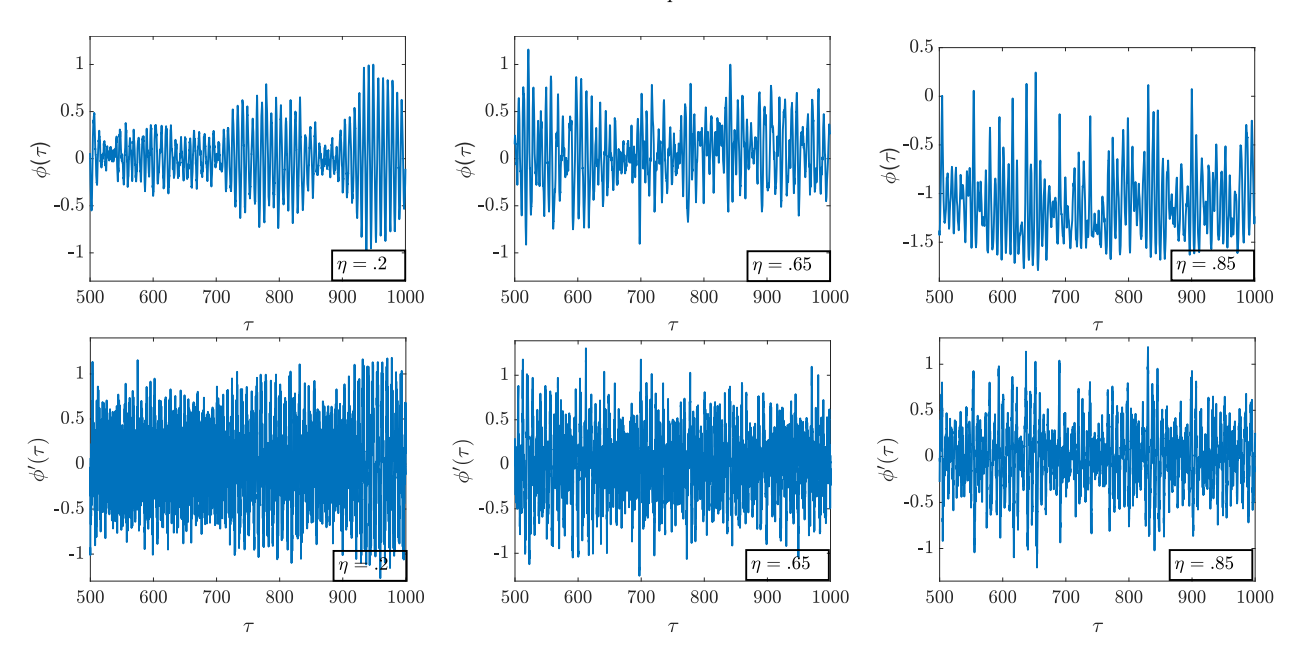


Figure 2.4 Realizations in the time domain for pendulum angular displacement and velocity before bifurcation, near bifurcation, and after bifurcation. $\mu_r = .3$, $\xi = .02$, $\xi_p = .07$, and D = .02.

the mean square velocity. Eqn. (2.13) allows for the determination of the bifurcation point of the moment equations and is built upon the assumption of a Gaussian distribution in the neighborhood of ϕ_0 . A higher order of nonlinearity is required to accurately predict all mean square values. To this end, it is assumed that $\mathbf{y} = \left(\epsilon \bar{\theta}, \epsilon \bar{\phi}, \epsilon \dot{\bar{\theta}}, \epsilon \dot{\bar{\phi}}\right)^T = \epsilon \bar{\mathbf{y}}$, where ϵ is a small scaling parameter. In this work, $\epsilon = \sqrt{\frac{D}{2(\xi + \xi_p)}}$, which corresponds to the root-mean-square displacement of a linear system that is obtained by removing the IPVA from the system and

assuming the viscous damping ratio is $\xi + \xi_p$. Substituting $\mathbf{y} = \epsilon \bar{\mathbf{y}}$ into (2.8) and expanding in a Taylor series up to order r = 7 with respect to ϵ results in

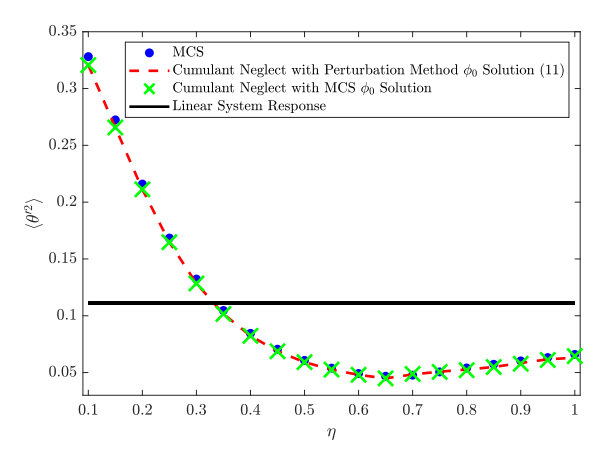
$$\bar{\mathbf{a}}(\bar{\mathbf{y}}, \phi_0) = \mathbf{a}(\epsilon \bar{\mathbf{y}}, \phi_0)|_{\epsilon=0} + \sum_{i=1}^r \epsilon^i \times \left(\frac{\partial^i \mathbf{a}(\epsilon \bar{\mathbf{y}}, \phi_0)}{i! \partial \epsilon^i} \right) \Big|_{\epsilon=0}$$

$$\bar{\mathbf{\Sigma}}(\bar{\mathbf{y}}, \phi_0, \tau) = \mathbf{\Sigma}(\epsilon \bar{\mathbf{y}}, \phi_0, \tau)|_{\epsilon=0} + \sum_{i=1}^r \epsilon^i \times \left(\frac{\partial^i \mathbf{\Sigma}(\epsilon \bar{\mathbf{y}}, \phi_0, \tau)}{i! \partial \epsilon^i} \right) \Big|_{\epsilon=0}$$
(2.18)

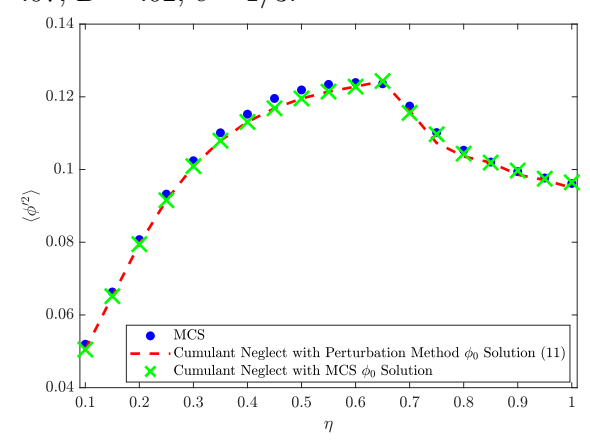
where a and Σ are defined in (4.14). Stationary moment equations with moments $m_{pqrs} = \langle y_1^p y_2^q y_3^r y_4^s \rangle$ up to order n=4 are then generated from (2.18) by the cumulant-neglect technique [82, 83]. All cumulants of higher order than n=4 are neglected by assuming that they have negligible contribution. To this end, cumulants of orders higher than n=4 are set to zero to obtain expressions of higher order moments in terms of lower orders, resulting in 69 nonlinear algebraic equations governing all moments up to fourth order, while additionally having a dependence on ϕ_0 ; see the appendix for more information. The system is thus underdetermined unless ϕ_0 is specified. Using the solution for ϕ_0 from (2.14), ϕ_0 can be substituted into the resultant 69 equations to allow for a solution for the 69 unknown moment variables.

Choosing the parameters associated with Fig. 2.2(a), corresponding to bifurcation occurring at $\eta = .65$, the $\phi_0(\eta)$ values predicted thereof was substituted into the 69 moment equations to calculate the mean square velocities $\dot{\theta}$ and $\dot{\phi}$ of the ball screw and pendulum, respectively. The results are plotted in Fig. 2.5. Because $\dot{\theta}$ is proportional to the velocity of the primary structure via $\dot{x} = R\dot{\theta}$, it is a measure of the kinetic energy of the primary structure. As such, we can examine how the energy transfers to the pendulum as a function of η . To validate the results, the mean square velocities computed by the MCS are also plotted in Fig. 2.5, which show indiscernible discrepancy in comparison with the results obtained by the moment equations.

There are several things worth noting in Fig. 2.5. First, Fig. 2.5(a) shows a general decrease in $\dot{\theta}$ as a result of increasing η . It specifically reaches a minimum value at the critical point where the bifurcation occurs ($\eta \approx 0.65$). Meanwhile, Fig. 2.5(b) shows that



(a) Ball screw mean square velocity as a function of η compared to linear system response. $\mu_r = .3, \ \xi = .02, \ \xi_p = .07, \ D = .02, \ \epsilon = 1/3.$



(b) Pendulum mean square velocity as a function of η . $\mu_r = .3$, $\xi = .02$, $\xi_p = .07$, D = .02, $\epsilon = 1/3$.

Figure 2.5 Comparison of mean squares of nonlinear system obtained by MCS and cumulantneglect and mean square of linear system while varying η . (a) Ball screw mean square velocity. (b) Pendulum mean square velocity.

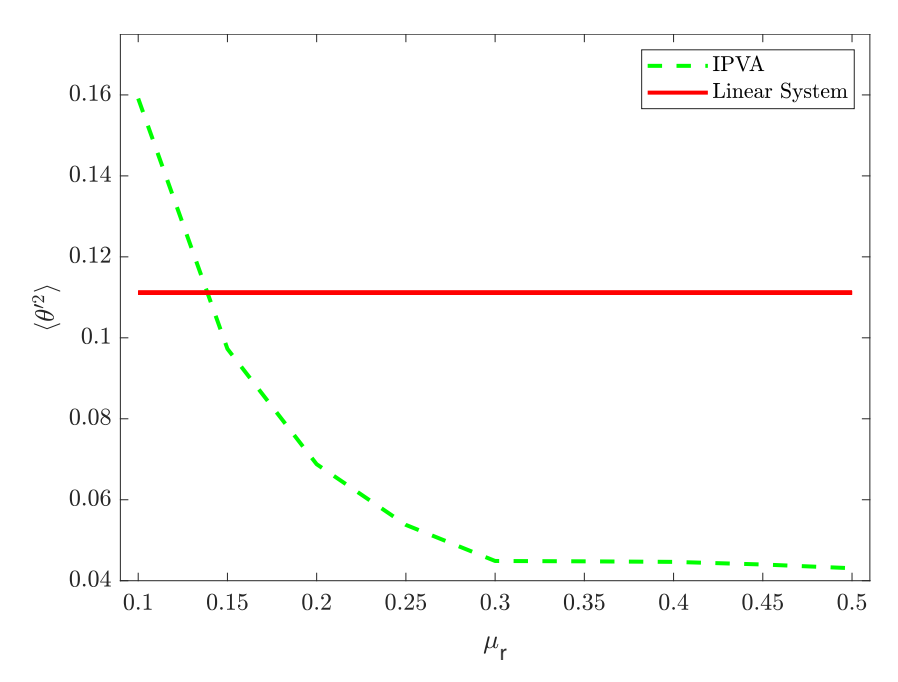
 $\dot{\phi}$ reaches a maximum at the bifurcation point. The observed trends clearly demonstrate that the kinetic energy of the primary structure transfers to the pendulum, which reaches a maximum at the bifurcation point. To demonstrate the efficacy of response suppression via this energy transfer, the mean square velocity $\langle \dot{\theta}_l^2 \rangle$ of the ball screw without the IPVA is plotted with solid line in Fig. 2.5(a), which is derived in the Appendix C. For a fair comparison, the viscous damping ratio of the linear system $\hat{\xi} = \xi + \xi_p$ is set, which equals the sum of the two damping ratios of the nonlinear system. As shown in Fig. 2.5(a), the response of the primary structure with IPVA is significantly lower than that without IPVA,

especially at the bifurcation point. Second, to investigate the influence of ϕ_0 on the mean squares, the mean squares were also computed with the proposed cumulant-neglect scheme using the $\phi_0(\eta)$ obtained from the MCS (dots in Fig. 2.2(a)), plotted with crosses in Fig. 2.5. Although the MCS and perturbation method (2.14) show discrepancy when predicting $\phi_0(\eta)$ at large η values (see Fig. 2.2(a)), it is interesting to note that the mean squares obtained by these two methods show little discrepancy in Fig. 2.5. This implies that the discrepancy is not large enough to cause significant errors in the mean square values, while it should be noted that higher order moments might lose accuracy with the perturbation ϕ_0 solution. This is, however, beyond the scope of this work. Cumulant-neglect used with the perturbation ϕ_0 solution is therefore sufficient for the remaining analysis in this chapter.

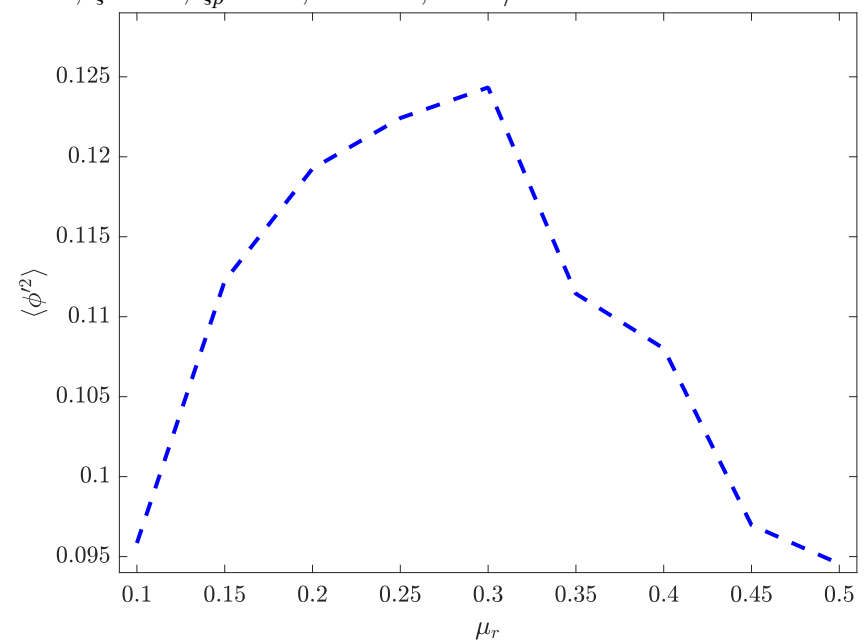
By choosing $\eta = .65$, which corresponds to the maximum energy transfer in Fig. 2.5, μ_r is varied to understand its influence on bifurcation. The mean square ball screw and pendulum velocities as a function of μ_r were calculated with the cumulant-neglect procedure with a $\phi_0(\mu_r)$ substitution obtained from the perturbation method, which are shown in Fig. 2.6a and Fig. 2.6b, respectively. It is clear that the optimal energy transfer occurs at the bifurcation point around $\mu_r = 0.3$. Larger values of μ_r lead to lower pendulum velocities, while smaller values will also increase the velocity of the ball screw and hence the response of the primary structure.

2.3 Parametric Study

Sec. 2.2 shows that the limit point bifurcation promotes the energy transfer and response suppression for a specific noise intensity level. It is worthwhile to investigate the performance of response suppression with different noise intensity levels. By setting $\lambda = \xi_p$ and $\gamma = D$ to be the two bifurcation parameters, (2.17) are used to generate the bifurcation curve in the $\lambda - \gamma$ plane, which determines the values of λ and γ for which the limit point bifurcation occurs. The damping ξ_p is chosen as a bifurcation parameter because there exist many engineering applications that allow for variable damping. For example, Kecik and Borowiec [84] suggested installing an electromagnetic motor at the pivot point of the pendulum, which



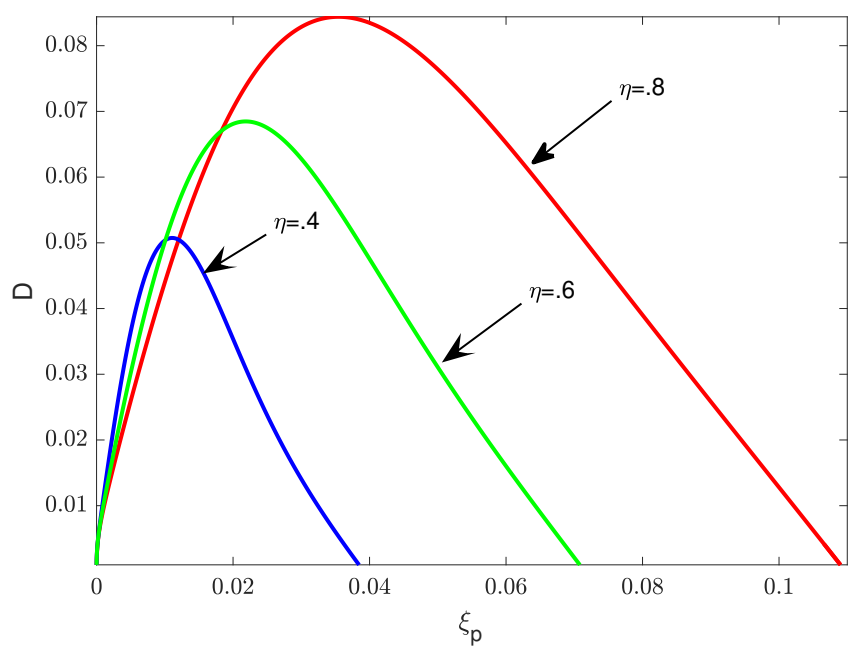
(a) Ball screw mean square velocity as a function of μ_r compared to linear system response. $\eta=.65,\,\xi=.02,\,\xi_p=.07,\,D=.02,\,\epsilon=1/3.$

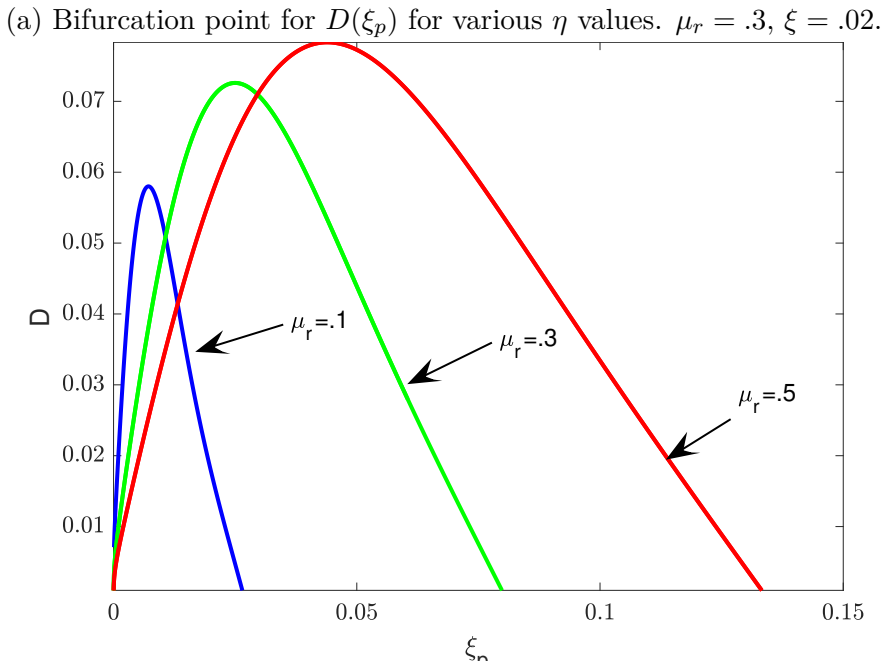


(b) Pendulum mean square velocity as a function of μ_r . $\eta = .65$, $\xi = .02$, $\xi_p = .07$, D = .02, $\epsilon = 1/3$.

Figure 2.6 Comparison of mean squares of nonlinear system obtained by cumulant-neglect and mean square of linear system while varying μ_r . (a) Ball screw mean square velocity. (b) Pendulum mean square velocity.

is shunted with resistive loads. As such, the pendulum damping can be passively adjusted by varying the resistance. Using the pulse width modulated (PWM) set-up chopper, Kim and Okada [85] showed that semi-active damping control of electromagnetic transducers can be achieved, suggesting the pendulum damping can be controlled in a semi-active manner.





(b) Bifurcation point for $D(\xi_p)$ for various μ_r values. $\eta=.65,\,\xi=.02.$

Figure 2.7 Bifurcation diagram of limit points in the $D - \xi_p$ plane with varying (a) η and (b) μ_r .

Shown in Fig. 2.7a are then the bifurcation curves for a few values of the pendulum length parameter (η) . The bifurcation curves for a few values of μ_r are additionally shown

in Fig. 2.7b. There are several things worth noting regarding Figs. 2.7a and 2.7b. First, the bifurcation curves show the values of noise intensity, ξ_p , μ_r and η that lead to a pitchfork bifurcation. It should be noted that for a chosen μ_r , η and noise intensity, one identifies two possible choices of pendulum damping on each curve except on the vertex. For example, as shown in Fig. 2.7a, for $\mu_r = 0.3$, $\eta = 0.6$, and D = 0.05, $\xi_p \approx 0.01$ and $\xi_p \approx 0.04$ each lead to a pitchfork bifurcation. The smaller values of pendulum damping on each curve lead to intermittent pendulum motion that is characterized by oscillations around one equilibrium angle marked by sporadic pendulum rotations. As analysis involving such intermittent rotation is not within the scope of this paper, we restrict our attention to larger values of pendulum damping, i.e., the right portion of each bifurcation curve in Fig. 2.8. Second, the bifurcation curves also show that one can adjust the pendulum damping so as to maintain a bifurcation condition for a wide range of noise intensity, η and μ_r values.

Shown in Figs. 2.8(a) and 2.8(b) are the mean square velocities corresponding to points along the right portion of the bifurcation curves in Fig. 2.7a. It generally appears as though an increase in η reduces the pendulum velocity and only slightly influences the angular velocity of the screw. Furthermore, an increase in noise intensity D along the bifurcation curves has the effect of monotonically increasing the total energy transfer. To further quantify vibration suppression, the mean square velocity associated with the linear system corresponding to the best response suppression is also shown in Fig. 2.8(a). The value of damping corresponding to that obtained by following the $\eta = 0.8$ bifurcation curve of Fig. 2.7a was thus chosen for the linear system. It is interesting to note that the IPVA system always outperforms the linear system for the particular set of parameters considered herein.

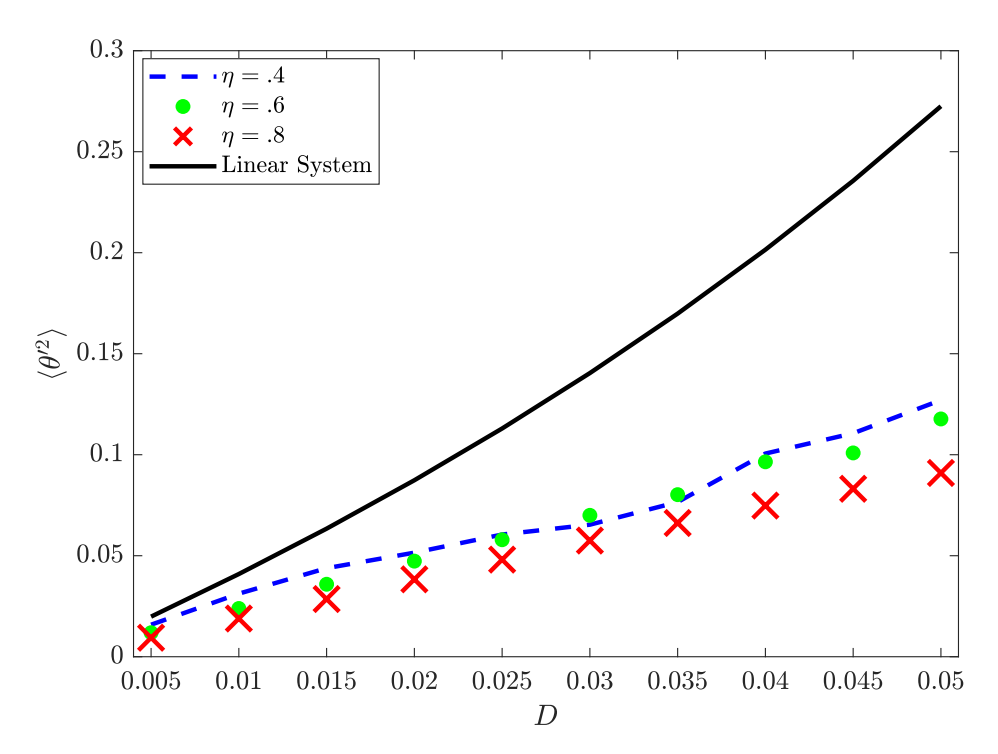
After choosing parameters corresponding to the bifurcation points on the right portion of the bifurcation curves with a noise intensity of D = 0.02, we then show the variation in the locations of local maximum ϕ_0 as a function of η in Fig. 2.9. The combined results shown in Fig. 2.8 and Fig. 2.9 show that a bifurcation point corresponding to smaller η is correlated with higher pendulum mean square velocity. Furthermore, the bifurcation

diagrams of Fig. 2.9 show that a bifurcation point corresponding to smaller η leads to a larger increase per η in the distance between the locations of local maxima.

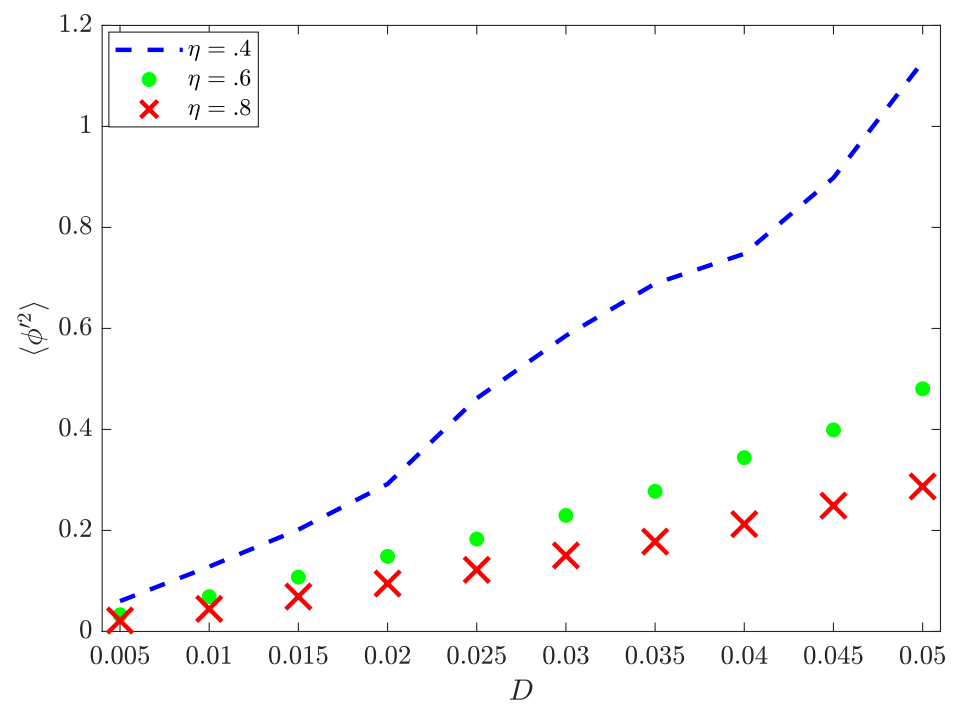
Moving our attention to the limit point bifurcation diagrams shown in Fig. 2.7b, we can then repeat the analysis with variation in μ_r . The results for the mean square ball screw and pendulum velocities, at various bifurcation points, are shown in Figs. 2.10a and 2.10b, respectively. It is interesting to note that an increase in μ_r will lead to lower velocity of the ball screw and primary mass, while the velocity of the pendulum will first increase and then decrease. Hence, a larger pendulum-structure mass ratio could be warranted if vibration suppression is of sole interest.

2.4 Discussion on Findings

In this chapter, the vibration suppression, energy transfer and bifurcation characteristics of a linear oscillator (primary structure) incorporating an inerter-based pendulum vibration absorber (IPVA) were investigated as a function of normalized pendulum length η and mass ratio μ_r . A perturbation method was introduced in conjunction with arc-length continuation to detect and track the pendulum equilibrium angles corresponding to local maxima of the marginal probability density function (PDF) in the parameter space. The obtained pendulum equilibrium angles were implemented in a cumulant-neglect based procedure with a 7^{th} order Taylor expansion about the equilibrium angles to obtain the mean squares of the system. It was shown that the marginal PDF underwent a P-bifurcation (mono-modality to bi-modality) at critical values of η and μ_r . In comparison with mean squares of the linear structure without the IPVA, it was shown that the IPVA led to effective vibration mitigation of the structure via transferring the kinetic energy of the structure to the pendulum. Furthermore, it was shown that the energy transfer was maximum in the neighborhood of bifurcation. The results were validated by an MCS that was used to numerically approximate the marginal PDF for the pendulum angle as well as the mean square values.



(a) Ball screw mean square velocity vs. noise intensity via cumulant-neglect for various η values. $\mu_r = .3, \, \xi = .02.$



(b) Pendulum mean square velocity vs. noise intensity via cumulant-neglect for various η values. $\mu_r = .3, \, \xi = .02.$

Figure 2.8 Mean squares of nonlinear system with parameters corresponding points along the bifurcation curves in Fig. 2.7(a): (a) ball screw mean square velocity and (b) pendulum mean square velocity.

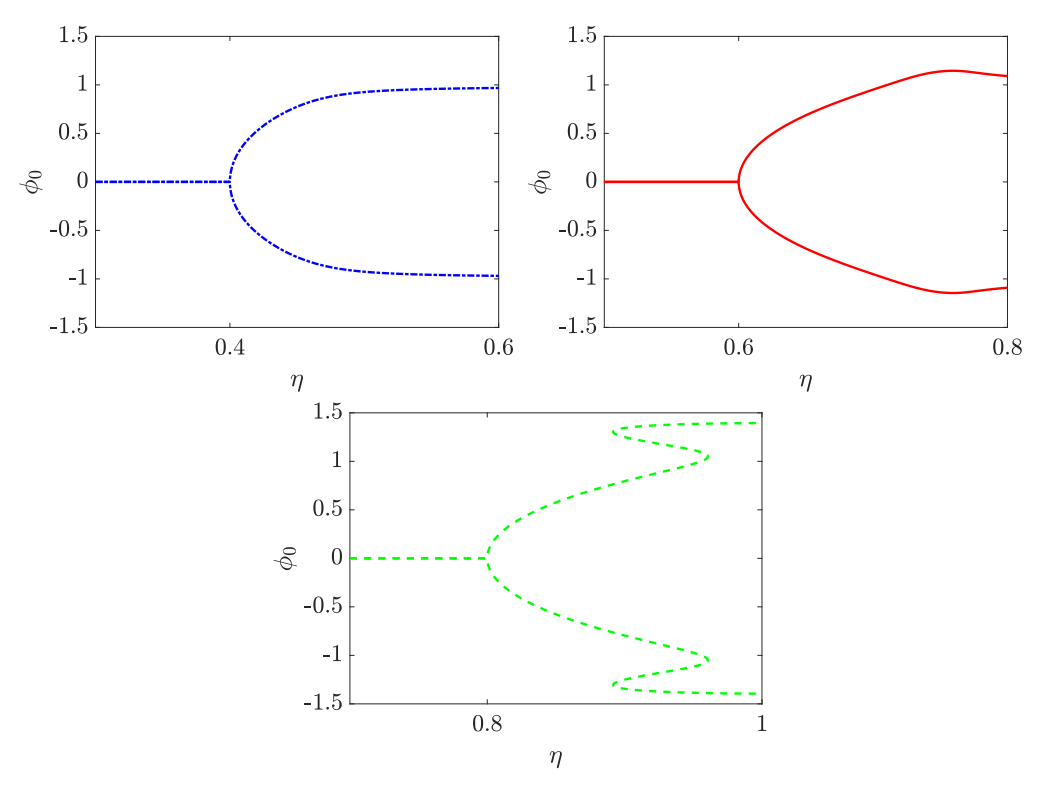
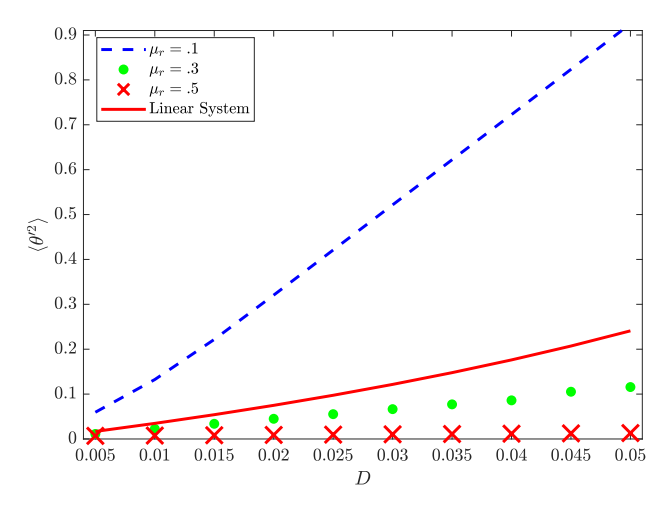
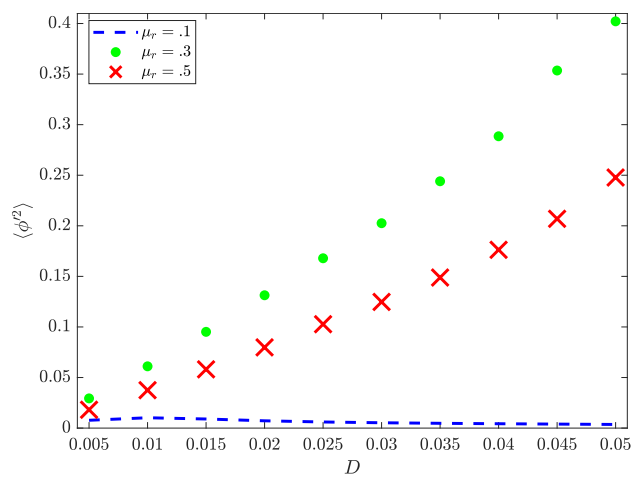


Figure 2.9 Pendulum equilibrium angle of oscillation $\phi_0(\eta)$ for various bifurcation conditions with $\mu_r = .3, \ \xi = .02.$



(a) Ball screw mean square velocity vs. noise intensity via cumulant neglect for various μ_r values. $\eta = .65, \xi = .02.$



(b) Pendulum mean square velocity vs. noise intensity via cumulant neglect for various μ_r values. $\eta=.65,\,\xi=.02.$

Figure 2.10 Mean squares of nonlinear system with parameters corresponding points along the bifurcation curves in Fig. 2.7(b): (a) ball screw mean square velocity and (b) pendulum mean square velocity.

CHAPTER 3

ENERGY HARVESTING, RIDE COMFORT AND ROAD HANDLING IN AUTOMOBILE SUSPENSION SYSTEMS

3.1 Introduction to the Energy Harvesting Shock Absorber

In this chapter, the nonlinear device introduced in the previous chapter is implemented in a quarter-car model suspension system in an EHSA. The questions to be answered are whether the bifurcation phenomena demonstrated in the last chapter will still show up and whether we can make a strong correlation between optimal energy harvesting, vibration suppression and P-bifurcation. To this end, performance metrics such as sprung mass acceleration, power harvested and road handling are evaluated near bifurcation.

The rest of this chapter is organized as follows. In Sec. 3.2, the system design with equations of motion (EOM) are shown followed by the development of an analytical bifurcation theory coupled with a Wiener path integration (WPI) formulation. An efficient perturbation-based algorithm is then defined which covers a large parameter space. In Sec. 3.3, a parameter study is conducted to allow the determination of power harvested, ride comfort, and road handling metrics as a function of a pendulum length parameter which is responsible for the nonlinearity. Electrical efficiency and energy flow are also considered. Finally, the relevant findings are summarized in Sec. 3.5.

3.2 Stochastic Bifurcation Detection Algorithm

In the previous chapter it was shown that P-bifurcation, involving the change in the maxima of the stationary PDF, was apparent and led to substantial transfer of the kinetic energy of the primary structure to the pendulum. As the same device is considered in this chapter concerning the EHSA, this phenomenon is further explored in association with the quarter-car model. The theoretical development of the method used to predict this P-bifurcation is presented in this section, where an efficient implementation of the Wiener path integration formulation originally outlined in [10] is modified to fit the current problem and augmented with a calculus of variations approach for the prediction of change in the

curvature of the PDF.

3.2.1 Equations of motion of the EHSA

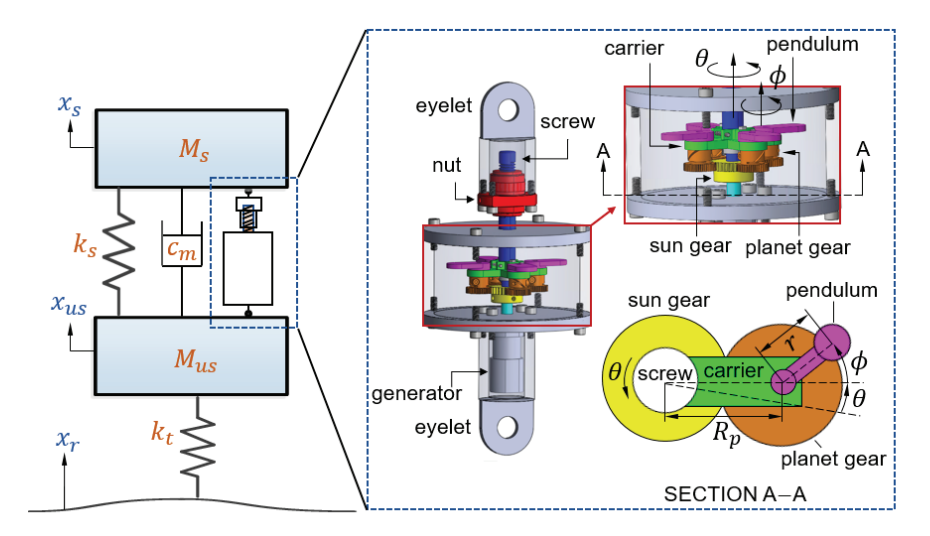


Figure 3.1 Schematics of an IPVA-integrated quarter-car model.

The IPVA-integrated quarter-car system is shown in Fig. 3.1. As shown, x_s denotes the position of the sprung mass (vehicle body) M_s , x_{us} the position of the unsprung mass (wheel) M_{us} , and x_r the road elevation. The top and bottom eyelets in Fig. 3.1 then attach to M_s and M_{us} , respectively. This connection then converts the translational motion between the eyelets to the angular motion of the ball screw inside the case. The holonomic constraint $x_s - x_{us} = R\theta$ then relates the suspension deflection $x_s - x_{us}$ to the angular displacement of the ball screw θ with $R = L/2\pi$, where L is the lead value for the ball screw. Note that attached to the ball screw is then a carrier that carries four pendulums. Each of the planet gears is mounted to the shaft of the corresponding pendulum so that all pendulums have the same angular position ϕ relative to the carrier. Furthermore, they each revolve around the sun gear such that the angular displacement of the latter is given by $\theta - \phi$. As the sun gear is mounted to the generator shaft, the angular motion $\theta - \phi$ serves as the input of the generator.

To simplify a parameter variation study, the following dimensionless parameters and

normalized time were chosen in the present work.

$$\mu_{r} = \frac{mR_{p}^{2}}{M_{s}R^{2}}, \ \omega_{o} = \sqrt{\frac{k_{s}}{M_{s}}}, \ \xi = \frac{c_{m}}{2M_{s}\omega_{o}}, \ \xi_{e} = \frac{c_{e}}{2M_{s}R^{2}\omega_{o}},$$

$$u = \frac{M_{us}}{M_{s}}, \ \mu_{g} = \frac{J_{g}n_{g}^{2}}{M_{s}R^{2}}, \ \omega_{t} = \sqrt{\frac{k_{t}}{M_{us}}}, \psi_{us} = \frac{x_{us}}{R}, \ \Psi_{r} = \frac{x_{r}}{R},$$

$$\tau = \omega_{0}t, \ \frac{d}{d\tau} = ()', \ v = \frac{\omega_{t}}{\omega_{o}}, \ \eta = \frac{r}{R_{p}}$$
(3.1)

Note that R_p and r are the distance between the pendulum pivot point and center of rotation of the carrier, and the length of the pendulum, respectively. The parameters J_g , n_g , k_s , and k_t represent the principal moment of inertia of the generator rotor, the generator gearbox ratio, suspension stiffness, and tire stiffness, respectively. ω_0 is then a frequency that is dependent on the sprung mass and suspension stiffness which is chosen as the characteristic frequency to define dimensionless time τ . Finally, c_e denotes the electrical damping constant due to the generator [86] and c_m is the mechanical damping constant which quantifies mechanical losses associated with the ball screw motion $R\dot{\theta}$. The equations of motion for the system were then derived in terms of the dimensionless parameters and dimensionless time. With $\mathbf{z} = [\theta, \phi, \psi_{us}]^T$, the dimensionless EOM are as follows:

$$\mathbf{Mz''} + \mathbf{Cz'} + \mathbf{Kz} = \mathbf{F}(\mathbf{z}, \mathbf{z'}, \Psi_r)$$
(3.2)

where

$$\mathbf{M} = \begin{bmatrix} M_{11} & M_{12} & 1 \\ M_{12} & M_{22} & 0 \\ 1 & 0 & u+1 \end{bmatrix}, \mathbf{C} = \begin{bmatrix} 2(\xi + \xi_e) & -2\xi_e & 0 \\ -2\xi_e & 2\xi_e & 0 \\ 0 & 0 & 0 \end{bmatrix}, \mathbf{K} = \begin{bmatrix} 1 & 0 & 0 \\ 0 & 0 & 0 \\ 0 & 0 & uv^2 \end{bmatrix},$$

$$\mathbf{F}(\mathbf{z}, \mathbf{z}', \Psi_r) = \begin{pmatrix} \mu_r \eta (2\phi' \theta' + (\phi')^2) \sin(\phi) \\ -\mu_r \eta (\theta')^2 \sin(\phi) \\ uv^2 \Psi_r \end{pmatrix}$$
(3.3)

and

$$M_{11} = \mu_g + \mu_r \left(\eta^2 + 2\eta \cos(\phi) + 1\right) + 1, \quad M_{12} = \eta \mu_r (\eta + \cos(\phi)) - \mu_g, \quad M_{22} = \eta^2 \mu_r + \mu_g$$
(3.4)

 Ψ_r corresponds to the dimensionless road profile acting as the excitation. The EOM for the road excitation is given here

$$\Psi_r' + v_c \Psi_r = n(\tau) \tag{3.5}$$

where $n(\tau) = \frac{W(\tau)}{\omega_o R}$ is a dimensionless random disturbance where $W(\tau)$ is a white noise process. $n(\tau)$ has expectation $E[n(\tau)] = 0$ and auto-correlation function $E[n(\tau)n(\epsilon + \tau)] = d\delta(\epsilon)$ and $d = \frac{2\pi G_r V}{\omega_0 R^2}$ is the dimensionless noise intensity. Furthermore, G_r quantifies the road roughness and V is the driving speed as described in [86]. $E[\cdot]$ represents the expected value of quantity "·". Finally, ω_c is the cutoff frequency that allows for the power spectral density (PSD) of the road excitation to remain bounded when the frequency ω equals zero. Then v_c is a dimensionless cutoff frequency defined by the ratio of the physical cutoff frequency ω_c to ω_0 . The dimensionless power spectral density (PSD) is given by

$$S_{\Psi_r} = \frac{d}{(\omega/\omega_0)^2 + v_c^2} \tag{3.6}$$

3.2.2 The Wiener Path Integration Implementation

Following similar notation and framework as in [18, 19], the transition PDF $p(\mathbf{y}_f, \tau_f | \mathbf{y}_i, \tau_i)$ gives the probability density of all states $\mathbf{y} = \left[\mathbf{z}^T, \Psi_r, \left(\mathbf{z}^T\right)'\right]^T$ starting at τ_i as \mathbf{y}_i and ending at τ_f as \mathbf{y}_f . It is written as

$$p(\mathbf{y}_f, \tau_f | \mathbf{y}_i, \tau_i) = \int_{C\{\mathbf{y}_f, \tau_f; \mathbf{y}_i, \tau_i\}} W[\mathbf{y}(\tau)][d\mathbf{y}(\tau)]$$
(3.7)

where $W[\mathbf{y}(\tau)]$ is the probability density functional on the space of all possible paths $C\{\mathbf{y}_f, \tau_f; \mathbf{y}_i, \tau_i\}$ starting at (\mathbf{y}_i, τ_i) and terminating at (\mathbf{y}_f, τ_f) with $\mathbf{y}_i = \mathbf{y}(\tau_i)$ and $\mathbf{y}_f = \mathbf{y}(\tau_f)$.

For a white noise process $n(\tau)$, the probability density functional is well known and can be expressed as

$$W[n(\tau)] = C \exp\left[-\int_{\tau}^{\tau_f} \frac{n^2(\tau)}{2d} d\tau\right]$$
(3.8)

where C is a normalization constant that induces a total probability of one [18]. Substituting the expression for the white noise as a function of Ψ_r and Ψ'_r given in (3.5), one obtains

$$W[\mathbf{y}(\tau)] = C \exp \left[-\int_{\tau_i}^{\tau_f} \frac{(\Psi'_r + v_c \Psi_r)^2}{2d} d\tau \right],$$

$$= C \exp \left[-\int_{\tau_i}^{\tau_f} \mathcal{L}(\Psi_r) d\tau \right]$$
(3.9)

where \mathcal{L} is then the Lagrangian of the system and is in general a functional of the states and state derivatives of the system. It is evident from (3.9) that $W[\mathbf{y}(\tau)]$ can be maximized by finding a path \mathbf{y}^* that minimizes \mathcal{L} , which is also known as the most probable path. Substituting the maximized $W[\mathbf{y}^*(\tau)]$ into (3.7) and isolating the most probable path will yield the first-order approximation of the PDF [87]

$$p(\mathbf{y}_f, \tau_f | \mathbf{y}_i, \tau_i) \approx C \exp \left[-\int_{\tau_i}^{\tau_f} \mathcal{L}(\Psi_r^*) d\tau \right]$$

As the definition of \mathcal{L} in (3.9) does not explicitly depend on \mathbf{z} and \mathbf{z}' in (4.9), it is insufficient to use \mathcal{L} to find \mathbf{y}^* . This can be remedied by converting the minimization problem into a constrained minimization problem. To that end, an auxiliary Lagrangian $\mathcal{L}^*(\mathbf{y}, \boldsymbol{\lambda}) = \mathcal{L}(\Psi_r) + \boldsymbol{\lambda}^T(\tau) \boldsymbol{\Phi}(\Psi_r, \mathbf{z})$ is introduced, where the dynamic constraints are

$$\Phi (\Psi_r, \mathbf{z}) = M\mathbf{z}'' + C\mathbf{z}' + K\mathbf{z} - F(\mathbf{z}, \mathbf{z}', \Psi_r) = 0$$
(3.10)

and $\lambda(\tau)$ denotes the time dependent Lagrange multiplier vector [10]. From the calculus of variations, \mathbf{y}^* that minimizes \mathcal{L}^* can be found by solving the following constrained variational equation

$$\delta \int_{\tau_i}^{\tau_f} \mathcal{L}^* (\mathbf{y}, \boldsymbol{\lambda}) d\tau = 0$$
 (3.11)

which naturally leads to the Euler-Lagrange equations given here.

$$\frac{\partial \mathcal{L}^*}{\partial \mathbf{x}} - \frac{d}{d\tau} \frac{\partial \mathcal{L}^*}{\partial \mathbf{x}'} + \frac{d^2}{d\tau^2} \frac{\partial \mathcal{L}^*}{\partial \mathbf{x}''} = \mathbf{0},
\frac{\partial \mathcal{L}^*}{\partial \boldsymbol{\lambda}} = \mathbf{0}$$
(3.12)

with generalized coordinates $\mathbf{x} = \begin{bmatrix} \mathbf{z}^T, \Psi_r \end{bmatrix}^T$. The associated boundary conditions are

$$\mathbf{x}(0) = \mathbf{x}_{0}, \quad \mathbf{x}(\tau_{f}) = \mathbf{x}_{f},$$

$$\mathbf{x}'(0) = \mathbf{x}'_{0}, \quad \mathbf{x}'(\tau_{f}) = \mathbf{x}'_{f},$$

$$\boldsymbol{\lambda}(0) = \boldsymbol{\lambda}_{0}, \quad \boldsymbol{\lambda}(\tau_{f}) = \boldsymbol{\lambda}_{f},$$

$$\boldsymbol{\lambda}'(0) = \boldsymbol{\lambda}'_{0}, \quad \boldsymbol{\lambda}'(\tau_{f}) = \boldsymbol{\lambda}'_{f}$$

$$(3.13)$$

Note that there are a total of seven second-order differential equations in (3.12) and therefore only fourteen of the boundary conditions in (3.13) can be fully specified. The rest of the boundary values are determined via the solution process automatically. Finally, the solution will yield the most probable path of all seven states \mathbf{y} from (3.2) through (3.5) in addition to new pseudo states $\left[\Psi'_r, \boldsymbol{\lambda}^T, \left(\boldsymbol{\lambda}^T\right)'\right]^T$ which are solely associated with (3.12). Finally, the approximate transition PDF for \mathbf{y} is given by

$$p(\mathbf{y_f}, \tau_f | \mathbf{y_i}, \tau_i) \approx C \exp \left[-\int_{\tau_i}^{\tau_f} \mathcal{L}(\Psi_r^*) d\tau \right]$$
 (3.14)

where Ψ_r^* denotes the most probable path of Ψ_r . It should be mentioned that the solution of (3.14) is only the first-order approximation of (3.7) and improvements made by higher order approximations are left for future work. The second order approximation would involve a second order functional expansion of the functional in (3.14). Ref. [87] outlines this well for the interested reader. Finally, it is worth mentioning that the solution to (3.12) and (3.13) with traditional boundary value problem solvers such as MATLAB byp4c will require additional differentiation if each produced equation does not have the same order of highest derivative. In such a case, one must turn to other methods to approximate the solution to (3.11) such as with Ritz method; see [88] for more detailed information. However, for the case of the current quarter-car model, the highest derivative is uniformly equal to two.

3.2.3 Variation-Based Approach for Curvature Estimation

This section is focused on predicting the P-bifurcation of the PDF. P-bifurcation involves the change in location of PDF extrema and thus in the present study, the P-bifurcation is explored near the stationary point $\phi_f = 0$ due to symmetry in the probability distribution.

The formulation for the proposed algorithm is outlined in this section. Given the knowledge of the IPVA system dynamics demonstrated in the previous chapter while taking into account that only the pendulum will oscillate locally around nonzero values, it is apparent that the present system will have a monomodal PDF with respect to all states except ϕ if bifurcation is achieved. As such, one can look at the change in sign of the second derivative $\frac{\partial^2 p}{\partial \phi_f^2}$, given the first derivative $\frac{\partial p}{\partial \phi_f} = 0$, where the approximate value of p is given in (3.14) and $\phi_f = \phi(\tau_f)$. In a system with symmetry, one can look solely at the PDF around $\phi_f = 0$. Otherwise, one may choose a general ϕ_f of interest in which the second derivative should vanish.

To compute the derivatives, however, the WPI method would involve computing a surrogate model of p [89] where one would solve (3.12) for numerous paths, which can result in considerable computational costs. In this work, a more efficient approach based on the calculus of variations for determining the derivatives is developed, which of the formulation is derived as follows.

First, let us define all pseudo and true states as a vector $\mathbf{q} = \left[\mathbf{y}^T, \Psi_r', \boldsymbol{\lambda}^T, \left(\boldsymbol{\lambda}^T \right)' \right]^T$. Then rewrite (3.12) and (3.13) as

$$\mathbf{q}' = \mathbf{g}(\mathbf{q}),$$

$$\mathbf{q}(\tau_f) = \mathbf{q}_f,$$

$$\mathbf{q}(0) = \mathbf{q}_i \tag{3.15}$$

where \mathbf{g} is a nonlinear function of \mathbf{q} and only 14 of the boundary conditions can be specified. Then taking variation δ of (3.15) with respect to the boundary \mathbf{q}_f gives

$$\frac{\partial \mathbf{q}'}{\partial \mathbf{q}_f} \delta \mathbf{q}_f = \frac{\partial \mathbf{g}(\mathbf{q})}{\partial \mathbf{q}_f} \delta \mathbf{q}_f \tag{3.16}$$

After interchanging derivatives $\partial/\partial \mathbf{q_f}$ and $\partial/\partial \tau$ it becomes

$$\mathbf{u}' = \frac{\partial \mathbf{g}(\mathbf{q})}{\partial \mathbf{q}} \mathbf{u} \tag{3.17}$$

where $\mathbf{u} = [\mathbf{u}_1, \mathbf{u}_2, \dots, \mathbf{u}_n] = \frac{\partial \mathbf{q}}{\partial \mathbf{q}_f}$, with $\mathbf{u}_i \in \mathbb{R}^{n \times 1}$ for $i = 1, 2, \dots, n$. Then $\mathbf{u} \in \mathbb{R}^{n \times n}$ given $\mathbf{q} \in \mathbb{R}^{n \times 1}$, where n = 14 for the current problem. The necessary boundary conditions are

then simply

$$\mathbf{u}\left(\tau_{f}\right) = \mathbf{I}\tag{3.18}$$

where I denotes the identity matrix of size n. Similarly, taking variation of (3.17) one obtains

$$\mathbf{w}' = \left(\frac{\partial}{\partial \mathbf{q_f}} \otimes \frac{\partial \mathbf{g}(\mathbf{q})}{\partial \mathbf{q}}\right) (\mathbf{I} \otimes \mathbf{u}) + \frac{\partial \mathbf{g}}{\partial \mathbf{q}} \mathbf{w}$$
(3.19)

with $\mathbf{q}_f = \left[q_f^{(1)}, q_f^{(2)}, \cdots, q_f^{(n)}\right]^T$, $\frac{\partial}{\partial \mathbf{q}_f} = \left[\frac{\partial}{\partial q_f^{(1)}}, \frac{\partial}{\partial q_f^{(2)}}, \cdots, \frac{\partial}{\partial q_f^{(n)}}\right]$ where $q_f^{(i)}$ corresponds to the value of the *i*-th final state, $\mathbf{w} = \frac{\partial}{\partial \mathbf{q}_f} \otimes \mathbf{u}, \mathbf{w} \in \mathbb{R}^{n \times n^2}$ and \otimes is the Kronecker tensor product. The right boundary condition is then

$$\mathbf{w}\left(\tau_{f}\right) = \mathbf{0}\tag{3.20}$$

where **0** denotes the zero matrix of size $n \times n^2$. Solving (3.15)–(3.20) together, one can obtain the most probable path and its first and second variations.

Note that in the present case, the interest is only in $\frac{\partial^2 p}{\partial \phi_f^2}$. Suppose the *i*-th component q_i of \mathbf{q} corresponds to the pendulum angle ϕ , i.e., $q_i = \phi$, then set $\mathbf{u}_i = \mathbf{v}$ and only solve $\mathbf{v}' = \frac{\partial \mathbf{g}}{\partial \mathbf{q}} \mathbf{v}$ in (3.17) and set $\hat{\mathbf{w}} = \frac{\partial \mathbf{v}}{\partial \phi_f}$. Then in indicial notation, the variational equations are given by

$$v'_{l} = \frac{\partial g_{l}(\mathbf{q})}{\partial q_{k}} v_{k}$$

$$\hat{w}'_{l} = \frac{\partial^{2} g_{l}(\mathbf{q})}{\partial q_{j} \partial q_{k}} v_{k} v_{j} + \frac{\partial g_{l}(\mathbf{q})}{\partial q_{j}} \hat{w}_{j}, j, k, l = 1, 2, \dots, n$$
(3.21)

where the subscript l denotes the l-th component. One then has the following boundary conditions

$$v_l(\tau_f) = \delta_{li}$$

$$\hat{w}_l(\tau_f) = 0, l = 1, 2, \dots, n$$
(3.22)

where Einstein summation is employed, i is the index corresponding to ϕ_f and δ_{li} is the Kronecker delta function. Finally, taking the derivative of (3.14) with respect to ϕ_f , one

obtains

$$\frac{\partial p}{\partial \phi_f} = -p \int_0^{\tau_f} \frac{\partial \mathcal{L}}{\partial \phi_f} d\tau \tag{3.23}$$

, while the second derivative gives

$$\frac{\partial^2 p}{\partial \phi_f^2} = p \left[\left(\int_0^{\tau_f} \frac{\partial \mathcal{L}}{\partial \phi_f} d\tau \right)^2 - \int_0^{\tau_f} \frac{\partial^2 \mathcal{L}}{\partial \phi_f^2} d\tau \right]$$
(3.24)

where $\frac{\partial \mathcal{L}}{\partial \phi_f} = \frac{\Psi_r'}{d} \frac{\partial \Psi_r'}{\partial \phi_f}$ and $\frac{\partial^2 \mathcal{L}}{\partial \phi_f^2} = \frac{1}{d} \left(\frac{\partial \Psi_r'}{\partial \phi_f} \right)^2 + \frac{\Psi_r'}{d} \frac{\partial^2 \Psi_r'}{\partial \phi_f^2}$. Note that Ψ_r' , $\frac{\partial \Psi_r'}{\partial \phi_f}$, and $\frac{\partial^2 \Psi_r'}{\partial \phi_f^2}$ are solutions obtained from solving (3.15), (3.21) and (3.22) together. Also, we have the cutoff frequency $v_c = 0$ as it is unnecessary in the context of computing the PDF approximation and derivatives. When the PDF is stationary one can further note that $\frac{\partial p}{\partial \phi_f} |_{\phi_f = 0} \approx 0$ as the current system has a symmetric PDF about the origin and a maximum or minimum is bound to occur at the center of symmetry. Furthermore, if $\frac{\partial^2 p}{\partial \phi_f^2} |_{\phi_f = 0} \neq 0$, the ratio

$$\beta = \frac{\frac{\partial p}{\partial \phi_f} \Big| \phi_f = 0}{\frac{\partial^2 p}{\partial \phi_f^2} \Big| \phi_f = 0}$$
(3.25)

can be used as a measure of convergence where smaller $|\beta|$ implies better convergence.

Now that the equations are defined. Fig. 3.2 is the pseudocode for the proposed WPI algorithm. There are a few things to note in the proposed algorithm. First, (3.12) will naturally give a system in which negative damping proportional to ξ_e and ξ exists due to the term $-\frac{d}{d\tau} \frac{\partial \mathcal{L}^*}{\partial \mathbf{x}'}$. This makes the system unstable with forward marching schemes such as one used with the shooting method [90]. Additionally, it had proven to be difficult to find a suitable initial solution guess that allowed for sufficient convergence using the collocation method with solvers such as $MATLAB\ bvp4c$.

The authors have overcome this difficulty with the following procedure. Perform a backward integration initially with $\xi_e = 0$. For the initial conditions, choose all final states $\mathbf{y}(\tau_f) = 0$ because the interest is in examining the PDF when all final states are trivial as the current system has a symmetric PDF. For other cases, the final states should be chosen to reflect the PDF location of interest. Out of seven final pseudo-states, $[\Psi'_r(\tau_f), \boldsymbol{\lambda}^T(\tau_f), \boldsymbol{\lambda}'^T(\tau_f)]$,

choose one nonzero but small value such that the solution remains bounded on the time interval $[0, \tau_f]$. The remaining final pseudo-states are set to zero. Ultimately, for sufficiently long integration, it is assumed that the response process is well mixed such that the initial states become all immaterial and do not affect the stationary PDF. They are consequentially left to be determined from the solution process. Finally, this solution is used as an initial guess for the solution corresponding to small, but nonzero ξ_e using the collocation method with an appropriate boundary value problem (bvp) solver.

Next, the algorithm takes a perturbation-based approach which accelerates the solution convergence. As such, following a small perturbation of parameters, the preceding solution is used as the initial guess for the current solution. This is done in an iterative fashion. Additionally, it was determined that some dependent variables may grow unbounded and result in failure or inefficiency in computation. This was remedied by setting a maximum dependent variable value of σ and then multiplying the solution time vector by some factor N < 1 before passing the solution as the initial guess for the next iteration wherein the integration time is shortened by the same factor N. Lastly, the algorithm only saves $\frac{\partial^2 p}{\partial \phi_f^2} |_{\phi_f=0}$ if $|\beta|$ is smaller than some specified tolerance β_{ub} , implying sufficient convergence. In general, $\beta_{ub} \ll 1$. In practice, it is recommended to initially store all values of $\frac{\partial^2 p}{\partial \phi_f^2} |_{\phi_f=0}$ to allow for the flexibility in changing β_{ub} based on the qualitative trends in the solutions. If many outliers exist, the tolerance is decreased. If not enough solution points meet the tolerance constraint, the tolerance is increased. A compromise is thereby determined.

3.3 Parametric Study and Performance Evaluation

3.3.1 One-Parameter P-bifurcation

With the curvature estimated method formulated in the previous section, the focus now moves on to the parametric study wherein the pendulum length parameter η is varied and the performance metrics given by power harvested, sprung mass acceleration and road handling are quantified.

For the variation in η study, start by assigning the dimensionless parameters given in

```
1: function WPIALGORITHM
         Define variable parameters: \Gamma_v^T = [\xi_e, \alpha_v^T]
 2:
         Set varying parameter initial values: \Gamma_{v,0} = [0, \alpha_{v,0}^T]^T
 3:
         Set domain: \Gamma_v \in [\Gamma_{v,L}, \Gamma_{v,R}], \Gamma_{v,L} \leq \Gamma_{v,0} \leq \Gamma_{v,R}
 4:
         Set fixed parameter values: \Gamma_f = \Gamma_{f,0}
 5:
         Set \mathbf{y}(\tau_f) = 0
 6:
         [\Psi_r'(\tau_f), \boldsymbol{\lambda}^T(\tau_f), \boldsymbol{\lambda}'^T(\tau_f)]^T = [\Psi_r'(\tau_f)_f, \boldsymbol{\lambda}^T(\tau_f)_f, \boldsymbol{\lambda}'^T(\tau_f)_f]^T,
 7:
         Solve (3.15), (3.21), and (3.22) together using backwards integration.
 8:
         sol = solution to boundary value problems
 9:
         sol.z = state solution vector
10:
         sol.time = time vector
11:
12:
         BC = True States and Variations at \tau = \tau_f and Pseudo-States at \tau = 0
13:
         while \Gamma_{v,L} \leq \Gamma_v \leq \Gamma_{v,R} do
              \Gamma_v = \Gamma_v + \epsilon
                                                                   \triangleright \epsilon is a small perturbation in parameters
14:
15:
              N \in (0,1)
                                                                                                      \sigma = \text{maximum desired value for any dependent variable}
16:
              while solution not obtained do
17:
                   Solve (3.15) and (3.21) with BC and sol as guess for collocation method with
18:
    any bvp solver, e.g., MATLAB bvp4c
                   if by solver fails (singularity in Jacobian of collocation equations) or does
19:
    not finish in a reasonable time then
                       \text{sol.time} = N \cdot \text{sol.time}
20:
                       solution not obtained
21:
22:
                   end if
23:
              end while
24:
              sol = solution obtained
              if \sigma < \max(\text{sol.z}) then
25:
                   sol.time = N \cdot sol.time
26:
              end if
27:
              save sol
                                                                                                 ▶ Save the solution
28:
              set \beta_{ub} \ll 1
                                                                                              \triangleright Upper bound of |\beta|
29:
              if |\beta| < \beta_{ub} then
30:
                  save \frac{\partial^2 p}{\partial \phi_f^2} \Big|_{\phi_f = 0}
                                                                            ▶ Save the second derivative value,
31:
32:
              end if
         end while
33:
34: end function
```

Figure 3.2 Pseudocode for WPI Algorithm.

(3.1) numerical values which can be reasonably correlated with a passenger car and a random excitation intensity correlated with a class C road as defined in [86]. As such, all dimensionless parameter values with the exception of μ_g given in Table 3.1 have been derived from recent work in [62]. Additionally, in this chapter, V = 113 km/hr which serves as a reason-

able upper bound for a passenger car driving on an average road. Also, note that the value of dimensionless μ_g was determined by considering the Maxon 353300 DC motor which has a rated power of 250W with a gearbox giving a 3.8:1 ratio, so that the speed would be in the nominal range. The motor also has an internal resistance $R_{int} = 1.06\Omega$ which will be needed when accounting for electrical efficiency. Some important physical parameters were then

| Parameters, Dimensionless | Value |
|---------------------------|-----------|
| μ_r | 0.1521 |
| $\mu_g \ \xi$ | 0.0194511 |
| ξ | .02 |
| ξ_e | 0.0337 |
| u | 0.14 |
| v | 4.4137 |
| d | .0806 |

Table 3.1 Dimensionless Parameters of IPVA system.

determined by assuming the ball screw lead value of L=100 millimeters. From companies such as THK Co., Ltd., this appears to be the largest value immediately offered. A large lead value will help keep the dimensionless intensity at a minimum when rougher roads are considered later on. Some physical parameters are given in Table 3.2. Starting with the

| Parameters | Value | Meaning |
|------------|---|-----------------------------|
| M_s | 374 kg | Sprung Mass |
| M_{us} | 52.36 kg | Unsprung Mass |
| k_t | 248,085 N/m | Tire stiffness |
| k_s | 90,963 N/m | Suspension stiffness |
| R_p | .05 m | Carrier radius |
| m | 3.74 kg | Mass of pendulum |
| c_m | 233.74 Ns/m | Mechanical damping |
| V | 31.3 m/s | Driving speed |
| G_r | $64/(2\pi)^2 \times 10^{-6} \text{ m} \cdot \text{cycle}$ | Road roughness coefficient |
| R | $.1/(2\pi) \text{ m}$ | Effective ball screw radius |
| κ | 0.207 Nm/A | Motor torque constant |
| R_{int} | 1.06Ω | Motor internal resistance |

Table 3.2 Phyical Parameters of IPVA system.

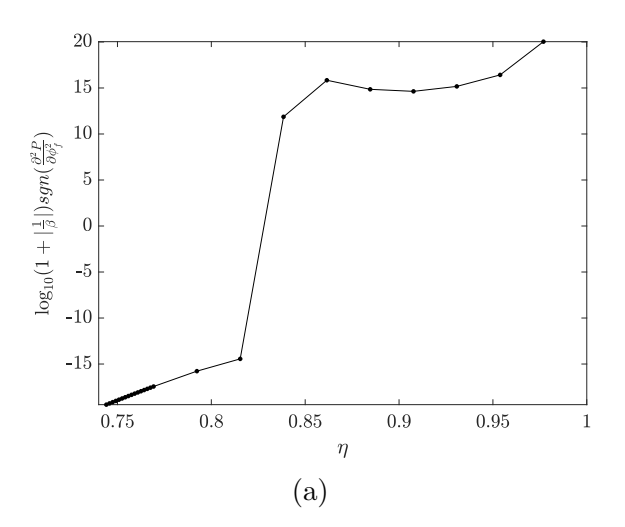
WPI method introduced in the previous section, $\operatorname{sgn}\left(\frac{\partial^2 p}{\partial \phi_f^2}\right) \log_{10}\left(1+\left|\frac{1}{\beta}\right|\right)$ is plotted against

dimensionless pendulum length η in Fig. 3.3a. This function was chosen to clearly show the qualitative characteristics of the second derivative of the marginal PDF as the magnitudes of the second derivative vary drastically. Additionally, β^{-1} is used in place of the second derivative in order to eliminate the unknown integration constant C.

In Fig. 3.3a there is a clear indication that the sign turns positive as η is increased past 0.84. This indicates an increase in curvature and more importantly a bimodal probability density function. This is verified with the marginal PDF plot for ϕ in Fig. 3.3b, obtained via an MCS with $\sim 7 \cdot 10^4$ realizations. Note that a marginal PDF is generally obtained by integrating the PDF with respect to all variables besides the variable of interest. The PDF is then normalized with respect to the entire integral such that the total probability is unity. The marginal PDF of ϕ is chosen in this work as this is where the bimodal distribution is clearly seen. The marginal PDF then simply gives the probability distribution for the pendulum angular position relative to the carrier. In this case, it is clear that the PDF becomes bimodal after $\eta=0.7$. For $\eta=0.9$, the PDF has two distinct peaks. It should also be noted that a 50-second integration time was chosen to ensure that the approximate solution for the second derivative was close to stationary and reasonably accurate in a qualitative sense. While lower integration times of only 10 seconds were tried initially (not shown in this work), they were qualitatively accurate only for subzero curvature solutions. However, this fact has been exploited by the authors in the bifurcation analysis later on in Sec. 3.4. i.e. the initial integration time is decreased in the case of low electrical damping as this most likely will result in rotation of the pendulum and thus near-zero and possibly negative curvature. This helps immensely with the efficiency of the algorithm. Next, we will examine how the P-bifurcation influences the suspension performance.

3.3.2 Multi-objective Suspension Performance

The power from the IPVA into the electrical domain (P_{nl}) is directly proportional to generator velocity squared, where the proportionality constant is the electrical damping coefficient $c_e = \kappa^2 n_g^2 / R_e$. Here κ is the torque constant of the motor, n_g is the gear ratio



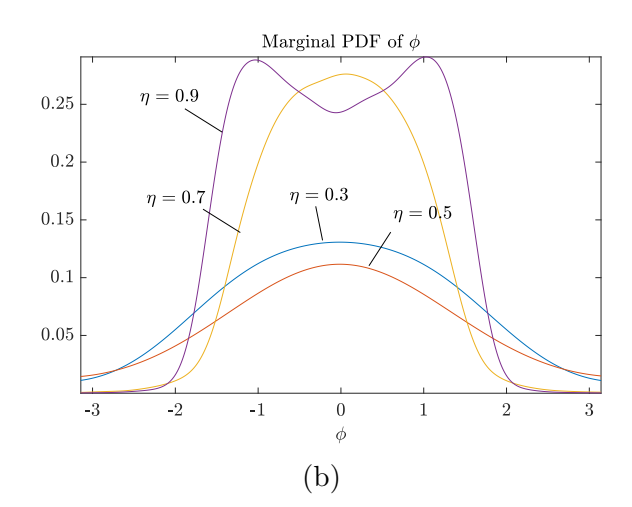


Figure 3.3 (a) Logarithm of the scaled and shifted magnitude of the second derivative of the marginal PDF vs. η . The integration time is 50 seconds. (b) Marginal PDF for pendulum angle ϕ for various η values.

and R_e is the total electrical resistance [91]. The expected value of the electrical power is then just

$$P_{nl} = E \left[c_e \left(\dot{\theta} - \dot{\phi} \right)^2 \right] \tag{3.26}$$

and in dimensionless form it is

$$\hat{P}_{nl} = E \left[\xi_e \left(\theta' - \phi' \right)^2 \right] \tag{3.27}$$

Upon consideration of losses due to internal resistance, one can write the expected value of the harvested dimensionless power $\hat{P}_{nl,H}$ as

$$\hat{P}_{nl,H} = E \left[\frac{R_l}{R_l + R_{int}} \xi_e \left(\theta' - \phi' \right)^2 \right]$$
(3.28)

where ξ_e now represents the electrical damping coefficient with internal electrical resistance R_{int} as well as load resistance R_l . R_l can further be written in terms of ξ_e so that (3.28) becomes

$$\hat{P}_{nl,H} = E\left[\left(\xi_e - \frac{2R^2 \omega_0 R_{int} M_s}{\kappa^2 n_g^2} \xi_e^2 \right) (\theta' - \phi')^2 \right]$$
(3.29)

It is apparent from (3.29) that losses can be reduced with a decrease in internal resistance R_{int} which should have a large influence on the choice of generator.

The formula for the linear system mean power corresponding to the case of locked pendulum such that $\phi = \phi' = 0$ is identical to that derived in [62] and is given here.

$$P_l = \frac{c_e \pi G_r V k_t}{c_e + c_m R^2} \tag{3.30}$$

In a similar fashion to the nonlinear case, the linear system dimensionless mean power can be written with electrical efficiency considerations as

$$\hat{P}_{l,H} = \eta_e \frac{\xi_e duv^2}{4(\xi_e + \xi_m)} \tag{3.31}$$

where electrical efficiency η_e is given by

$$\eta_e = \frac{R_l}{R_l + R_{int}} \tag{3.32}$$

For the linear system, there exists an optimal load resistance giving optimal harvested power $\hat{P}_{l,H}^{opt}$. For a given set of parameters, this can be determined via $\frac{\partial \hat{P}_{l}}{\partial R_{l}} = 0$. Substituting the optimal load resistance in (3.31), one arrives at

$$\hat{P}_{l,H}^{opt} = \frac{d\kappa^2 u v^2 n_g^2 \sqrt{\kappa^2 n_g^2 + 2R^2 \omega_0 R_{int} \xi_m M_s}}{(A)(B)}$$
(3.33)

where

$$A = 2\sqrt{2} \left(\sqrt{2\kappa^2 n_g^2 + 4\xi_m R^2 \omega_0 R_{int} M_s} + 2R\sqrt{\xi_m \omega_0 R_{int} M_s} \right)$$

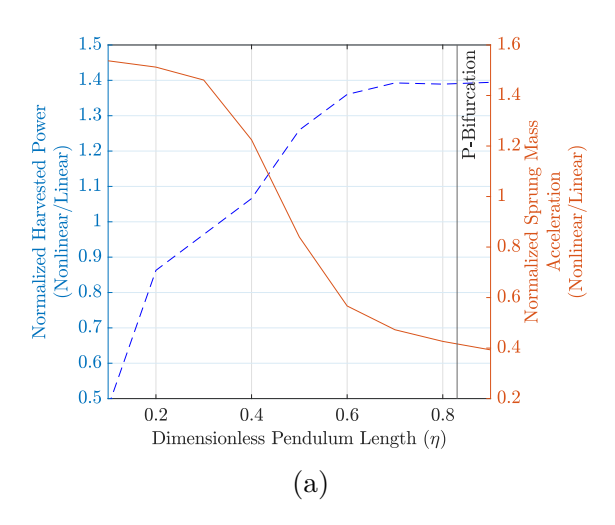
$$B = \kappa^2 n_g^2 + \sqrt{2}R\sqrt{\xi_m \omega_0 R_{int} M_s \left(\kappa^2 n_g^2 + 2\xi_m R^2 \omega_0 R_{int} M_s\right)}$$

$$+ 2\xi_m R^2 \omega_0 R_{int} M_s$$

$$(3.34)$$

Now the mean electrical power is plotted against η in Fig. 3.4a, normalized with respect to the optimal linear system. Given an optimized linear system with a mean power of $P_l = 21.0932$ Watts, a clear increase of 40% is shown in Fig. 3.4a for $\eta = 0.9$, in the bimodal regime.

In order to quantify ride comfort, Fig. 3.4a also shows the root mean square (RMS) sprung mass acceleration normalized with respect to the linear system. The detailed derivation of the root mean square sprung mass acceleration for the linear system with no pendulum



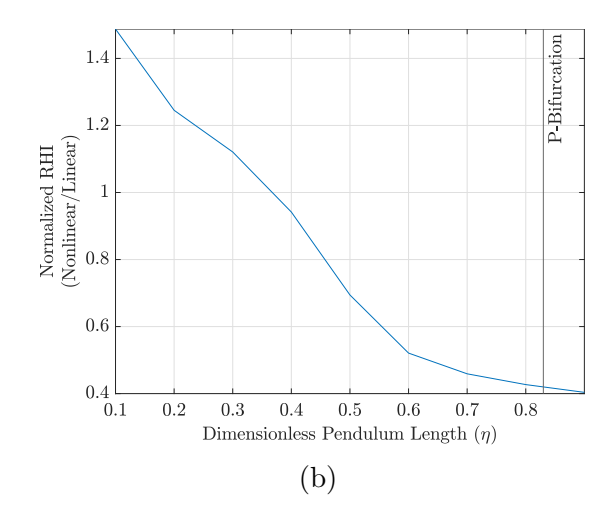


Figure 3.4 (a) Harvested power and RMS sprung mass acceleration vs. η for the proposed IPVA-integrated system, normalized with the optimal linear benchmark system. Note that $P_{l,H}^{opt} = 21.0932$ W, and the electrical efficiency of the nonlinear system is 83%. (b) Road handling index vs. η for the proposed IPVA-integrated system normalized with respect to linear system $\gamma_{RHI,l}$. Solid vertical line indicates P-bifurcation.

is given in [62]. Note that as the present work considers a locked pendulum rather than no pendulum at all, the solution is slightly different than in [62]. However, the solution procedure is the same and the solution is omitted here for brevity. It is clear from Fig. 3.4a that the ride comfort improves with an increase in pendulum length parameter η . There is an approximate 60% reduction for $\eta = 0.9$. It is finally noted that the simultaneous optimization of power and ride comfort is a major hallmark of the current design; the non-linearity allows for simultaneous objectives which are otherwise competing when the linear system is used [92].

Another metric worth exploring is the road handling index (RHI)[86] which will be given the symbol γ_{RHI} in this paper. This is the ratio of root mean square dynamic tire force to static weight from the car. Lower numbers indicate safer driving conditions as the car makes better contact with the road. This mathematically is stated as

$$\gamma_{RHI} = \text{RMS}\left(\frac{k_t R \left(\psi_{us} - \Psi_r\right)}{\left(M_{us} + M_s\right) g}\right)$$
(3.35)

where RMS(·) denotes the root mean square value of "·" and g is the acceleration due to gravity. This quantity normalized with respect to the linear system value $\gamma_{RHI,l}$ is plotted vs

 η in Fig. 3.4b. Note that the detailed formulation of the linear system road handling index is given in Appendix D. With the IPVA system, there is apparently simultaneous improvement in γ_{RHI} for larger η when the system is bimodal. It should finally be noted that the P-bifurcation condition with bifurcation parameter η does not guarantee optimal harvested power, sprung mass acceleration, or road handling. However, it serves as a suitable starting point for further optimization with respect to η . Note that the power harvested seems to approach a horizontal asymptote near this P-bifurcation in Fig. 3.4a. In this case, it is quickly discovered that larger choices of η are desired as the other metrics continue to improve.

Returning to the subject of power, let us investigate power generation further with power spectral density (PSD) analysis. The PSD associated with the generator velocity is plotted vs. normalized frequency ω/ω_0 for the monomodal system in Fig. 3.5a and the bimodal system in Fig. 3.5b. Note that the two natural frequencies ω_{n1} and ω_{n2} of the linear system with locked pendulum $\eta=0.9$ have been determined to be $0.74\omega_0$ and $2.54\omega_0$, respectively. It is then noted, that for both η cases the introduction of the IPVA has the effect of annihilating ω_{n2} which simultaneously has the effect of broadening the effective bandwidth of operation. Also, as the power harvested is directly proportional to the area under the curve, both cases show improvement over the linear system while power is notably increased in the bimodal case. Specifically, for $\omega/\omega_0 < 1$ and $\omega/\omega_0 > 3$ the total area is noticeably larger. Therefore, these high-frequency and low-frequency areas are responsible for significant improvements in energy harvesting. In fact, the total area increase for the frequency range shown is 23% for the monomodal case and 34% for the bimodal case.

3.3.3 Energy Flow

The power input to the IPVA, each component in the IPVA, and the electrical domain are analyzed in this section to better understand the energy flow in the system as a function of η .

Starting with the power input to the IPVA (P_{IPVA}) , the result derived in [62] is used.

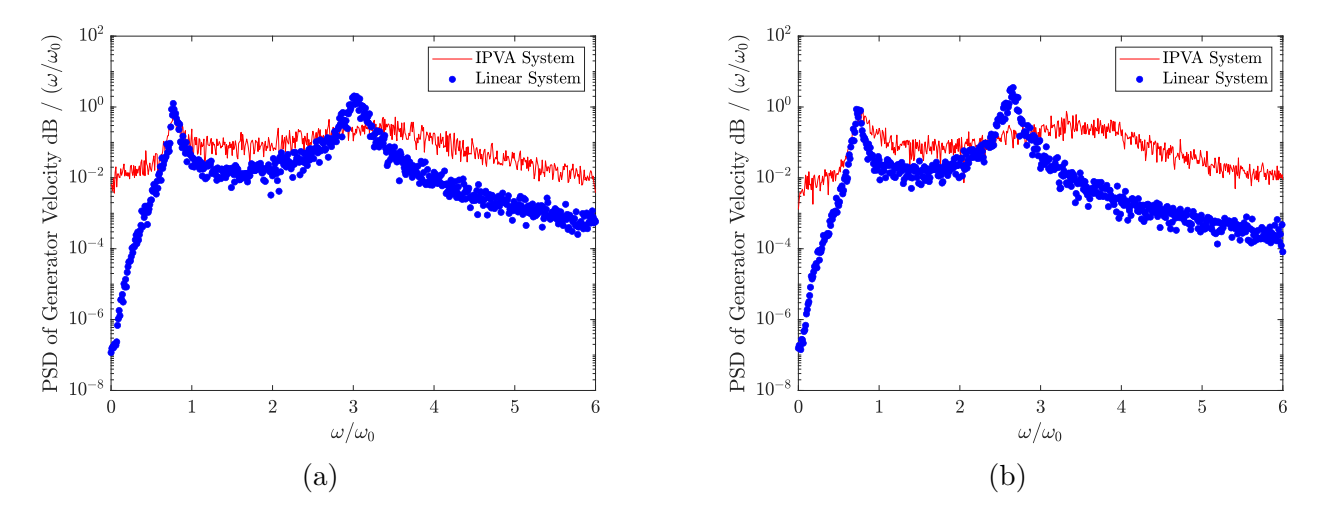


Figure 3.5 (a) Power spectral density of the generator velocity. $\eta = 0.5$. (b) Power spectral density of the generator velocity. $\eta = 0.9$. $\omega_0 = \sqrt{k_s/M_s}$.

Namely,

$$P_{IPVA} = -\left(M_s \ddot{x}_s + c_m R \dot{\theta} + k_s R \theta\right) R \dot{\theta} \tag{3.36}$$

To determine the power input to the pendulum (T_c) first write the energy in physical units as

$$T_c = \frac{1}{2}m\left(R_p^2\dot{\theta}^2 + r^2\left(\dot{\theta} + \dot{\phi}\right)^2 + 2R_pr\cos\left(\phi\right)\dot{\theta}\left(\dot{\theta} + \dot{\phi}\right)\right)$$
(3.37)

Then the power input to the pendulum, $P_p = \frac{dT_c}{dt}$, is simply

$$P_{p} = m \left[r^{2} \left(\dot{\theta} + \dot{\phi} \right) \left(\ddot{\theta} + \ddot{\phi} \right) - r R_{p} \dot{\theta} \dot{\phi} \sin(\phi) \left(\dot{\theta} + \dot{\phi} \right) \right.$$
$$\left. + r R_{p} \dot{\theta} \cos(\phi) \left(\ddot{\theta} + \ddot{\phi} \right) + r R_{p} \ddot{\theta} \cos(\phi) \left(\dot{\theta} + \dot{\phi} \right) + R_{p}^{2} \dot{\theta} \ddot{\theta} \right]$$
(3.38)

The mechanical energy of the generator rotor is then

$$T_g = \frac{J_g n_g^2}{2} \left(\dot{\theta} - \dot{\phi} \right)^2 \tag{3.39}$$

and the power is

$$P_g = J_g n_g^2 \left(\dot{\theta} - \dot{\phi} \right) \left(\ddot{\theta} - \ddot{\phi} \right) \tag{3.40}$$

Finally, the expected value of power into the electrical domain is given in (3.26). Note that the second derivatives in (3.36), (3.38) and (3.40) are written in terms of the system states as determined by (3.2-3.4) before they are made dimensionless. The substitutions are omitted

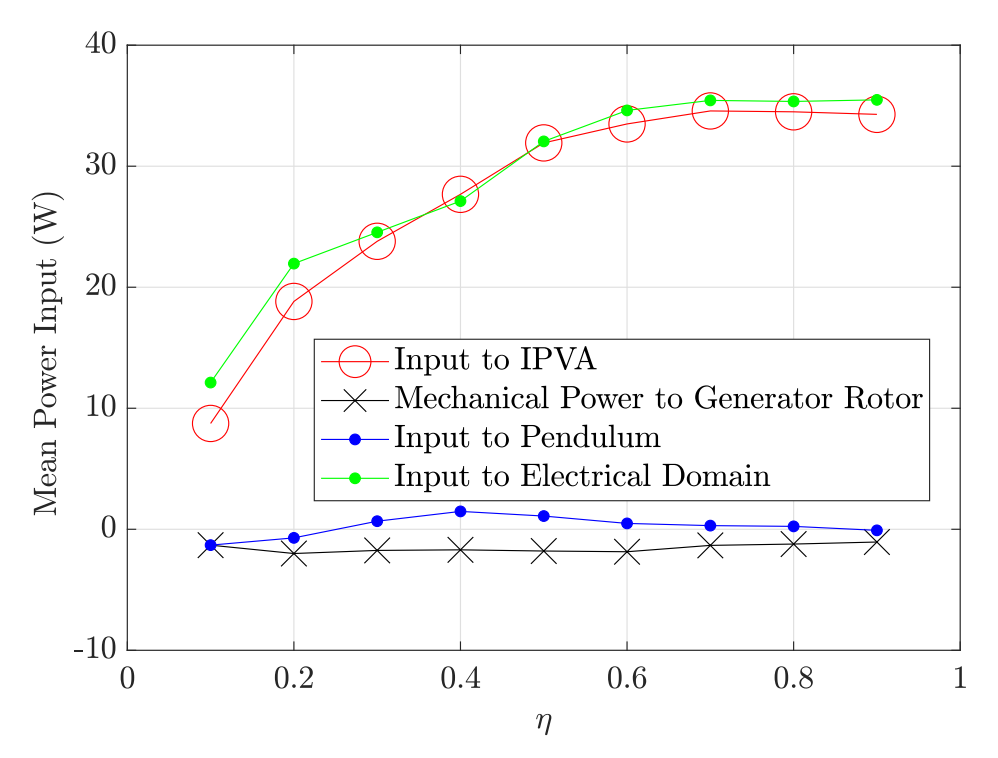


Figure 3.6 Mean input power into IPVA, generator rotor, pendulum, and electrical domain vs. η .

here as they are too lengthy. For a range of η , the mean powers are then estimated with the statistical expectation derived from an ensemble of $\sim 7 \cdot 10^4$ realizations. The results are shown in Fig. 3.6. It is apparent that for all η , most of the energy that is input to the IPVA flows into the electrical domain. The total power also increases with an increase in the dimensionless pendulum length η . Additionally, there is practically zero net energy flow in the pendulum and generator rotor. These components are acting to only transfer the power into the electrical domain.

3.4 Two-parameter P-bifurcation and Performance Evaluation Around the Bifurcation Boundary

As demonstrated in Sec. 3.3, the P-bifurcation is critical to the suspension performance. Therefore, we study it in-depth in this section. Now that the WPI algorithm efficiently estimates $\frac{\partial^2 p}{\partial \phi_f^2}$, a simple bifurcation detection algorithm which checks for change in sgn $\left(\frac{\partial^2 p}{\partial \phi_f^2}\right)$ is implemented. Note that for this study, the dimensionless pendulum length is set to $\eta = 0.97$ as it was shown in the preceding section that large pendulum lengths might be

correlated with energy transfer. Also, to allow for rotation one must have $\eta < 1$. For $\eta > 1$, the pendulum will collide with the ball screw. Also, the sign change is determined as a

| Parameters | Value | Meaning |
|------------|-----------------------|-----------------------------|
| M_s | 374 kg | Sprung Mass |
| M_{us} | 52.36 kg | Unsprung Mass |
| k_t | 300263 N/m | Tire stiffness |
| k_s | $110095~\mathrm{N/m}$ | Suspension stiffness |
| R_p | $.062 \mathrm{\ m}$ | Carrier radius |
| m | 3.74 kg | Mass of pendulum |
| c_m | 256.67 Ns/m | Mechanical damping |
| R | $.1/(2\pi) \text{ m}$ | Effective ball screw radius |
| κ | 0.207 Nm/A | Motor torque constant |
| R_{int} | 1.06 Ω | Motor internal resistance |

Table 3.3 Physical Parameters of the IPVA System on Rough Class F Road.

function of dimensionless noise intensity (d) and electrical damping ratio ξ_e . For this study, some physical parameters are also given in Table 5.1. Note that the suspension stiffness and tire stiffness has been increased in this case to allow for d < 0.9 when traveling on a rough class F road with a velocity of 5 m/s while keeping all dimensionless parameters (excluding d and ξ_e) the same as in Table 3.1.

Using the developed WPI-based curvature estimation algorithm, a bifurcation curve has been produced and is shown in Fig. 3.7a. Three distinct regions have been determined based on the WPI approximation and verified with an MCS of $\sim 3.6 \cdot 10^4$ realizations and a simulation time of $\tau = 1000$ for a few different car velocities and damping values. Given a parameter set in region I, the system is expected to primarily exhibit rotation and thus the PDF will have near-zero curvature at $\phi = 0$. Region II and III then correspond to monomodal and bimodal PDFs, respectively, while it should be noted that rotations in region II are still possible. In the case of rotations in region II, oscillations are likely to occur near $\phi = 2\pi k$ following rotation, where k is an integer. It should finally be noted that the dashed line was estimated with the use of the MCS. The dashed line prediction was necessary as no detectable change in the sign was determined with the WPI approximation and convergence

criteria used in the algorithm. Additionally, the noise intensity stops at around d = 0.9 as it was proven difficult to observe any further qualitative distinctions past this point given the fact that rotation is highly probable.

To demonstrate these assertions, let us define the value of ξ_e lying on the bifurcation curve to be $\xi_{e,bif}$ and $\xi_e \in [0.5\xi_{e,bif}, 1.5\xi_{e,bif}]$. Then the marginal PDFs for pendulum angle ϕ for three distinct velocities corresponding to bifurcation points in the bifurcation diagram are shown in Figs. 3.7b-3.7d. Note that the PDFs extend to very large angles in the positive and negative directions. The domain has been cropped only for visualization near the origin and the area under all PDFs for the entire domain is in fact equal to unity. Next, note that Figs. 3.7b and 3.7c correspond to the case of the PDF transitioning between bimodal and monomodal (region III to region II) when the driving speed is $V=0.1973~\mathrm{m/s}$ and V = 0.5371 m/s respectively. In both cases, a PDF with near zero curvature at the approximate bifurcation point is apparent. A major difference is then in the bimodal PDFs where the larger velocity leads to a larger distance between peaks. Moving to Fig. 3.7d one sees the case of the PDF transitioning between monomodal and pure rotation (region II to region I) when the driving speed is V = 2.6432 m/s. In this case, it is interesting to note that the PDF at the approximate bifurcation point actually takes the form of what appears to be a monomodal type whose curvature is nearly zero at the origin. While it has proven to be too difficult to numerically verify this curvature with the use of the MCS for sufficient accuracy, one can easily see that the MCS results in a PDF at the predicted bifurcation point which indeed is qualitatively different than the others, indicating a transition. Hence, WPI has given a reasonable bifurcation prediction.

3.4.1 Performance Around P-bifurcation

In this section, we look at performance as a function of driving speed on a class F road in the neighborhood of P-bifurcation. As a reminder, the dimensionless noise intensity is $d = \frac{2\pi G_r V}{\omega_0 R^2}$ where for a class F road, one has $G_r = 4096/(2\pi)^2 \times 10^{-6}$ m· cycle [86]. As a result, one may vary d by varying the driving speed V. It should be noted that d is also

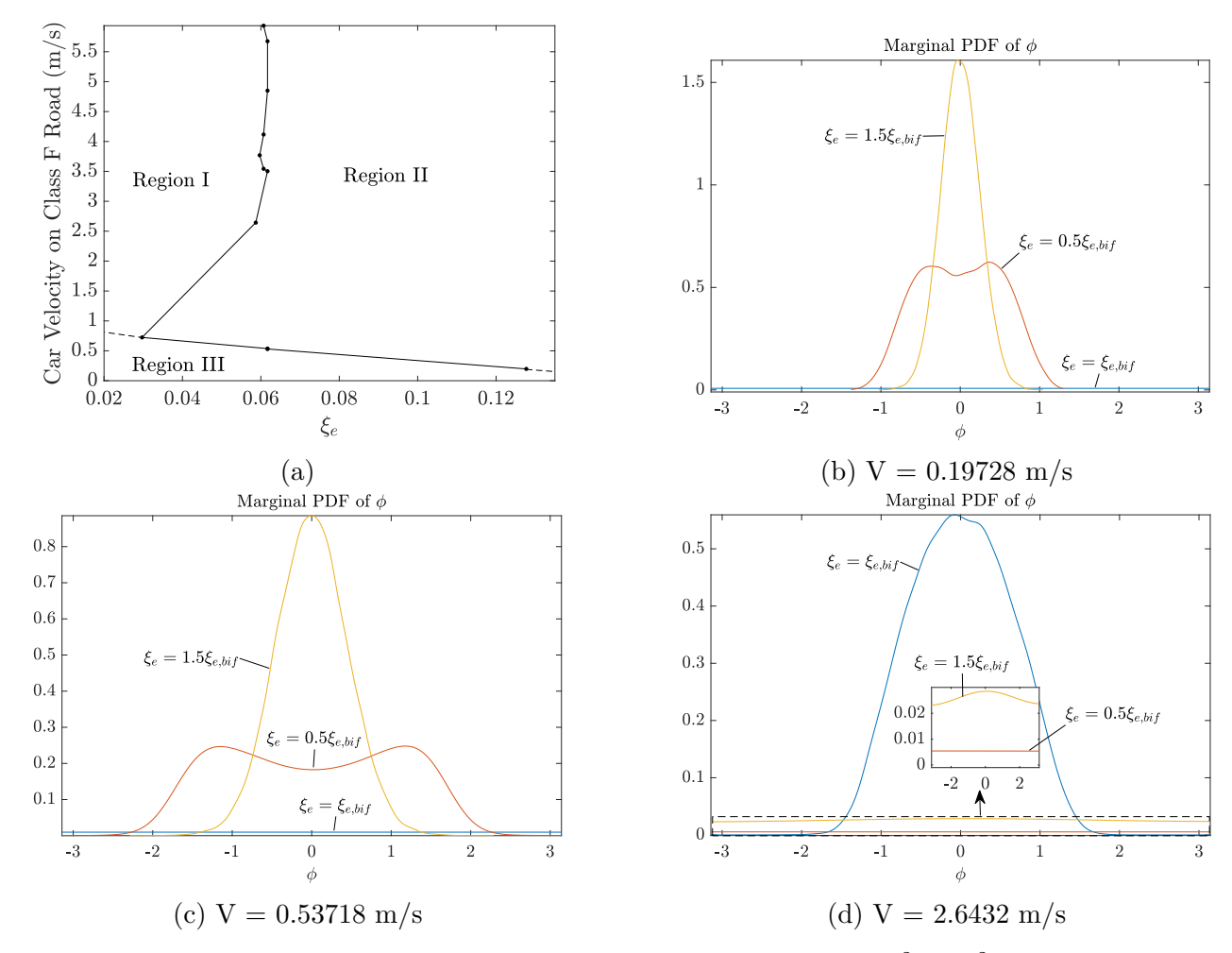


Figure 3.7 (a) Bifurcation boundaries in d vs. ξ_e plane. Region I: $\partial^2 p/\partial \phi_f^2 \approx 0$ with certain rotation. Region II: $\partial^2 p/\partial \phi_f^2 < 0$, monomodal oscillations and possible rotation. Region III: $\partial^2 p/\partial \phi_f^2 > 0$, bimodal and rotation is less likely. The dashed line is an MCS prediction. (b) PDF transition from region III to II with V = 0.19728 m/s. (c) PDF transition from region III to II with V = 2.6432 m/s.

linearly proportional to G_r and so one might interpret the results in this section as a function of road class with constant velocity if they wish. Furthermore, note that an upper limit of driving speed V = 6 m/s is chosen because a class F road means a very rough off-road style terrain. Driving speeds are generally low on off-road terrain for safety and to prevent damage to the vehicle suspension.

Using (3.33) one can obtain the physical optimal power $P_{l,H}^{opt}$ with

$$P_{lH}^{opt} = 2M_s \omega_0^3 R^2 \hat{P}_{lH}^{opt} \tag{3.41}$$

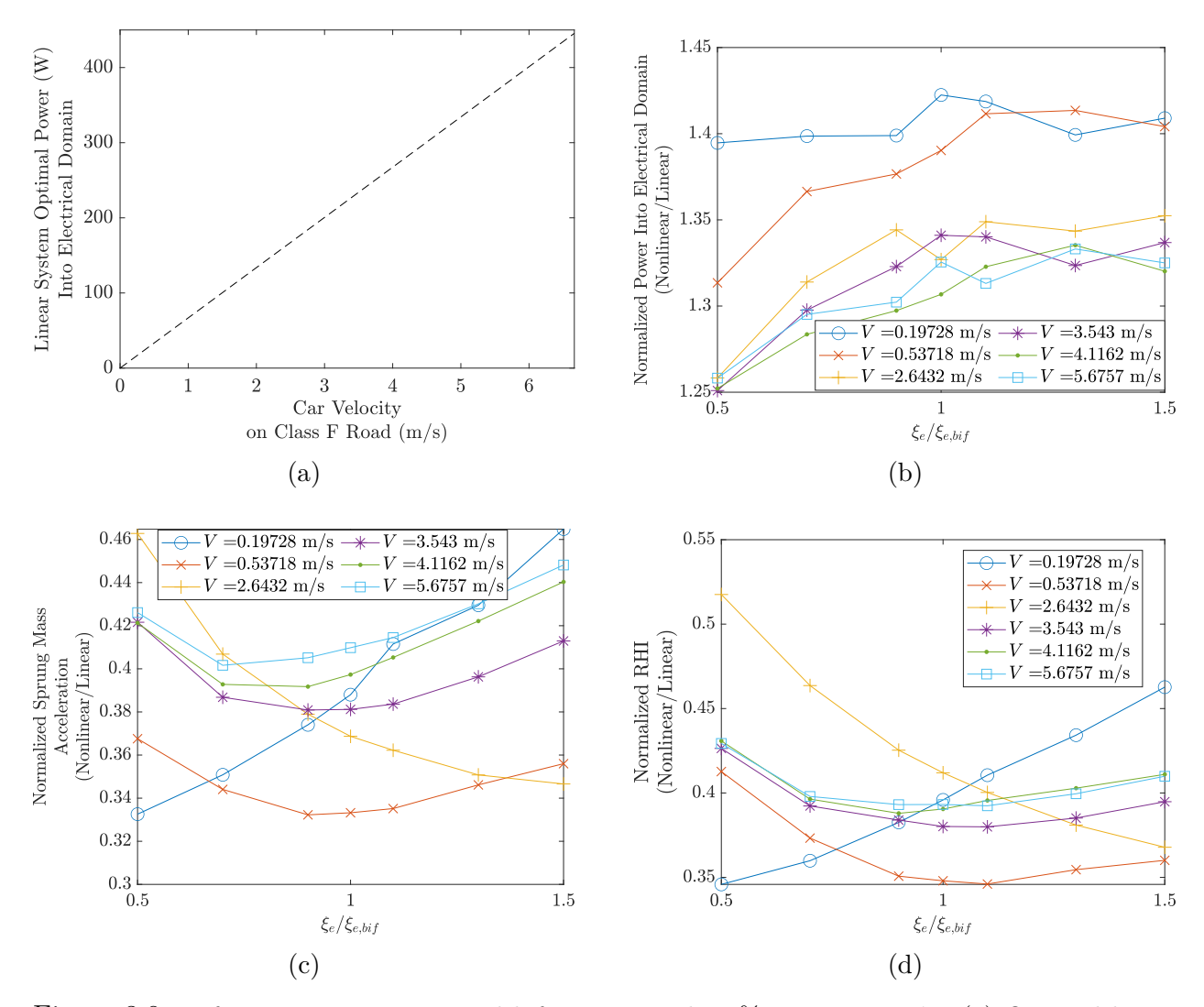


Figure 3.8 Performance metrics around bifurcation with 50% variation in ξ_e . (a) Optimal linear system power into the electrical domain. (b) Nonlinear system mean power into the electrical domain normalized with the optimal linear system. (c) Nonlinear system RMS sprung mass acceleration normalized with the optimal linear system. (d) Nonlinear system RHI normalized with the optimal linear system.

The total power into the electrical domain for the optimized linear system is then

$$P_l^{opt} = \frac{P_{l,H}^{opt}}{\eta_e} \tag{3.42}$$

The optimized linear system power that flows into the electrical domain is then shown in Fig. 3.8a as a function of driving speed. This optimal system will now be used in normalization to evaluate the performance of the nonlinear system around the bifurcation curve shown in Fig. 3.7a. Let us now restrict our electrical damping domain to be $\xi_e \in [0.5\xi_{e,bif}, 1.5\xi_{e,bif}]$. Moreover, by taking the ratio of of (3.26) to (3.42) at these ξ_e values, one can quantify

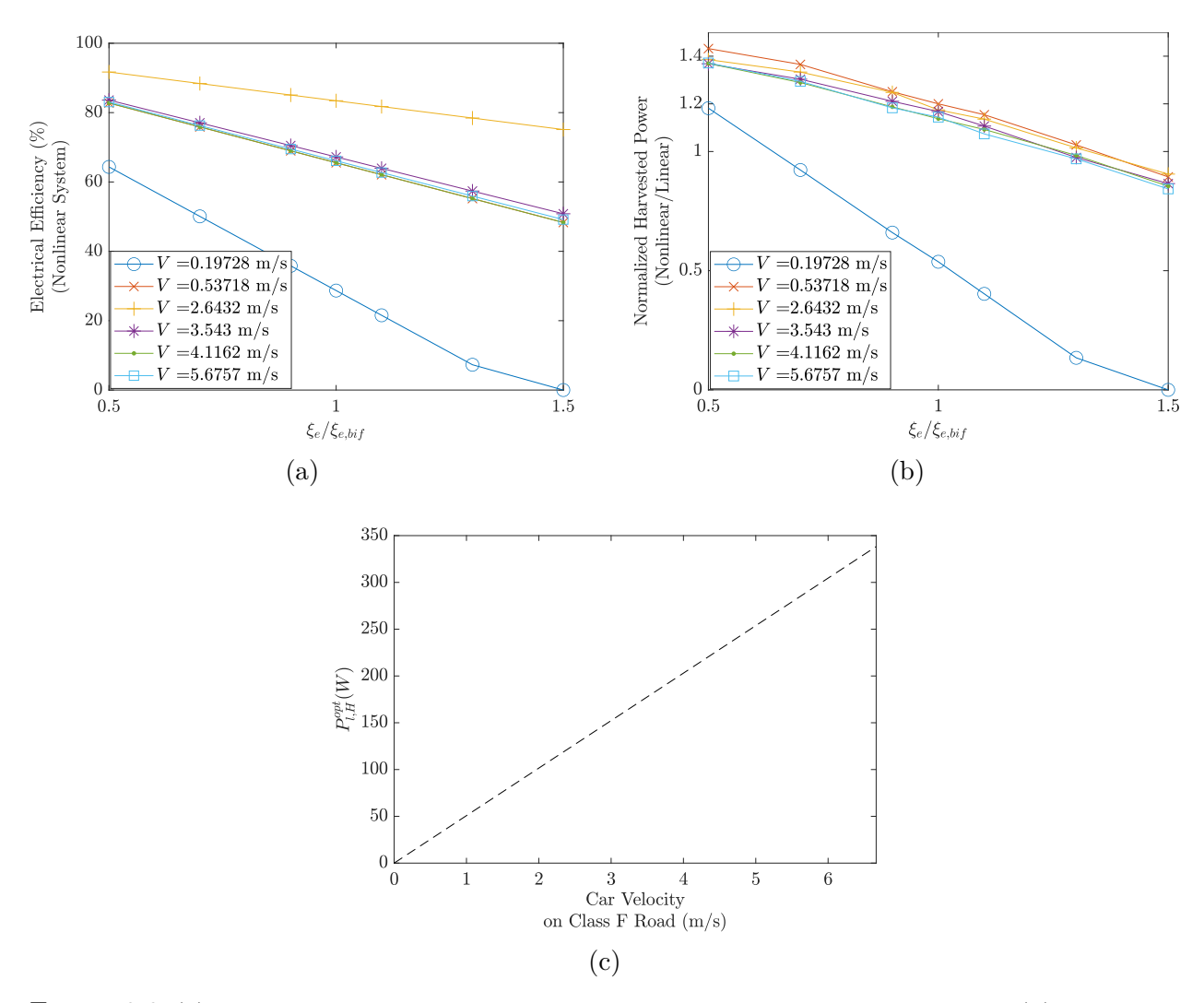


Figure 3.9 (a) Electrical efficiency for the nonlinear system around bifurcation. (b) Nonlinear system mean power harvested, normalized with the optimal linear system. (c) Optimal linear system harvested power.

the normalized expected value of power that flows into the electrical domain relative to the optimized linear benchmark system when the system is near bifurcation. This is plotted vs. $\xi_e/\xi_{e,bif}$ on a class F road for six different speeds in Fig. 3.8b. It is finally apparent that for all driving speeds shown, the energy transferred into the electrical domain is between 130% and 143% of the optimal linear system when electrical damping is chosen to accommodate P-bifurcation. Note that it is also apparent that the power into the electrical domain appears to vary less in magnitude as electrical damping is increased past the predicted bifurcation point. This might signify that an optimal solution is near.

In Fig. 3.8c is the RMS acceleration of the sprung mass plotted using the same parameter values, normalized with respect to the linear system that was optimized for power. A key result here is that the nonlinear system outperforms the linear system and allows for at least 59% better ride comfort for all driving speeds near bifurcation. It is also noted that for most driving speeds, the best ride comfort occurs when ξ_e is near the predicted bifurcation curve. However, the case of V=0.19728 m/s and V=2.6432 m/s seem to break this trend. The former and latter show that the best performance in terms of ride comfort occurs when the system is bimodal and when the system is monomodal with intermittent rotation, respectively. While this means that simultaneous performance objectives cannot be completely met in the case of the V=0.19728 m/s case, it is actually apparent that the power into the electrical domain decreases by at most 2%. In the case of V=2.6432 m/s, simultaneous objectives are met if electrical damping is larger than the bifurcation value.

In Fig. 3.8d, is then the road handling index normalized with respect to the same optimal linear system and for the given parameter set. It is finally interesting to note that the performance in this metric somehow qualitatively mirrors that of the ride comfort which means the road handling performance objective is automatically met if the ride comfort performance objective is met. Quantitatively, as much as 65% improvement in this metric over the linear system is seen near the bifurcation point. Excellent road handling can therefore be expected with the proposed nonlinear EHSA.

To further understand the power potential of the nonlinear EHSA, the electrical efficiency determined via (3.32) is plotted vs. driving speed on a class F road in Fig. 3.9a. The result from (3.29) is then divided by (3.33) and one can show that

$$\frac{P_{nl,H}}{P_{l,H}^{opt}} = \frac{\hat{P}_{nl,H}}{\hat{P}_{l,H}^{opt}} \tag{3.43}$$

The corresponding harvested power is then plotted in Fig. 3.9b. However, first note that the zero values of power and electrical efficiency correspond to when the electrical damping ξ_e is greater than the upper limit $\xi_{e,max}$ that is achieved with only internal resistance; $\xi_{e,max} = \frac{\kappa^2 n_g^2}{2M_s \omega_0 R^2 R_{int}}$. Simply put, no power can be harvested when there is zero load resistance. Using

parameters from Table 5.1 one finds that $\xi_{e,max} = 0.1791$. While energy transfer might be large near bifurcation, the small electrical efficiency corresponding to large electrical damping results in significant decreases in power harvested. This implies that simply choosing a point near P-bifurcation curve will not guarantee the good power harvested; it is also important to choose an extremely efficient generator. In the best case of $\xi_e = 0.5\xi_{e,bif}$, one can expect around a 20% to 40% improvement over the linear system. Given the result in Fig. 3.9c, this correlates with around 12 Watts per shock at a driving speed of 0.19728 m/s and around 412 Watts per shock at a driving speed of 5.6757 m/s.

3.5 Discussion on Findings

In this chapter, analysis was done which pertained to the performance of an IPVA-based EHSA connected to a quarter-car suspension system while varying the dimensionless pendulum length η . The performance of the device was measured relative to a linear benchmark with locked pendulum whereby electrical efficiency was considered and the linear system was thereby optimized for power. Excellent power harvesting, sprung mass acceleration, and road handling of the device was determined to occur for large η when the system PDF was bimodal, prompting the development of a Wiener path integration formulation to determine approximately when the PDF is bimodal. Some PSD analysis showed that for normalized frequencies of $\omega/\omega_0 < 1$ and $\omega/\omega_0 > 3$ the total power was much larger than that of the linear benchmark system. Energy flow analysis also showed that more energy flowed into the electrical domain as the pendulum length was increased.

A variation-based formulation was then adopted which, in addition to the value of the PDF, allowed for a prediction for the estimated sign of the second derivative of the PDF at any point of interest. An efficient bifurcation detection algorithm was thereby developed, which resulted in the prediction of three distinct regions in the noise intensity and electrical damping plane. These regions corresponded to monomodal, bimodal, and finally flat (rotation) probability distributions. The algorithm results were verified with an MCS.

Next, the performance of the EHSA was measured against the optimized linear system

driving on a class F road and varying driving speeds with electrical damping which put the system at or near the bifurcation curve. It was determined that energy transfer into the electrical domain may be as much as 43% larger than that of the optimized linear benchmark system when the nonlinear system is in the neighborhood of P-bifurcation. Furthermore, harvested power can be around 20% improved, while ride comfort and road handling may be improved by at least 59% for all investigated driving speeds. Electrical efficiency was shown to diminish the power harvested from the nonlinear EHSA for high electrical damping while ride comfort and road handling were much less sensitive to electrical damping variation. Therefore, it is first important to select the most efficient generator. In the case that a generator is not very efficient, it is recommended to select electrical damping values less than required for bifurcation when power harvesting is the most important metric considered.

While the bifurcation detection algorithm did not allow for complete optimization in the performance, it serves as a means for choosing initial parameter values to be used in a less exhaustive MCS with a full parameter sweep across the reduced realistic domain of values that will ultimately optimize the system parameters. It should be noted that the proposed algorithm could be used in any case where the qualitative nature of the probability distribution is of interest and there is uniformity in the highest derivatives of the produced Euler-Lagrange equations. Otherwise, other approximate methods such as the Ritz method might be substituted in the algorithm to solve the Lagrangian optimization problem.

CHAPTER 4

AN EXPERIMENTAL STUDY: P-BIFURCATION, ENERGY HARVESTING, AND VIBRATION SUPPRESSION

This chapter focuses on the bimodal IPVA energy harvesting device with an application to a SDOF structure subjected to Gaussian broadband excitation. The objective is to conduct an experimental investigation into P-bifurcation of the device and the correlation with simultaneous energy harvesting and vibration suppression. Notably, this study includes the experimental parameter characterization for a developed prototype to accommodate accurate predictions of energy harvesting potential, vibration suppression, and bifurcation boundaries. Adequate experimental data is used to verify predictive capabilities, confirm the bifurcation phenomenon, and gather information regarding power harvested and vibration suppression.

4.1 The IPVA Device and System Model

In this section, the IPVA device, which was built and designed for experiment, and the corresponding system model are introduced. The model for the system is shown in Fig. 4.1. The system has a suspended mass M_s with a degree of freedom x_s , stiffness k_s , mechanical damping c_m , and an attached IPVA device with planetary gear coupling to a DC generator. The system also has a base motion x_r .

A holonomic constraint is imposed by the ball screw giving $x_s - x_r = R\theta$, where R is the lead value of the screw divided by 2π . Figures 4.1b and 4.1c then show the bottom and top

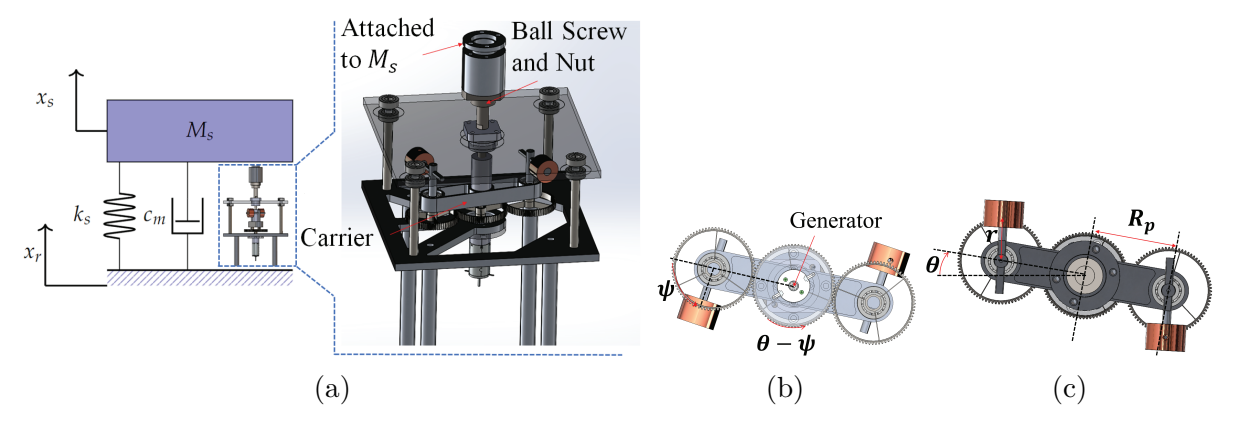


Figure 4.1 (a) Model of the suspended mass system with IPVA device. (b) Bottom view of carrier. (c) Top view of pendulum and gear arrangement with connection to ball screw.

of a carrier that holds two pendulums, each of mass m_p and principal inertia J_p about their centers of mass. Additionally, the center of mass of each pendulum is displaced at a distance r from the respective pivot points which are at a distance R_p from the center of the carrier. These pendulums are free to rotate with an angle ψ relative to the carrier, while the carrier with principal moment of inertia J_c about its vertical axis is free to rotate with an angular degree of freedom θ about the ball screw's vertical axis. Also attached to each pendulum is then a planetary gear of mass m_{gear} and principal moment of inertia J_{pg} . These planetary gears are then meshed with a sun gear connected to the input of a gearbox whose output is connected to the input of a DC generator. The gearbox shaft has a degree of freedom $\psi_g = \theta - \psi$ due to the holonomic constraint imposed by the planetary gear system. The motor rotor then has a degree of freedom $n_g \psi_g$, where n_g is the gear ratio. The principal moment of inertia of the sun gear and generator rotor are J_{sg} and J_r , respectively.

4.1.1 Equations of Motion

To derive the equations of motion using Lagrange's equations, we first derive the kinetic energy, potential energy, and virtual work associated with the system. The kinetic energy for the system can be broken down into energy associated with each component. The energy associated with the suspended mass and carrier is

$$T_1 = \frac{1}{2}M_s(R\dot{\theta} + \dot{x_r})^2 + \frac{1}{2}J_c\dot{\theta}^2$$

Then the energy associated with the pendulums and planetary gears is

$$T_{2} = \frac{1}{2} \left[\left(\sum_{i=1}^{2} (m_{p}r^{2} + J_{p}) + \sum_{i=1}^{2} J_{pg} \right) (\dot{\psi} + \dot{\theta})^{2} \right]$$

$$+ \sum_{i=1}^{2} m_{p} \left(R_{p}^{2} \dot{\theta}^{2} + 2R_{p}r \cos(\psi) \dot{\theta} (\dot{\theta} + \dot{\psi}) \right)$$

$$+ \sum_{i=1}^{2} (m_{gear} R_{p}^{2}) \dot{\theta}^{2}$$

The energy associated with sun gear and generator rotor is given by

$$T_3 = 1/2 \left(J_r n_g^2 + J_{sg} \right) \left(\dot{\theta} - \dot{\psi} \right)^2 \tag{4.1}$$

Finally, the total kinetic energy is given by

$$T = T_{1} + T_{2} + T_{3}$$

$$= \frac{1}{2} \left[\left(\sum_{i=1}^{2} \left(m_{gear} R_{p}^{2} \right) + J_{c} \right) \dot{\theta}^{2} \right]$$

$$+ \left(\sum_{i=1}^{2} \left(m_{p} r^{2} + J_{p} \right) + \sum_{i=1}^{2} J_{pg} \right) \left(\dot{\psi} + \dot{\theta} \right)^{2}$$

$$+ \sum_{i=1}^{2} m_{p} \left(R_{p}^{2} \dot{\theta}^{2} + 2 R_{p} r \cos(\psi) \dot{\theta} \left(\dot{\theta} + \dot{\psi} \right) \right)$$

$$+ \left(J_{r} n_{g}^{2} + J_{sg} \right) \left(\dot{\theta} - \dot{\psi} \right)^{2} + \frac{1}{2} M_{s} (R \dot{\theta} + \dot{x}_{r})^{2}$$

$$(4.2)$$

where $(\dot{\cdot}) = d(\cdot)/dt$ represents the first time derivative. The potential energy is given by

$$V = \frac{1}{2}k_s \left(R\theta\right)^2 \tag{4.3}$$

Furthermore, a torsional viscous damping coefficient c_p is introduced to account for energy loss at the pivot point of the pendulum due to bearings. Assuming negligible internal inductance such as in [51, 62, 86], one can also assume a generator electrical damping torque opposing the flow of current due to Faraday's law and proportional to the generator rotor velocity with coefficient c_e . Specifically, define the electrical damping imposed by the generator as

$$c_e = \frac{n_g^2 \kappa_t^2}{R_i + R_I} \tag{4.4}$$

where R_i and R_l are the internal and load electrical resistance, respectively. κ_t is the torque constant of the generator. Additionally, mechanical losses in the direction opposing the sun gear and generator rotor motion ψ_g can be approximated with a viscous damping torque with coefficient c_{gm} and coulomb friction torque in the same direction. This accounts for mechanical energy dissipation within the generator housing as well as dissipation in the gears. Finally, note that the virtual displacement of the mass M_s is given by $\delta x_s = R\delta\theta$, the virtual displacement of the pendulum in the direction of the pendulum damping torque is $\delta\psi$ and the virtual displacement of the sun gear is $\delta\psi_g = \delta\left(\theta - \psi\right)$. It follows that the summed

virtual work due to the mechanical damping, electrical damping, and frictional torque is written as

$$\delta Q = -c_m R^2 \dot{\theta} \delta \theta - (c_e + c_{gm}) \left(\dot{\theta} - \dot{\psi} \right) \delta \left(\theta - \psi \right) - c_p \dot{\psi} \delta \psi$$

$$- T_f \frac{\left(\dot{\theta} - \dot{\psi} \right)}{\left| \left(\dot{\theta} - \dot{\psi} \right) \right|} \delta \left(\theta - \psi \right)$$
(4.5)

where $-T_f \frac{(\dot{\theta} - \dot{\psi})}{|(\dot{\theta} - \dot{\psi})|} \delta(\theta - \psi)$ accounts for the friction - based losses in generator rotor and gear motion. With (4.2), (4.3) and (4.5), the equations of motion for the system were derived using Lagrangian methodology and are given here.

$$\left(MR^{2} + J_{c} + J_{r}n_{g}^{2} + J_{sg} + \sum_{i=1}^{2} m_{p}R_{p}^{2} + \sum_{i=1}^{2} J_{p} + \sum_{i=1}^{2} m_{p}r^{2}\right) \ddot{\theta}
+ \left(\sum_{i=1}^{2} m_{gear}R_{p}^{2} + \sum_{i=1}^{2} J_{pg} + 2\sum_{i=1}^{2} m_{p}R_{p}r\cos(\psi)\right) \ddot{\theta}
+ \left(\sum_{i=1}^{2} m_{p}r^{2} + \sum_{i=1}^{2} m_{p}R_{p}r\cos(\psi) + \sum_{i=1}^{2} J_{p} + \sum_{i=1}^{2} J_{pg} - J_{r}n_{g}^{2} - J_{sg}\right) \ddot{\psi}
+ \left(c_{e} + c_{gm} + c_{m}R^{2}\right) \dot{\theta} - \left(c_{e} + c_{gm}\right) \dot{\psi} + kR^{2}\theta
- 2\sum_{i=1}^{2} m_{p}R_{p}r\dot{\psi}\dot{\theta}\sin(\psi) - \sum_{i=1}^{2} m_{p}R_{p}r\sin(\psi) \dot{\psi}^{2}
= -M\ddot{x}_{r}R - T_{f} \frac{\left(\dot{\theta} - \dot{\psi}\right)}{\left|\left(\dot{\theta} - \dot{\psi}\right)\right|},
\left(\sum_{i=1}^{2} m_{p}r^{2} + \sum_{i=1}^{2} J_{p} + \sum_{i=1}^{2} J_{pg} + J_{r}n_{g}^{2} + J_{sg}\right) \ddot{\psi}
+ \left(\sum_{i=1}^{2} J_{p} + \sum_{i=1}^{2} J_{pg} + \sum_{i=1}^{2} m_{p}\left(r^{2} + R_{p}r\cos(\psi)\right) - J_{r}n_{g}^{2} - J_{sg}\right) \ddot{\theta}
+ \sum_{i=1}^{2} m_{p}R_{p}r\sin(\psi) \dot{\theta}^{2}
+ \left(c_{e} + c_{p} + c_{gm}\right) \dot{\psi} - \left(c_{e} + c_{gm}\right) \dot{\theta} = T_{f} \frac{\left(\dot{\theta} - \dot{\psi}\right)}{\left|\left(\dot{\theta} - \dot{\psi}\right)\right|}$$
(4.6)

In (4.6), $\ddot{(\cdot)} = d^2(\cdot)/dt^2$ represent the second time derivative. Let us next define \hat{M} as

the effective structural mass constituted by components only multiplying $\ddot{\theta}$. Then,

$$\sum_{i=1}^{2} m_{gear} R_p^2 + MR^2 + J_c$$

$$= \left(2m_{gear} R_p^2 / R^2 + M + \frac{J_c}{R^2}\right) R^2 = \hat{M}R^2$$
(4.7)

where it should be noted that here $2m_{gear}$ constitutes the mass of planet gears, vertical shafts and bearings at the pendulum pivot point combined. Thus, these moment of inertia terms can be absorbed into the effective mass term without loss of generality. In order to simplify parameter identification, the effects of friction torque and viscous damping torque are combined and approximated by a single viscous damping torque in the direction opposing the generator motion and with coefficient c_f . Additional terms can be combined and the following set of dimensionless parameters are defined.

$$\mu_{r} = \frac{2m_{p}R_{p}^{2}}{M_{s}R^{2}}, \ \mu_{p} = \frac{2(J_{p} + J_{pg})}{M_{s}R^{2}}, \ \eta = \frac{r}{R_{p}},$$

$$\mu_{g} = \frac{n_{g}^{2}J_{r} + J_{sg}}{M_{s}R^{2}}, \ \alpha = \frac{\dot{M}}{M_{s}}, \ \omega_{0} = \sqrt{\frac{k_{s}}{M_{s}}}, \ \xi = \frac{c_{m}}{2M_{s}\omega_{0}},$$

$$\xi_{e} = \frac{c_{e}}{2M_{s}R^{2}\omega_{0}}, \ \xi_{f} = \frac{c_{f}}{2M_{s}R^{2}\omega_{0}}, \ \xi_{p} = \frac{c_{p}}{2M_{s}R^{2}\omega_{0}}$$

$$\tau = \omega_{0}t, \ (\bullet)' = \omega_{0}(\dot{\bullet}), \ (\bullet)'' = \omega_{0}^{2}(\dot{\bullet})$$

$$(4.8)$$

The equations of motion for the system are now rewritten in terms of the dimensionless parameters as follows:

$$\mathbf{M}(\psi)\mathbf{x}'' + \mathbf{C}\mathbf{x}' + \mathbf{K}\mathbf{x} + \mathbf{g}(\mathbf{x}, \mathbf{x}') = \mathbf{f}$$
(4.9)

where

$$\mathbf{M}(\psi) = \begin{bmatrix} M_{11} & M_{12} \\ M_{12} & M_{22} \end{bmatrix},$$

$$M_{11} = 1 + \alpha + \mu_p + \mu_g + \mu_r \left(1 + \eta^2 + 2\eta \cos(\psi) \right)$$

$$M_{12} = \mu_r \eta (\eta + \cos(\psi)) - \mu_g + \mu_p$$

$$M_{22} = \mu_r \eta^2 + \mu_g + \mu_p$$

$$\mathbf{C} = \begin{bmatrix} 2(\xi + \xi_e + \xi_f) & -2(\xi_e + \xi_f) \\ -2(\xi_e + \xi_f) & 2(\xi_e + \xi_f + \xi_p) \end{bmatrix},$$

$$\mathbf{K} = \begin{bmatrix} 1 & 0 \\ 0 & 0 \end{bmatrix}, \mathbf{f} = \begin{pmatrix} W(\tau) \\ 0 \end{pmatrix},$$

$$\mathbf{g}(\mathbf{x}, \mathbf{x}') = \mu_r \eta \begin{pmatrix} -(2\psi'\theta' + \psi'^2)\sin(\psi) \\ \theta'^2\sin(\psi) \end{pmatrix}$$

$$(4.10)$$

In (4.9) and (4.10), $\mathbf{x} = (\theta, \psi)^T$, \mathbf{M} is the dimensionless inertia matrix, \mathbf{C} is the dimensionless damping matrix, \mathbf{K} is the dimensionless stiffness matrix, and the vector \mathbf{f} is associated with stochastic excitation. The excitation term $W(\tau) = -\ddot{x}_r M/MR \ \omega_0^2$ is then defined to be the normalized Gaussian white noise with zero mean and constant two-sided power spectral density D, given that $D = d/(\ \omega_0^3 R^2)$ where d is the physical noise intensity in units of squared acceleration per frequency. ξ and ξ_p are the damping ratios associated with the structure and the pendulum, respectively. α quantifies added mass due to inertance, while μ_r and μ_p quantify pendulum mass and moment of inertia relative to structural mass. η quantifies the length of the pendulum. Furthermore, \mathbf{g} represents the nonlinear Coriolis, centrifugal terms, and friction. It is finally apparent that μ_r and η are the quantifiers of non-linearity in the system. Additionally, note that the equations of motion are written in terms of the normalized time variable, $\tau = \omega_0 t$, where ω_0 is the characteristic frequency associated with the suspended mass and spring stiffness.

4.2 The Experimental Setup and Characterization

The experimental setup correlating with Fig. 4.1 is now shown in Fig. 4.2. The setup consists of the IPVA, a generator, a mass suspended with eight coil springs and clamps, a signal conditioner, an electrodynamic shaker, an amplifier, a vibration controller, and a pendulum tracking system. In this section, the measured or experimentally determined values for all parameters outlined in the previous section are given.

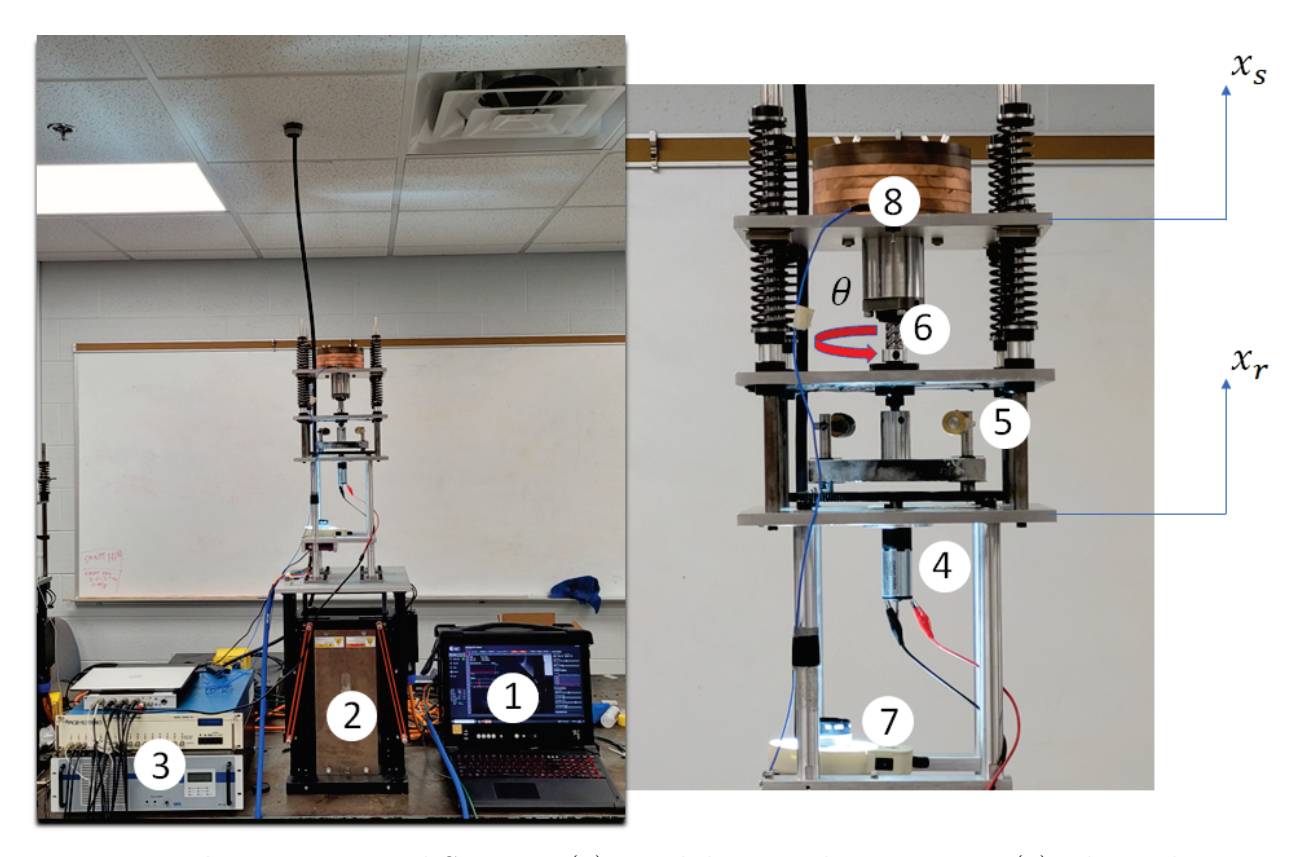


Figure 4.2 The Experimental System. (1) Pendulum tracking system. (2) Electrodynamic shaker. (3) Amplifier, signal conditioner, and vibration controller. (4) DC generator. (5) Pendulums on the carrier. (6) Ball screw and nut with the coupler to suspended mass. (7) Camera and light for pendulum tracking. (8) Suspended mass.

4.2.1 Fitting the Frequency Response Function

Mechanical damping ξ , characteristic frequency ω_0 , and rotational inertia of ball screw and carrier were fit in the frequency domain by fitting the norm squared frequency response function (FRF) of the relative acceleration $(\ddot{x}_s - \ddot{x}_r)$ for the linear system with pendulums and gears removed. For a constant acceleration base excitation experiment steady-state response, $\ddot{x}_r = A \cdot \exp j \ \omega t$, $x_s = X_s (j \ \omega) \cdot \exp j \ \omega t$ and $x_s - x_r = R\Theta (j \ \omega) \cdot \exp j \ \omega t$. Then the norm squared FRF takes the form given here.

$$\frac{(R|\Theta|)^2 \omega^4}{A^2} = \frac{r^4}{(1 - r^2 (1 + \alpha_l)^2)^2 + 4\xi^2 r^2}$$
(4.11)

where $r = \frac{\omega}{\omega_0}$ and $\alpha_l = \alpha - 2m_{gear}R_p^2/M_sR^2$. A sine sweep test with 0.15g base acceleration (g is the acceleration due to gravity) was done and the values of ω_0 , ξ , and α were fit using a nonlinear least squares algorithm in MATLAB. The close agreement between the theoretical

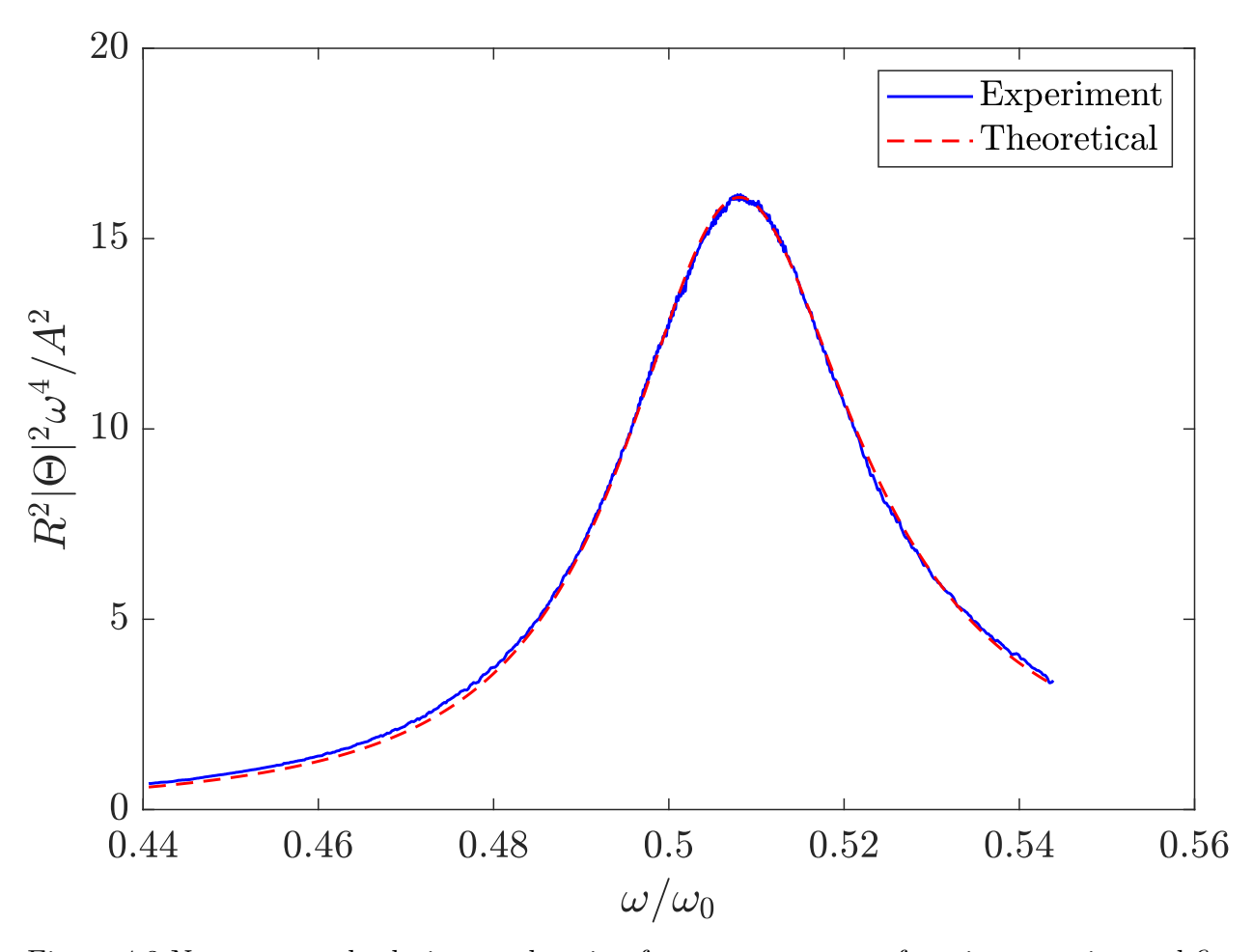


Figure 4.3 Norm squared relative acceleration frequency response function experimental fit. and experimental FRF is shown in Fig. 4.3.

4.2.2 The Experimental Methods

With the experimental setup shown in Fig. 4.2, a three-hour random excitation experiment was done for the case of four different load resistances attached to the generator, giving four different electric damping (ξ_e) values with the use of (4.4) and (4.8). This is outlined in Table. 4.1. The resistor values were chosen to incorporate a sufficiently large electrical damping range while using resistors that were imediately available. Note that open circuit implies infinite load resistance. Also, note that a total of thirty minutes of data was removed in order to eliminate transient beginning and ending dynamics which might have a misleading effect when interpreting some statistical information. The total duration of the analyzed data in each case was then about two and a half hours. The excitation used in the

| Load Resistance (R_l) | Electric Damping (ξ_e) |
|-------------------------|----------------------------|
| Open Circuit | 0 |
| 10Ω | .02 |
| 3.9Ω | 0.037 |
| 1 Ω | 0.0637 |

Table 4.1 Electric load resistances and associated electrical damping value.

experiment was such that the base acceleration had a root mean square (RMS) value of 0.8g where g is the acceleration due to gravity and the corresponding PSD is shown in Fig. 4.4. Note that this PSD was constructed to be broadband on the frequency band between two and thirteen cycles per second while also including the resonant frequency determined in the FRF fit and also within the voltage, current, and stroke limits of the electrodynamic shaker. Shaker current, voltage, and minimum frequency limitations are directly proportional to the acceleration, velocity, and displacement output limitations, respectively.

For the purpose of verifying bifurcation predictions, the same experiments were also done for the case of 0.6g RMS base acceleration as well as a 0.8g RMS base acceleration case with a shorted circuit (zero load resistance). The corresponding PDFs will be analyzed and it shall be determined whether the bifurcation boundaries can be used to predict their qualitative nature.

4.2.3 Characterization of Experiment

Various fitted, measured, and generator parameters used in this study are presented in Table 4.2 and Table 4.3. It should be noted that μ_r was directly measured, while μ_p and η were computed using SolidWorks. Additionally, c_e varies with load resistance as described by (4.4), but once a load resistance is selected, it is calculated using the reported values for the $Maxon\ 110207\ 4.5$ Watt DC motor with a gear ratio of $n_g=5.2$. Finally, although mechanical damping ξ was determined through the FRF fit, it was observed that it significantly differs from the value obtained in the actual experiment described in Sec. 4.2.2; hence, it is discarded hereinafter. The value is included in Table E.1 of Appendix E. It should finally be noted that stiffness k_s and mass M_s in ω_0 were chosen to keep the linear resonant frequency low and

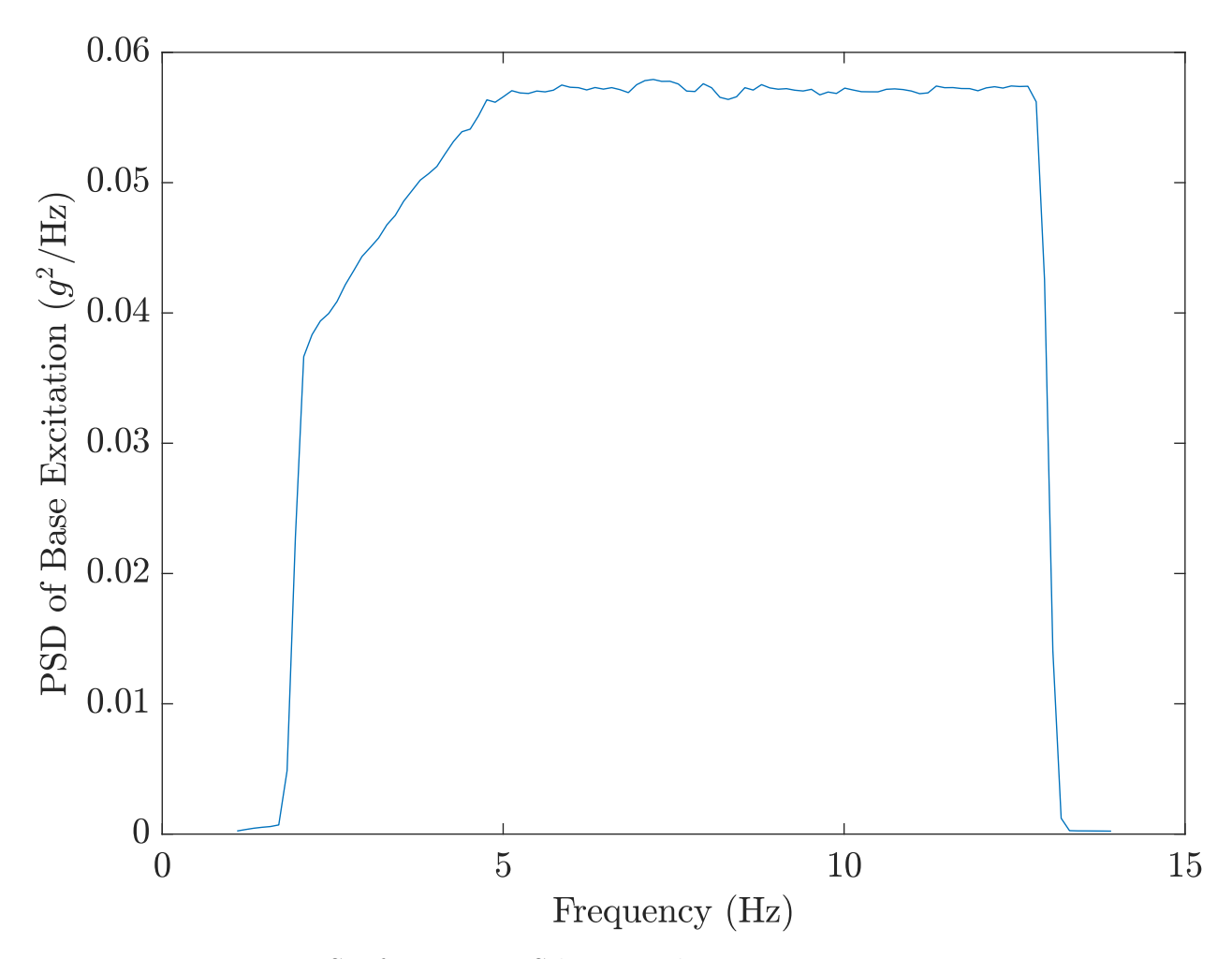


Figure 4.4 PSD for 0.8g RMS base acceleration excitation experiment.

accommodate a lower excitation frequency upper bound while also keeping the mechanical damping ratio ξ_m as low as possible with the springs and mass which were available on hand. Pendulum parameters μ_r and η were chosen after numerical simulation predicted that they were sufficiently large to accommodate the bimodal phenomenon of interest while also remaining relatively compact. The choice of generator torque constant κ_t , internal resistance R_i , and gear ratio n_g was governed by a combination of what was commercially available and the intent to limit generator inertia μ_g , limit internal resistance, and use a gear ratio which would put the generator speed near its nominal rated value in the documentation.

| Dimensionless Parameters | Value |
|--------------------------|-------|
| μ_r | 2.43 |
| η | 0.45 |
| μ_p | 0.38 |
| μ_g | 0.28 |
| α | 5.93 |

Table 4.2 Dimensionless Parameters of Experimental IPVA system.

| Physical Parameters | Value |
|---------------------|------------------------|
| κ_t | $0.0168~\mathrm{Nm/A}$ |
| R_i | 3.17Ω |
| ω_0 | $12.26~\mathrm{Hz}$ |
| M_s | $9.39~\mathrm{kg}$ |
| R | $\frac{.03}{2\pi}$ m |

Table 4.3 Physical Parameters of Experimental IPVA system.

4.2.3.1 Parameter Fitting with Frequency Domain Optimization

To further accommodate complicated dynamics not modeled in (4.9) and (4.10) which may only be noticeable in the experiment with random excitation, $\Xi = (\xi_f, \xi_p, \xi)^T$ has been left as a vector of variables to be tuned in an optimization routine. The new approximate model is then a function of unknown linear damping coefficients Ξ . Also, in this case, $W(\tau)$ in (4.10) is the dimensionless form of the exact excitation input to the shaker which was also used to generate Fig. 4.4. The optimization routine is now defined for the determination of the most suitable Ξ that forces the RMS velocities for the ball screw, pendulum, and generator obtained from the simulation of the EOM and from the experiment outlined in Sec. 4.2.2 to be within three percent agreement. To accurately capture pendulum dynamics, especially when there is rotation, the objective function is chosen to minimize the error in the mean square pendulum velocity on the frequency band below two cycles per second. The

optimization problem is formally defined as

$$\min_{\Xi} \left| 1 - \sum_{0 \le f_k < 2} \frac{\left| V_{\psi_{exp}}(f_k) \right|^2}{\left| V_{\psi_{sim}}(f_k) \right|^2} \right|$$

subject to

$$\max_{i=1,2,3} |F_i| < 0.03 \tag{4.12}$$

$$(0,0,0)^T \le \Xi \le (0.01,0.03,0.15)^T$$
,

 $\mathbf{x}(0) = \mathbf{x}_{0,exp}, \quad \mathbf{x}'(0) = \mathbf{v}_{0,exp},$

$$\mathbf{M}(\psi)\mathbf{x}'' + \mathbf{C}(\xi_e, \mathbf{\Xi})\mathbf{x}' + \mathbf{K}\mathbf{x} + \mathbf{g}(\mathbf{x}, \mathbf{x}') - \mathbf{f} = 0,$$

where

$$\mathbf{F} = \left(1 - \frac{\text{RMS}(\theta'_{exp})}{\text{RMS}(\theta'_{sim})}, 1 - \frac{\text{RMS}(\psi'_{exp})}{\text{RMS}(\psi'_{sim})}, 1 - \frac{\text{RMS}(\psi'_{g,exp})}{\text{RMS}(\psi'_{g,sim})}\right).$$

where RMS(·) is defined as the RMS value of (·). The symbols (·)_{exp} and (·)_{sim} represent the experimental and simulated values of (·), respectively. Additionally, $\mathbf{x}_{0,exp}$ and $\mathbf{v}_{0,exp}$ are the initial position and velocity in the experiment, respectively. It is also important to note that the time period used for both the simulation and experimental data in the optimization process was the same. Furthermore, $V_{\psi}(f_k) = \sum_{n=0}^{N-1} \dot{\psi}(n) \exp\left(-i2\pi \frac{f_k}{f_s}n\right)$ denotes the discrete Fourier transform of the pendulum velocity, where n is the sample number, $f_k = kf_s/N$ is the chosen frequency in cycles per second, f_s is the sampling rate and N is the total number of samples. The objective function is then the absolute value of the error in the mean spectral power of the pendulum velocity below two cycles per second. The upper limit of two cycles per second was chosen to account for the pendulum dynamics associated with frequencies below the lowest excitation frequency, including the rotational component at zero cycles per second. This should help fit more closely potential rotational dynamics as well as possible subharmonic features in the response.

To execute the optimization described in (4.12), an initial three-dimensional grid of finite parameter values was established. Initial fitting in the time domain detailed in Appendix E helped narrow down the parameter space to the range specified in (4.12). Next, parallel computing leveraging high-performance computing resources with 4×128 CPU cores and

921.6 gigabytes of memory per 128 cores to solve the EOM in (4.12) with ode45 in MAT-LAB. Consequentially, the objective function value was determined. The minimal objective function that satisfied the constraint was then determined and the optimized damping parameters for all resistant loads along with the corresponding maximum RMS velocity percent errors are presented in Table 4.4. It should be noted that each resistance load case was associated with a unique optimal Ξ . Throughout the rest of this study, Ξ is considered as a function of ξ_e (dependent on load resistance). This approach is necessary because the model described in (4.12) does not fully capture the complex dynamics involved. For instance, intricate dynamics associated with ball screw damping, discussed in [93, 94], are omitted.

Following the optimization routine of (4.12), a comparison between experimental and simulated PSDs is displayed in Fig. 4.5. Note that the maximum RMS velocity error is below 3% across all PSDs and the low frequency contributions are accurate qualitatively, while the peak PSD values do not align as closely. It was proven difficult to obtain complete agreement. While this is deemed acceptable given the primary focus on the RMS error in this research, it highlights some flaws in the mathematical model.

In concluding this section, it is noted that all RMS velocities and power, with power being directly related to the square of the generator velocity as shown in previous chapters and in [62], were within a 3% error margin. Consequently, it is anticipated that predictions regarding vibration suppression (reduction in relative velocity of M_s) and energy harvesting will have a maximum of 3% error, at least when electrical damping and noise intensity are relatively close to the experimental values in magnitude. Additionally, it is important to highlight that the optimization that initially only minimized RMS velocity error resulted in RMS error as low as 0.62%. However, predictions related to the rotational dynamics were poor. Hence, this work uses the objective function in (4.12) for enhanced accuracy in predicting complicated dynamics and improving the likelihood of forecasting P-bifurcation in the following section.

| Load Resistance (R_l) | $\mathbf{\Xi}^T = (\xi_f, \xi_p, \xi)$ | Maximum RMS Velocity Error |
|-------------------------|--|----------------------------------|
| Open Circuit | (0.005, 0.004, 0.0821) | 2.84% |
| 10Ω | (0, 0, 0.1093) | 2.10% |
| $3.9~\Omega$ | (0, 0, 0.1093) | 1.37% |
| 1 Ω | (0.0025, 0, 0.1093) | 2.74% |

Table 4.4 Fitted damping values for all load resistance cases and corresponding maximum % RMS velocity error.

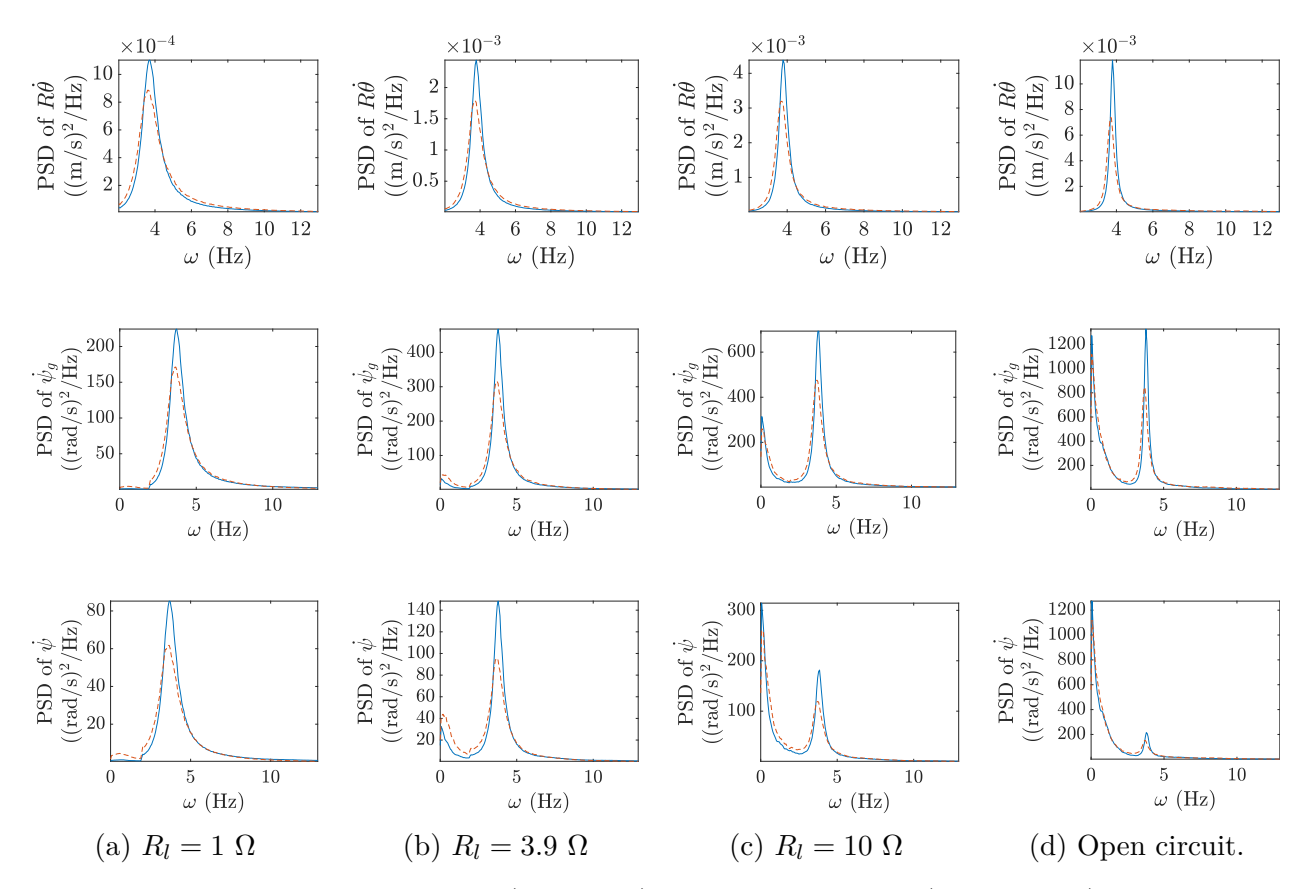


Figure 4.5 Fitted simulation PSD (solid line). Experiment PSD (dashed line). Each figure column corresponds to a different load resistor case.

4.3 Verification of P-bifurcation with Power Harvested and Vibration Suppression Exploration

The bifurcation tracking formulated in Chapter 2 will now be used to predict the critical values in a two-parameter plane for which a P-bifurcation, or change between the total number of PDF maxima, may occur. In this section, the stochastic bifurcation analysis is briefly reintroduced and the prediction is compared with experimental results.

4.3.1 Moment Equations And P-bifurcation

Just as in Chapter 2, but choosing this time to use symbolic matrix notation rather than summation notation [14], the equations governing the steady state solution to moments of all orders are

$$\left\langle \left(\nabla g_m\right)^T \hat{\mathbf{a}} + \frac{1}{2} \operatorname{tr} \left(\hat{\mathbf{\Sigma}} \hat{\mathbf{\Sigma}}^T \nabla \left(\nabla g_m\right)^T\right) \right\rangle = 0 \tag{4.13}$$

where $\langle \cdot \rangle$ is the expectation operator, $g_m = \hat{y}_1^i \hat{y}_2^j \hat{y}_3^k \hat{y}_4^l$ is a polynomial consisting of the state variables in $\hat{\mathbf{y}} = (\theta, \phi, \theta', \phi')^T$ up to a desired order n = i + j + k + l, $\nabla = \frac{\partial}{\partial \hat{\mathbf{y}}}$, and $\operatorname{tr}(\cdot)$ represents the trace of the matrix (\cdot) . Note that ϕ is the pendulum angle of oscillation relative to some fixed angle ϕ_0 . $\hat{\mathbf{a}}$ and $\hat{\mathbf{\Sigma}}$ are the deterministic and stochastic contributions, respectively. Specifically, they are defined by first writing the stochastic differential form [15] of (4.12) as follows.

$$d\mathbf{y} = \mathbf{a}(\mathbf{y}) d\tau + \mathbf{\Sigma}(\mathbf{y}, \tau) dB \tag{4.14}$$

where $\mathbf{y} = (\theta, \psi, \theta', \psi')^T$ and

$$\mathbf{a}(\mathbf{y}) = -\begin{bmatrix} \mathbf{0}_{2\times2} & \mathbf{I}_{2\times2} \\ \mathbf{M}^{-1}\mathbf{K} & \mathbf{M}^{-1}\mathbf{C} \end{bmatrix} \mathbf{y} - \begin{pmatrix} \mathbf{0}_{2\times1} \\ \mathbf{M}^{-1}\mathbf{g}(\mathbf{y}) \end{pmatrix}$$

$$\mathbf{\Sigma}(\mathbf{y},\tau) = \begin{bmatrix} \mathbf{0}_{2\times2} \\ \mathbf{M}^{-1} \end{bmatrix} \begin{pmatrix} \sqrt{D} \\ 0 \end{pmatrix}$$
(4.15)

and in this case dB is a scalar differential Wiener process, with $\langle dB(\tau)dB^{T}(\tau)\rangle = Dd\tau$. Just as in Chapter 2, the drift and diffusion vectors are now first-order Taylor expanded about some pendulum angle ϕ_0 to obtain

$$\hat{\mathbf{a}}(\hat{\mathbf{y}}, \phi_0) = \left[\mathbf{a}(\mathbf{y}) + \left(\frac{\partial \mathbf{a}(\mathbf{y})}{\partial \psi}\right) \phi\right]_{\psi = \phi_0}$$

$$\hat{\mathbf{\Sigma}}(\hat{\mathbf{y}}, \phi_0, \tau) = \left[\mathbf{\Sigma}(\mathbf{y}, \tau) + \left(\frac{\partial \mathbf{\Sigma}(\mathbf{y}, \tau)}{\partial \psi}\right) \phi\right]_{\psi = \phi_0}$$
(4.16)

To alleviate the infinite hierarchy of dependence of moments on higher order moments, as detailed in Chapter 2 with reference to [14, 15], n is set equal to two, and Gaussian closure

is used. Next, the Jacobian of the moment equations in (4.13) with respect to moment variables and ϕ_0 , is evaluated at $\phi_0 = 0$ and the parameter values required for a vanishing Jacobian determinant are determined. Then with the algorithm developed in Chapter 2 all P-bifurcation solution candidates are readily found.

4.3.1.1 P-bifurcation Verification with Experiment

With the constructed excitation PSD shown in Fig. 4.4, the experiment excitation is only an approximation to the theoretically assumed Gaussian white noise. Given the theoretical dimensionless noise $D = d/(\omega_0^3 R^2)$, d was chosen so that the integral of the PSD of the white noise on the frequency band from $f_1 = 2$ Hz to $f_2 = 13$ Hz was equal to the mean square experiment acceleration value of $(0.8g)^2/2$. The division by two is necessary to keep total power conserved since one must integrate over the negative frequencies as well in the case of a symmetric two-sided spectral density such as with the theoretical Gaussian white noise. Finally, to obtain d, with Parseval's theorem one finds

$$\int_{f_1}^{f_2} d \cdot df = (f_2 - f_1)d = \frac{(0.8g)^2}{2}$$

$$d = \frac{(0.8g)^2}{2(f_2 - f_1)}$$
(4.17)

The dimensionless value is then D = 0.2687.

Using the noise intensity, ξ_e , $\Xi(\xi_e)$ from Table 4.4, and the bifurcation tracking algorithm in Chapter 2, a bifurcation diagram was generated for each resistor case in Table 4.1 with the RMS acceleration excitation of 0.8g. The maximum and minimum boundary for a given electrical damping was then determined and the resultant boundary region is shown in Fig. 4.6. In this figure are also markers indicating the experimental damping and noise intensity values, including the values corresponding to the experiments only used to test the boundary accuracy. It is assumed that the region between the curves in Fig. 4.6 serves as an estimate for where p-bifurcation can occur. In other words, an electrical damping-noise intensity pair outside of this region is assumed to be not correlated with a bifurcation point.

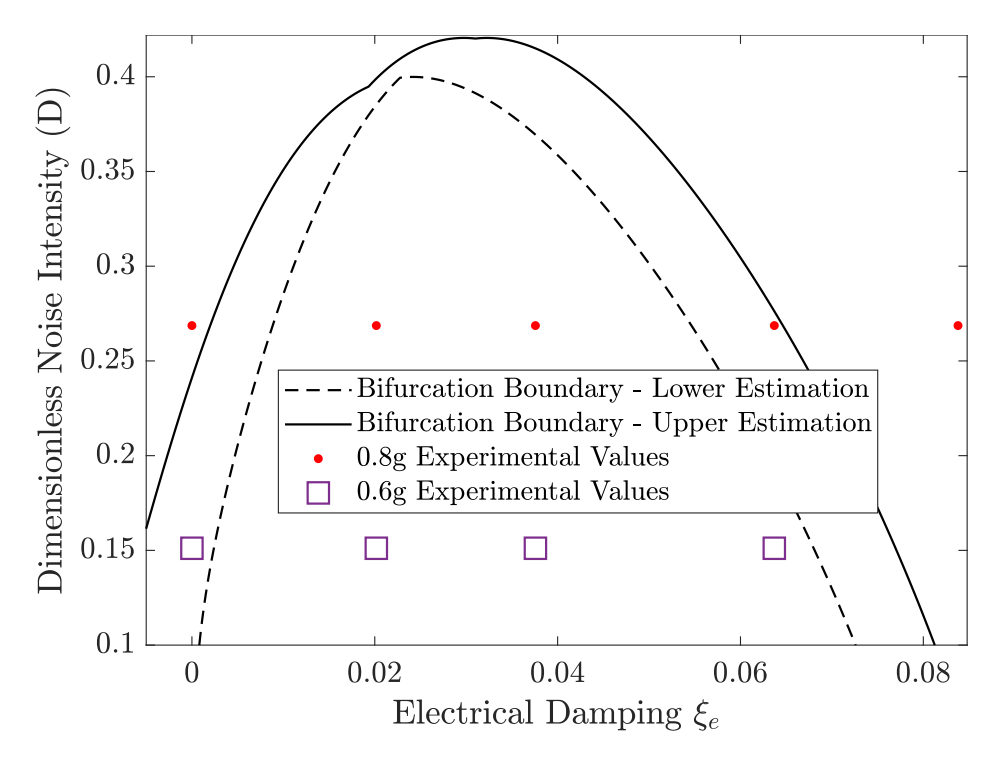


Figure 4.6 Lower and upper bifurcation estimation in the $D - \xi_e$ plane. Point markers and square markers indicate the 0.8g RMS excitation and 0.6g RMS excitation experiment values, respectively. The right-most 0.8g marker corresponds to $R_l = 0$.

The marginal PDFs for the pendulum angle corresponding to each experimental parameter set were also obtained via a Monte Carlo simulation with $\sim 4 \cdot 10^4$ realizations, a dimensionless simulation time of 10^4 and a time step of 10^{-3} . Note that this simulation time corresponds to only ~ 130 seconds in physical time which is drastically smaller than the experimental time of two and a half hours. As a result, any dynamics that develop on a timescale larger than 130 seconds might not be accurately captured. However, given the number of realizations needed to reach stationarity, running the MCS with a simulation time of two and a half hours is impractical within a reasonable timeframe. With this disclaimer aside, the resultant marginal PDFs are shown in Fig. 4.7 and the corresponding Marginal PDFs from the experiment are shown in Fig. 4.8. Note that the pendulum will undergo oscillations centered around $\psi = 2\pi k$ radians for any integer k with possible intermittent rotations in between. As such, the pendulum angle ψ has been replaced in the PDFs with ψ mod 2π and further restricted to the domain of $[-\pi, \pi]$ which is all accomplished using

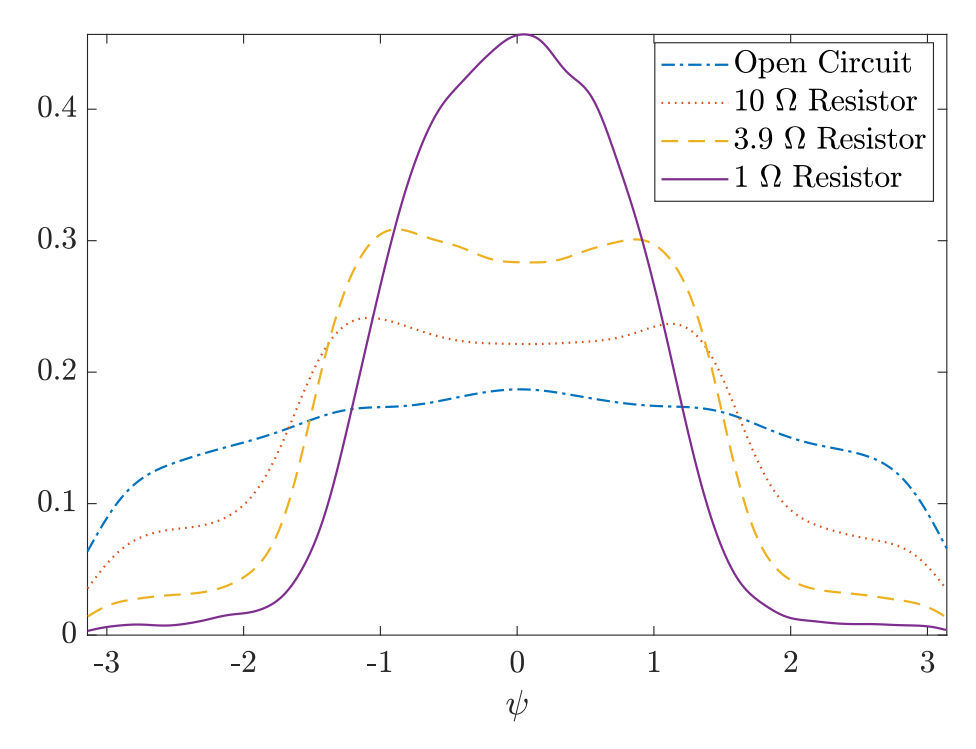


Figure 4.7 Marginal probability density functions for the pendulum angle from simulation using experiment parameters and 0.8g RMS excitation. Each PDF correlates with a point marker in Fig. 4.6.

the 'wrapToPi' function in MATLAB. This does have the side effect of the separation of the PDFs from the ψ axis near $\psi = \pm \pi$ when rotation exists.

Initially, it is important to recognize that the bifurcation diagram in Fig. 4.6 delineates both a right and left boundary region. Considering the relationship between damping and resistance in Table 4.1, transitioning from a 3.9 Ω to a 1 Ω load resistor necessitates entering the right bifurcation boundary region from the left and ending near the outer edge. With that being said, the original bifurcation boundary generated with the parameters from the 1 Ω load resistor case actually had an outer edge that was to the left of the experimental data point. In this case, it is assumed that bifurcation has in fact occurred. Notably, the PDF in Fig. 4.7 associated with the 1 Ω case has negative curvature at its origin and is distinctly monomodal, while the PDF for the 3.9 Ω case on the left side of the boundary region shows positive curvature at the origin and is distinctly bimodal. The experimental PDFs in Fig. 4.8 exhibit similar characteristics in terms of curvature at the origin, with more

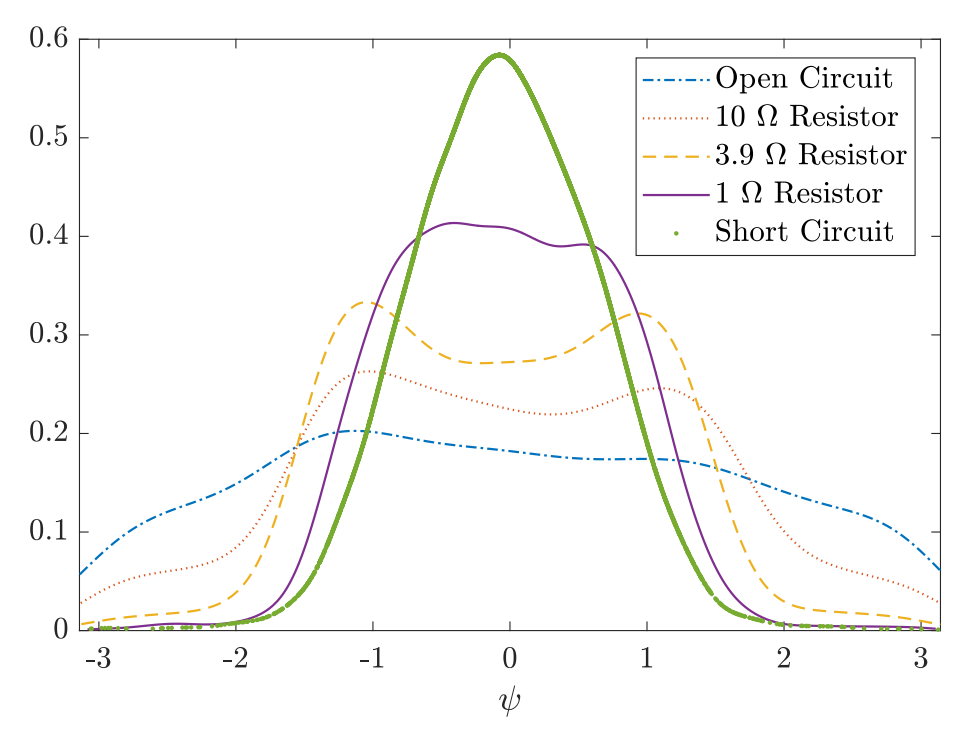


Figure 4.8 Marginal probability density functions for the pendulum angle from the experiments with 0.8g RMS excitation. Each PDF correlates with a marker in Fig. 4.6.

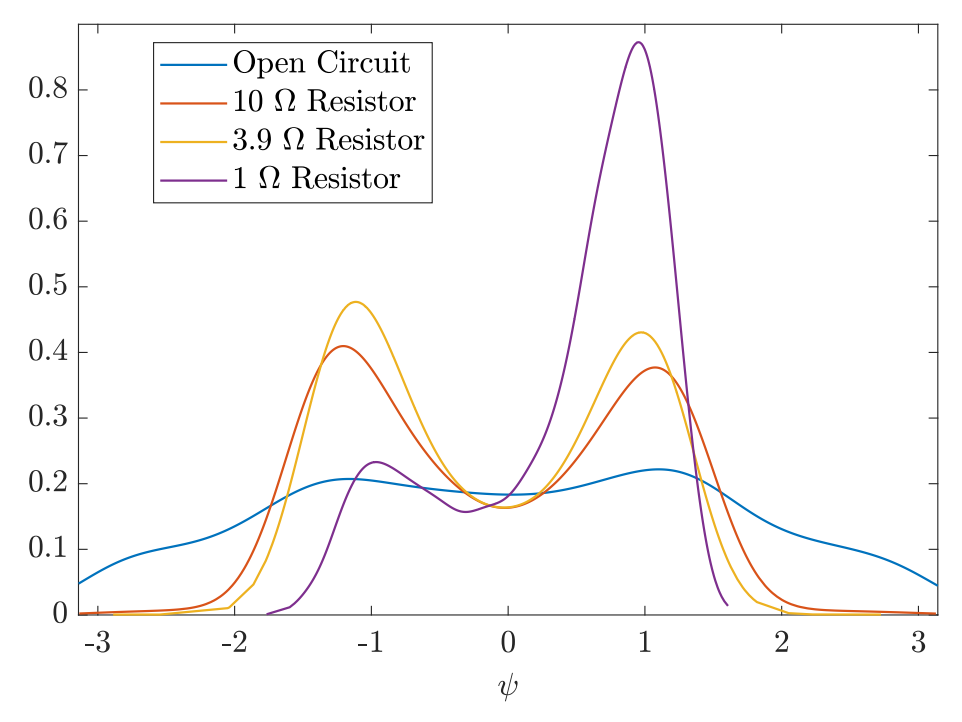


Figure 4.9 Marginal probability density functions for the pendulum angle from the experiments with $0.6g~\mathrm{RMS}$ excitation. Each PDF correlates with a square marker in Fig. 4.6.

pronounced bimodality. Furthermore, the experimental short circuit case is shown in Fig. 4.8, corresponding to the marker with the highest damping value in Fig. 4.6. The PDF is indeed more distinctly monomodal, indicating that the transition has fully occurred from bimodal to monomodal. The right bifurcation boundary has been predicted reasonably well. Moreover, if the left boundary region is accurate, the 10 Ω case is likely to display a bimodal PDF as well. Both simulation and experimental PDFs in Figs. 4.7 and 4.8 reveal this bimodality, also with rotation indicated by the separation from the ψ axis at $\psi = \pm \pi$, attributed to reduced electrical damping. Crossing the left boundary region to examine the open circuit scenario, one might anticipate another qualitative shift in the PDFs. In this instance, Figs. 4.7 and 4.8 suggest a possible flattening of the PDFs, while they show an apparent change from positive to negative curvature at the origin, indicating bifurcation. The precise nature of this change remains uncertain, yet a comparable qualitative change was noted in the Chapter 3, where the left boundary was presumed to lead to pure rotation. Lastly, Fig. 4.9 shows the experimental PDFs for 0.6q RMS acceleration. The boundary would predict that all of these should be bimodal, with the exception of the open circuit case which lies in the region of uncertainty. After closer examination, the three bimodal predictions are in fact verified, albeit more asymmetric due to frictional effects or not enough time to become stationary. The PDF with a prediction in the bifurcation region of uncertainty then appears be possibly locally bimodal with a somewhat flattening of the PDF. This indicates a potential transition towards pure rotation.

Some concluding observations pertaining to this subsection are now provided. The PDFs derived from the MCS were produced using numerous realizations in the time domain, in contrast to the PDFs associated with the experiment, which were derived from a single two-and-a-half-hour experiment. Consequently, it is highly probable that the PDFs depicted in Fig. 4.7 are closer to being stationary compared to those in Fig. 4.8, as suggested by the greater symmetry in Fig. 4.7. However, there remains a possibility that the duration of the simulation was insufficient to achieve fully developed PDFs, even if they are relatively

symmetric compared to the experimental PDFs. Furthermore, it is important to highlight that generating these PDFs took around four hours, leveraging high-performance computing resources with 8×128 CPU cores and 921.6 gigabytes of memory per 128 cores. Additionally, it should be noted that the Gaussian white noise excitation utilized in the analysis is merely an approximation of the band-limited noise employed in the experiment. Lastly, the precision of the pendulum tracking system was constrained by a sampling rate of five hundred samples per second, yet its measurement accuracy was confirmed to be within a couple of degrees. Nevertheless, the qualitative change in the PDF was predicted with the use of the approximate bifurcation boundary region.

4.3.2 Experimental Exploration of Power Harvested and Vibration Suppression

In this section, the PSDs are presented for the relative velocity of the suspended mass and harvested power computed with the data obtained from the experiments discussed in Section 4.2.3.1. Additionally, the same experiments were done for a linear benchmark system where the pendulums are removed, but equivalent inertia is added so that the natural frequency remains about the same for a fair comparison. However, note that the pendulums act as vibration absorbers and so their removal results in very high displacement amplitudes of the suspended mass. For safety and to preserve the integrity of the experiment, the linear system was excited at only half of the root mean square acceleration excitation and the resultant amplitude was scaled by two. This is simply utilizing the principles of linearity; i.e. a force twice as large will give a response twice as large. Ultimately, after this scaling, the PSDs from the linear system experiment will be compared to those from the experiment with the addition of the IPVA.

First, Fig. 4.10 shows the PSD for the electric power harvested across the resistant load. Note that the power in this work was considered as the power across the resistive load which was connected in between the generator terminals. The power harvested was calculated directly from measured voltage (V_m) as $P = V_m^2/R_l$. In this scenario, it becomes evident that the 1 Ω resistance setup correlates with the least electric power near the resonant frequency,

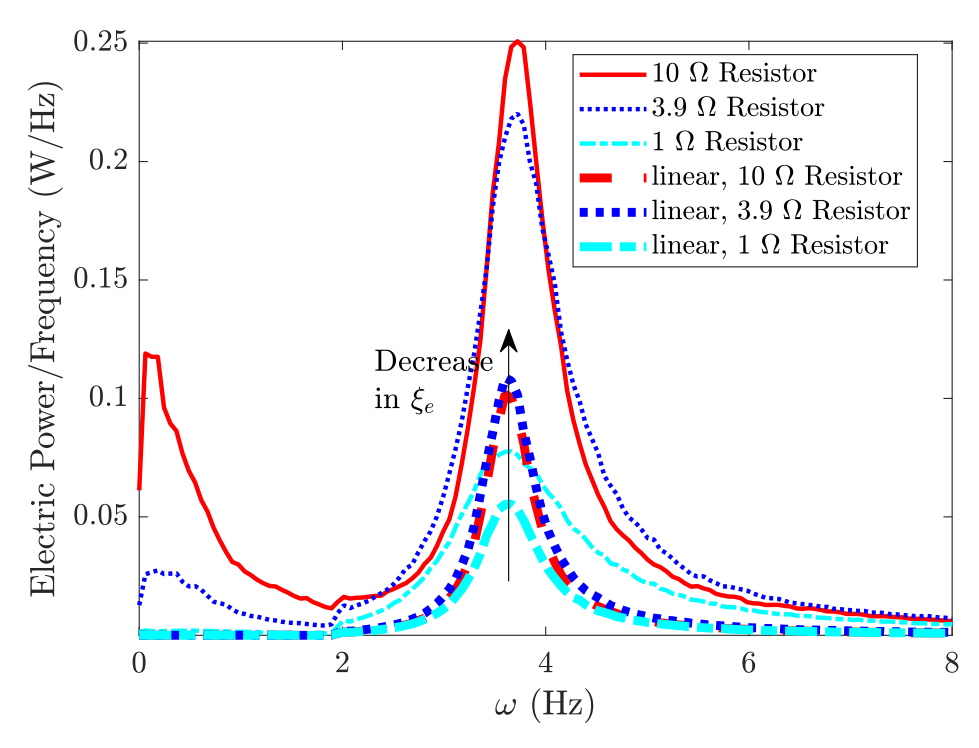


Figure 4.10 PSD for harvested power for the three finite resistant load configurations.

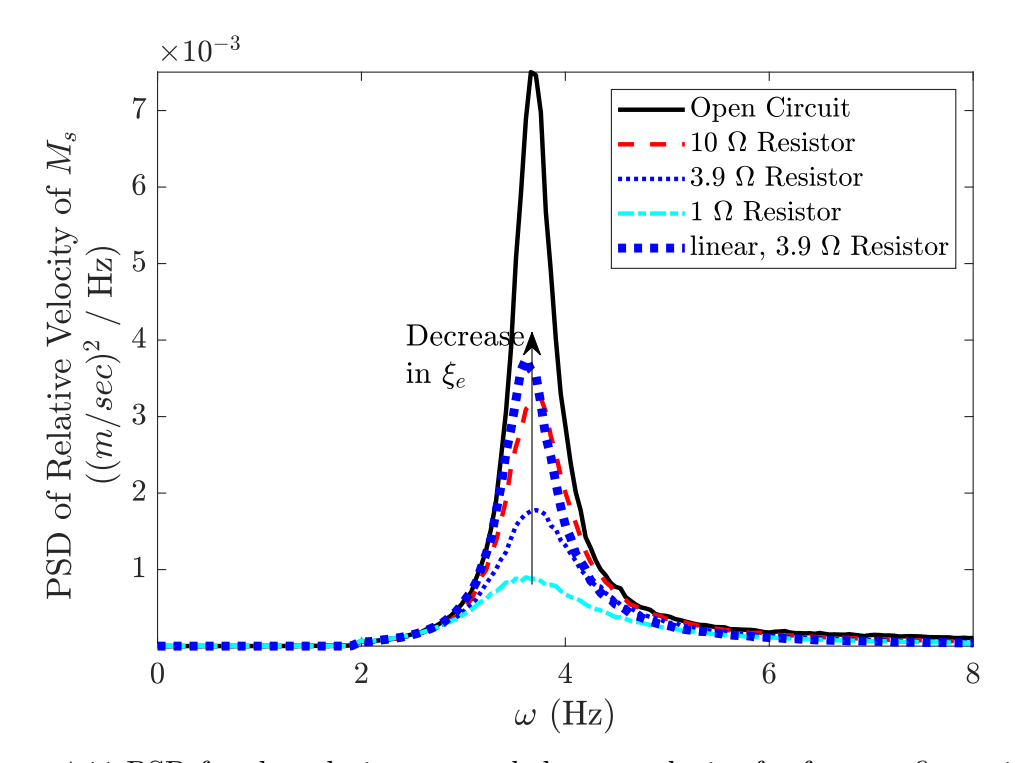


Figure 4.11 PSD for the relative suspended mass velocity for four configurations.

while it still outperforms all linear system cases in terms of mean power, calculated as the area under the PSD. A closer look at the PDF in Fig. 4.8 reveals that this 1 Ω resistance setup is also a monomodal configuration. The correlation between a monomodal PDF and suboptimal energy harvesting exists. For $R_l = 10 \Omega$, the mean power is more than a factor of four times that of the linear system, and the power near the resonant frequency is more than double compared to the best linear system ($R_l = 3.9 \Omega$). A significant portion of the mean power can be attributed to the substantial low-frequency response below the excitation frequency, including the DC component in the PSD due to the pendulums' rotation. Note that the actual amount of power is not discussed in this work as the concern is primarily with how the power correlates with the characteristics of the PDF and how the nonlinear system performance compares to that of the linear benchmark system.

Moreover, Fig. 4.11 shows the PSDs for the relative suspended mass velocity. In this case, the nonlinear system results are only compared with the linear system which uses the $3.9~\Omega$ resistor. This is because this is the configuration in which the linear system performs the best in terms of power harvesting. In fact, one can derive an optimal load resistance for the linear system. Noting that the linear system would be the same as the linear system in Chapter 2, where the linear closed-form solution for the dimensionless mean square ball screw velocity was determined and is given by

$$\langle \theta'^2 \rangle = \frac{D}{4(\xi + \xi_e)} \tag{4.18}$$

The formula for dimensionless mean power harvested $\langle \hat{P} \rangle$ then just as in Chapter 3 is

$$\langle \hat{P} \rangle = \frac{R_l}{R_i + R_l} \xi_e \langle \theta'^2 \rangle = \frac{R_l}{R_i + R_l} \frac{\xi_e D}{4(\xi + \xi_e)}$$
(4.19)

Finally, taking $\frac{\partial \langle \hat{P} \rangle}{\partial R_l} = 0$, one can find that the optimal load resistance

$$R_l^{opt} = \frac{\sqrt{R_i}\sqrt{\kappa_t^2 n_g^2 + 2M_s \xi \ \omega_0 R_i}}{\sqrt{2M_s \xi \ \omega_0}}$$

$$(4.20)$$

Using the parameters from Table 4.3, one finds when rounded to the hundredths place, $R_l^{opt} = 3.17 \Omega$, which is very close to the experimental value of 3.9 Ω .

It is clear in Fig. 4.11 that the nonlinear system once again outperforms in terms of vibration suppression near the resonant frequency except when there is an open circuit condition and electrical damping is zero. A reduction by a factor of four in the relative velocity PSD value is seen near the resonant frequency and an overall halving in the mean squared value of the relative velocity has been computed for the case of $R_l = 1 \Omega$ in the system with the IPVA. As long as power harvesting is a priority and the circuit is not open, it appears as though the IPVA will allow for superior vibration suppression and power harvesting over the linear system. This possibility for simultaneous objectives somewhat echoes the result of utilizing the device in a two-degree-of-freedom quarter car model such as in [62] and Chapter 3.

A final note is that the nonlinear system with 10 Ω resistance actually had 6% higher mean square velocity and hence worse vibration suppression. However, a linear system fully optimized for power using (4.20), given $R_l^{opt} = 3.17 \Omega$, will have a much larger mean squared value for the relative velocity of M_s . Using (4.18) one can then find an expression for the ratio of optimized mean square relative velocity $R^2 \langle \theta'^2 \rangle^{opt}$ to mean square relative velocity with another load resistance $R^2 \langle \theta'^2 \rangle$. One finds

$$\frac{\langle \theta'^2 \rangle^{opt}}{\langle \theta'^2 \rangle} = \frac{\kappa_t^2 n_g^2 + 2M_s \xi R^2 \omega_0 \left(R_i + R_l \right)}{\sqrt{2} R \left(R_i + R_l \right) \sqrt{\frac{M_s \xi \omega_0 \left(\kappa_t^2 n_g^2 + 2M_s \xi R^2 \omega_0 R_i \right)}{R_i}}}$$
(4.21)

and with Tables 4.2, 4.3, and 4.4, a 26% increase in the linear system mean squared relative velocity has been determined which would put it 20% above that of the IPVA system with $10~\Omega$ resistance. In this case, one can similarly use (4.19) and (4.20) to determine a corresponding 8% increase in power for the optimized linear system. This still gives a power that is less than 30% of the power harvested with the IPVA system and $10~\Omega$ resistance.

In concluding this section, it is important to solidify the hypothesis for why energy harvesting appears to be optimal when the nonlinear system PDF is bimodal. More specifically, the most superior power was found in the 10 Ω case. A closer look at Figs. 4.7 and 4.8 reveals that this case was also associated with a smaller decrease in PDF magnitude in between the

peaks when compared to the bimodal PDF associated with the 3.9 Ω resistance case. It is hypothesized that this smaller decrease in PDF magnitude between peaks is responsible for more frequent large amplitude jumps between the pendulum angles specified by the PDF extrema. The work in Chapter 3, which was associated with the same energy harvesting IPVA device implemented in a quarter car suspension system, also concluded that energy harvesting performance was generally better when near bifurcation, where the PDF magnitude reduction is minimal. Furthermore, this hypothesis would be analogous to how a shallow well in double potential-based systems allows for enhanced interwell oscillations which is known and exploited by many researchers such as in [6].

4.4 Discussion on Findings

In this chapter, an inertially nonlinear device was equipped with a DC generator to conduct experiments on and verify predictions regarding the modality of the marginal PDF of the pendulum angle of oscillation as well as the device's ability to suppress vibrations and harvest energy when applied to a single degree of freedom structure under Gaussian broadband base excitation, treated analytically as white noise. The experimental excitation, closely approximating Gaussian white noise within experimental constraints, involved a broadband excitation with a root mean square acceleration of 0.8g and a bandwidth of eleven cycles per second, incorporating the system's resonant frequency and a minimum value of two cycles per second.

To facilitate experimental verification, the system's unknown parameters were formally characterized with frequency domain optimization, where the optimization routine was designed to minimize the mean squared error in the pendulum velocity on the frequency band below two cycles per second while constraining the RMS velocity discrepancy between the simulations and actual experiments to be below 3%. All parameters whether measured, calculated, or characterized via the optimization routine were documented. Experiments utilized four different load resistance settings: open-circuit, 1 Ω , 3.9 Ω , and 10 Ω . Each resistance setting was associated with a unique set of damping parameters determined from

optimization. The RMS velocities and the corresponding mean power (proportional to the squared RMS velocity) were shown to be predicted within a margin of error of 3%. This signifies predictive capabilities for both power generation and vibration reduction. Additionally, a visual comparison between the simulation and the power spectral densities (PSDs) for all velocities demonstrated sufficient agreement.

A numerically determined P-bifurcation boundary in the plane of noise intensity versus electrical damping was derived for each experiment at 0.8g RMS acceleration excitation, excluding a extra test scenario with a short circuit, and a bifurcation region was established based on all four boundaries. Two clear qualitative changes were predicted and experimentally verified when noise intensity remained constant and electrical damping varied. The right boundary region indicated a transition from a bimodal to monomodal PDF, while the left boundary region suggested a potential flattening of the PDF. The validity of the bifurcation boundary was enhanced with the addition of the short-circuited experiment at 0.8g and four additional 0.6g experiments. There was significant qualitative agreement between experimental and simulation PDFs.

The power spectral density for electric power in the IPVA system was compared to a linear benchmark system. Results showed that power harvested by the IPVA was double that of the linear benchmark system near the resonant frequency, and mean power was a factor of four times that of the best linear system tested. Additionally, an analytically optimized linear system was shown to still produce less than 30% of the power harvested by the IPVA system. The IPVA configuration with the lowest performance in terms of power harvesting had the lowest load resistance of 1 Ω , associated with a monomodal PDF.

Finally, the power spectral density for the relative velocity of the suspended mass was assessed and compared to the most effective experimentally tested linear system for power harvesting, which had a load resistance of 3.9 Ω . All configurations except the open circuit configuration outperformed the linear system, by as much as a factor of four at the peak PSD value. Then all except the open circuit and 10 Ω resistance configuration had as little as half

of the mean square relative velocity associated with the linear system. It was determined that the 10 Ω resistance configuration had 6% higher mean square velocity than the tested linear system with 3.9 Ω resistive load. However, further analysis showed that a linear system that was fully optimized for power had 20% higher mean square velocity and still less than 30% of the power when compared to the 10 Ω resistance IPVA configuration.

CHAPTER 5

FUTURE AND ONGOING WORK: AN EXPERIMENTAL STUDY WITH THE FULL-SCALE ENERGY HARVESTING SHOCK ABSORBER

The full-size prototype has been built and is shown in Fig. 5.1 and the corresponding model in the quarter car is shown in Fig. 5.2. Measured and known parameters are given in Table 5.1. The objective of this chapter is to introduce the prototype, including design constraints and considerations, and fully characterize mechanical damping associated with the ball screw, generator, and pendulum motion. The MTS 810 hydraulic testing machine, equipped with the available software, lacks the capability to perform random testing. Therefore, sinusoidal testing is used and damping is determined with a parameter fitting in the time domain. Forcevelocity and force-displacement curves, as are used ubiquitously in EHSA literature such as in [86, 95], are used to qualitatively observe the effective damping ratio and the total energy dissipated. The characterized model is then used in a quarter-car model simulation with a road profile defined in the same manner as in Chapter 3 with a noise intensity correlated with a class F road (rough road) according to ISO 8608 standards [9]. Finally, power harvested, road handling, and ride comfort performance metrics are thoroughly investigated with the fitted model simulation results.



Figure 5.1 Manufactured IPVA integrated EHSA.

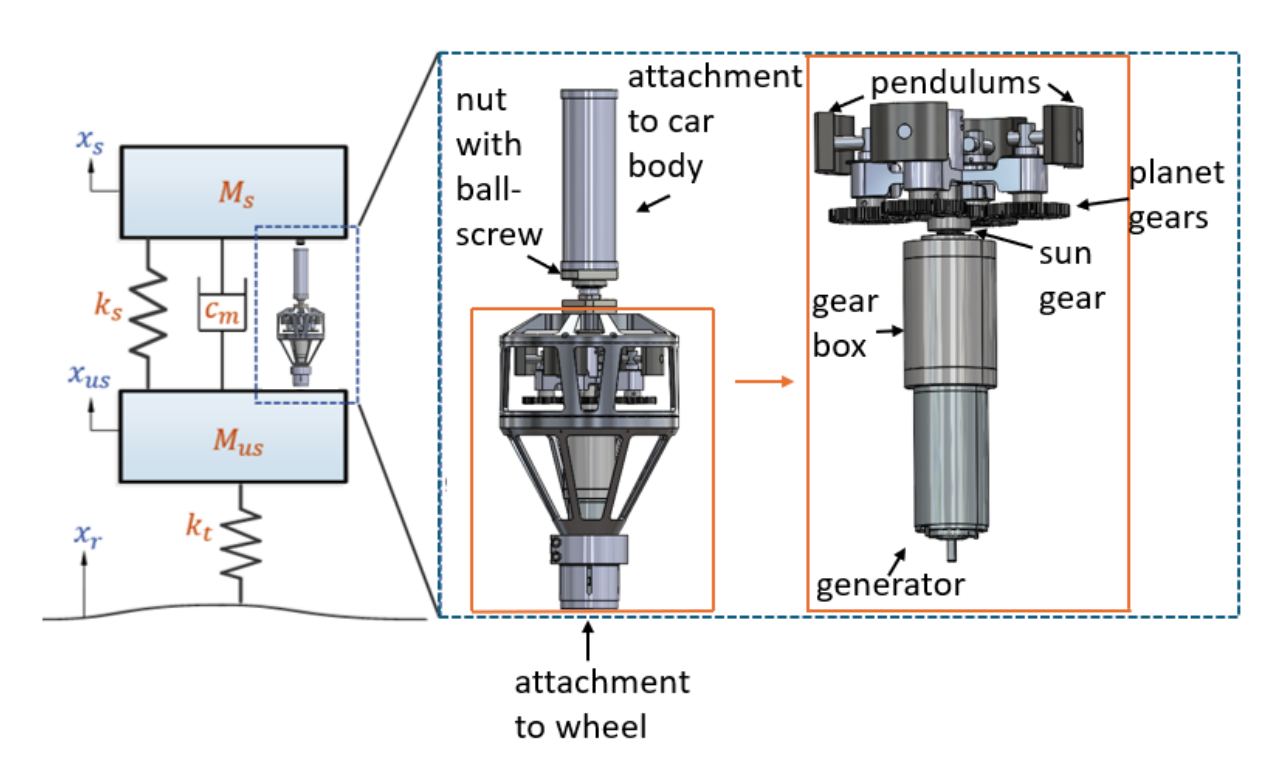


Figure 5.2 Quarter car model with IPVA integrated EHSA.

| Parameters | Value | Meaning |
|-----------------|--------------------------------|-----------------------------|
| M_s | 324 kg | Sprung Mass |
| M_{us} | 50 kg | Unsprung Mass |
| k_t | 300263 N/m | Tire stiffness |
| k_s | 110095 N/m | Suspension stiffness |
| R_p | .072 m | Carrier radius |
| m | 3.48 kg | Mass of pendulums |
| R | $0.06/(2\pi) \text{ m}$ | Effective ball screw radius |
| κ | 0.245 Nm/A | Motor torque constant |
| J_g | $1340(10^{-7}) \text{ kg m}^2$ | Generator Inertia |
| R_{int} | $1.41~\Omega$ | Motor internal resistance |
| $M_{generator}$ | 4.4 kg | Generator Mass |
| M_{total} | 15.71 kg | Prototype Mass |
| | | |

Table 5.1 Physical Prototype Parameters of the IPVA EHSA.

5.1 Physical Realization of the Prototype, Important Constraints, and Necessary Design Considerations

As demonstrated in Sec. 3.3, the P-bifurcation is critical to the suspension performance. In Sec. 3.4 the WPI algorithm efficiently estimated $\frac{\partial^2 p}{\partial \phi_f^2}$ and a simple bifurcation detection

algorithm was developed to check for change in $\operatorname{sgn}\left(\frac{\partial^2 p}{\partial \phi_f^2}\right)$. Ideally, the design of a full-scale prototype EHSA is designed as close to the model in Chapter 3 as physically possible, associated parameter values are fitted, and then the bifurcation detection algorithm and MCS are used to predict bifurcation and performance metrics near bifurcation for a few driving speeds and as a function of electrical damping on a class F-road. However, some parameters defined for the shock absorber in Chapter 3 have been deemed either impractical or not physically realizable. As one example, $\eta = 0.97$ is not physically realizable unless the carrier that holds the pendulum is unrealistically wide and most mass is concentrated near the end.

Moreover, to keep the width and height down to a size that can convincingly fit inside a passenger car wheel well, a constraint on the physical design is imposed to keep the shock diameter (d_s) below 300 mm.

The choice of the ball screw was not a trivial one to make as well. As pointed out in section 3.3, a larger lead value allows for a lower dimensionless noise intensity. This is apparent given the characteristic radius $R = \text{Lead}/2\pi$ and dimensionless intensity formula $d = \frac{2\pi G_r V}{\omega 0 R^2}$. In numerical simulation, a larger lead has also been correlated with better performance. However, it has been determined that the ball screw lead value of 100 mm leads to a very massive ball screw and nut configuration, which significantly increases the total mass of the shock absorber and decreases the specific power (power per unit mass) of the device. Another important factor to consider is the strength of the ball screw. Care was taken to choose a diameter of the ball screw which was large enough to not break in operation with potentially imperfectly aligned torsion and axial loads. Overall, a compromise between large lead, sufficient strength, and low mass has led to the choice of a 60 mm lead ball screw.

The decrease in lead value unfortunately makes the analysis from the Chapter 3 not directly usable even in the qualitative sense since μ_g is thereby amplified by $100^2/60^2$ times. A change in DC motor (used as generator) from the Maxon 353300 motor with a nominal speed of 2960 RPM to the to Maxon 353301 motor with a nominal speed of 2480 RPM has

also been done. This is because the system at hand has shown mean generator velocities $(\dot{\psi}_g = \dot{\theta} - \dot{\phi})$ values on the order of only hundreds of RPM and a nominal operating speed which is closer to the generator input speed results in superior energy harvesting. The gear ratio has also changed from $n_g = 3.8$ to 3.7 since this is what was immediately available; note that future work will likely involve a more fine tuned custom generator. Finally, these changes affect the value of μ_g and it is rightfully noted that the system dynamics have a non-trivial dependence on μ_g . This is apparent by looking at the dependence in the mass matrix from Chapter 3. Specifically, we have

$$M_{11} = \mu_g + \mu_r \left(\eta^2 + 2\eta\cos(\phi) + 1\right) + 1, \ M_{12} = \eta\mu_r(\eta + \cos(\phi)) - \mu_g, \ M_{22} = \eta^2\mu_r + \mu_g(5.1)$$

For example, investigation of M_{12} alludes to the fact that if $\mu_g > \max(\eta \mu_r(\eta + \cos(\phi)))$ there are always negative off-diagonal inertia terms. Otherwise, for $\eta < 1$, as is the requirement for no collisions of the pendulum, the off-diagonal inertia terms may be positive for certain pendulum angles of oscillation. These off-diagonal terms couple the pendulum and carrier motion. Therefore, the change in sign can play a significant role in the overall dynamics.

In order to keep the dynamics of the designed prototype similar to that of the system analyzed in the Chapter 3, an optimization routine has been developed to keep μ_g small relative to $\eta^2 \mu_r$. The optimization takes into account the following constraints: $d_s = 254$ mm, $\eta = r/R_p < 1$, the mass of the pendulums m < 4 kg giving a mass ratio $m/M_s \le 4/324 < 1.5\%$, and the height of the pendulums (h) is constrained by |h| < 50.8 mm in order to keep the total length of the shock absorber down so as to fit it in a passenger vehicle and be around the 70 cm determined from an existing shock absorber that has been measured in the lab. To achieve the pendulum weight with minimal volume, tungsten with a density of $17.99g/\text{cm}^3$ is used.

5.2 Characterization of Energy Harvesting Shock Absorber

5.2.1 Energy method with the linear system

The equations of motion associated with the shock detached from the car for experimentation are then derived using the Euler-Lagrange formulation. Specifically, they are derived in terms of dimensionless parameters but with physical time $t = \tau/\omega_0$, pendulum angle relative to the carrier ϕ (as in Chapter 3), and ball screw angular rotation about its vertical axis θ .

$$\left(\alpha + \mu_{p} + \mu_{gear} + \mu_{g} + \mu_{r} \left(\eta^{2} + 2\eta \cos(\phi) + 1\right) + \frac{M_{tran}R^{2}}{M_{s}R^{2}}\right) \ddot{\theta}
+ \left(\eta \mu_{r} (\eta + \cos(\phi)) - \mu_{g} + \mu_{p} + \mu_{gear}\right) \ddot{\phi} + 2(\xi + \xi_{e} + \xi_{f}) \omega_{0} \dot{\theta}
- 2(\xi_{e} + \xi_{f}) \omega_{0} \dot{\phi} - \mu_{r} \eta (2\dot{\phi}\dot{\theta} + (\dot{\phi})^{2}) \sin(\phi) = \frac{T_{nl}(t)}{M_{s}R^{2}},
\left(\eta \mu_{r} (\eta + \cos(\phi)) - \mu_{g} + \mu_{p} + \mu_{gear}\right) \ddot{\theta} + \left(\eta^{2} \mu_{r} + \mu_{g} + \mu_{p} + \mu_{gear}\right) \ddot{\phi}
- 2\xi_{e} \omega_{0} \dot{\theta} + (2\xi_{e} + 2\xi_{p} + 2\xi_{f}) \omega_{0} \dot{\phi} + \mu_{r} \eta (\dot{\theta})^{2} \sin(\phi) = 0$$
(5.2)

 M_{tran} is quantified as the mass which translates with the MTS hydraulic machine actuator. μ_{gear} quantifies the summation of all four planetary gear principal moment of inertia about their rotational axis. α quantifies the moment of inertia about the ball screw vertical axis for all components which rotate with the ball screw angular displacement, not including the pendulums. μ_p then quantifies the principal moment of inertia of the pendulums about the vertical axis through their center of mass. $T_{nl}(t)/R$ is the imposed force on the nonlinear shock along the ball screw rotational axis in order to prescribe the motion $x_s - x_r = R\theta$. All other parameters have been defined previously in chapter 3.

For the locked pendulum, this time with force $T_l(t)/R$, we have

$$\left(\alpha + \mu_p + \mu_{gear} + \mu_g + \mu_r(\eta^2 + 2\eta + 1) + \frac{M_{adapter}R^2}{M_sR^2}\right)\ddot{\theta} + 2(\xi + \xi_e)\omega_0\dot{\theta} = \frac{T_l(t)}{M_sR^2}$$
 (5.3)

Prescribing $\dot{\theta} = -\omega\Theta\cos\omega t$ in the case of harmonic excitation and with $\mu_{tran} = \frac{M_{tran}}{M_s}$ we have

$$T_l(t) = \Theta M_s R^2 \omega (2\omega_0 \cos(\omega t)(\xi + \xi_e + \xi_f) - (\alpha + \mu_p + \mu_{tran} + \mu_q + \mu_r (\eta + 1)^2) \omega \sin(\omega t))$$

We may also integrate (5.3) with respect to angular displacement θ over one cycle $T=2\pi/\omega$ to obtain

$$\int_{0}^{T} \left[\left(\mu_{g} + \mu_{r}(\eta^{2} + 2\eta + 1) + \mu_{tran} \right) \ddot{\theta} + 2(\xi + \xi_{e}) \omega_{0} \dot{\theta} \right] d\theta = \int_{0}^{T} \frac{T_{l}(t)}{M_{s}R^{2}} d\theta$$
 (5.4)

Then using $\int_0^T \ddot{\theta} d\theta = \int_0^T \ddot{\theta} \dot{\theta} dt = \int_0^T \frac{1}{2} \frac{d}{dt} \left(\dot{\theta}^2 \right) dt = \dot{\theta}^2 |_0^T = 0$ a relationship between work input to the system and the energy dissipated by mechanical and electrical damping is derived. Specifically, with $\int_0^T \dot{\theta}^2 dt = \pi \omega \Theta^2$ we have the following relationship between damping parameters and work input W_{in} into the system

$$\xi + \xi_e = \frac{1}{2\pi\omega\omega_0\Theta^2 M_s R^2} \int_0^T T_l(t) \dot{\theta} dt$$

$$\approx \frac{1}{2\pi\omega\omega_0\Theta^2 M_s R^2} \sum_{i=1}^{N-1} RF_l(t_i) (\theta_{i+1} - \theta_i) = \frac{1}{2\pi\omega\omega_0\Theta^2 M_s R^2} W_{in}$$
 (5.5)

Theoretically speaking, experiments can be defined and used to determine a range of values for ξ assuming known $\xi_e = c_e/(2\omega_0 R^2 M_s)$ based on the the relationship $c_e = \frac{\kappa^2 n_g^2}{R_i + R_l}$ and Table 5.1. The determined parameters can be used for further fitting of ξ_p and ξ_f with the use of 5.2. Note the linear system characterization has not been done for the sake of preserving limited time and funding; only the characterization of the nonlinear system has been done. The equations have been derived merely for completeness and to guide the proposed characterization in future work.

5.2.2 Experimental configuration, constraints, and challenges

| Load Resistance, R_l | Frequency, ω (Hz) | Amplitude, $R\Theta$ (mm) |
|------------------------|--------------------------|---------------------------|
| Open circuit | 2,6,8 | 10, 5, 2 |
| 39Ω | 2,6,8 | 10, 5, 2 |
| 22Ω | 2,6,8 | 10, 5, 2 |
| 10Ω | 2,6,8 | 10, 5, 2 |
| 4.6Ω | 2,6,8 | 10, 5, 2 |
| 1Ω | 2,6,8 | 10, 5, 2 |

Table 5.2 Experiment values for the linear system limited by the maximum current and generator speed limitations as well as a maximum input force which remains mostly periodic.

Note that the values in Table 5.2 defining the experiments obey the generator speed and maximum continuous current limitation set by the manufacturer. The experiments are designed so that the constraints of (5.6) are satisfied; the constraint equation assumed is based on the linear system velocity, but is used to at least determine a rough estimate for the upper limit of input displacement. The constraints are derived by taking the circuit of Fig. 5.3 and neglecting inductance ($L_i = 0$) due to low frequency operation of the generator, giving the circuit of Fig. 5.4.

$$i_l = \frac{\kappa n_g \theta \omega}{R_i + R_l} < 3.53 \text{ A}$$

 $\dot{\psi}_g = n_g \theta \omega < 5500 \text{ RPM}$ (5.6)

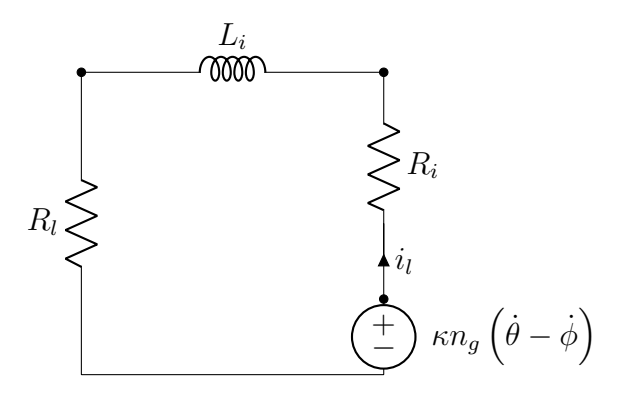


Figure 5.3 Circuit diagram with inductance.

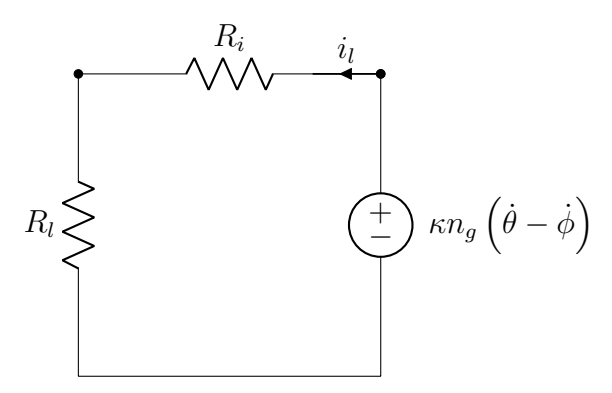


Figure 5.4 Circuit diagram neglecting inductance.

Other limitations incorporated are the MTS 810 hydraulic testing machine force limit of 25 kN and maximum peak to peak stroke of around 80 mm. Additionally, a plethora

of experimental testing showed that the force imposed (or at least the sensor reading) was in fact irregular for imposed amplitudes beyond those of Table 5.2. An example data set which demonstrates the erratic force readings is shown in Fig. 5.5; this example data set specifically corresponds to experiments with 2 Hz input displacement frequency. While the velocity reading is regular across all five experiment data sets, the force reading breaks down into irregularity for the cases of larger input velocity/displacement.

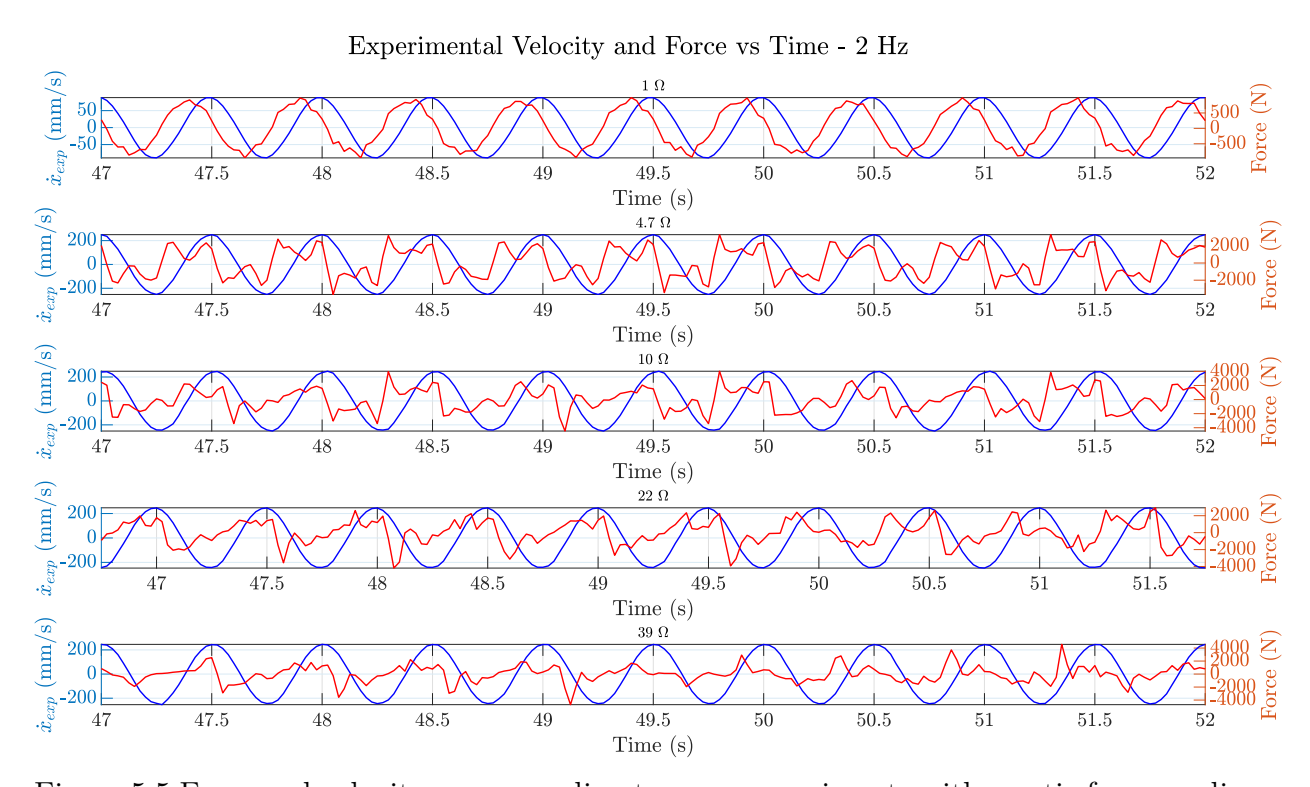


Figure 5.5 Force and velocity corresponding to some experiments with erratic force readings.

In fact, it was proven impossible to reproduce the irregular force using measured voltage and velocities and an extensive grid of damping parameters with the mathematical model defined next in the Sec. 5.2.3; this model incorporates a twist in the actuator of the machine which is introduced in the end of this section. The mathematical model is simply not capable of capturing some unknown dynamics either associated with the prototype or the MTS machine itself. The values in Table 5.2 were chosen based on trial and error and visually inspecting the force data for expected periodicity. The experiments which were kept had force sensor readings which were at least close to periodic. Experiments with aperiodic/chaotic

force readings were stored, but not used for further analysis. It is the opinion of the author of this work that irregularity of the force measurement could have been due to air in the system or possible sensor issues, but will remain unclear until further investigated in future work. Future work will attempt to identify any unmodeled dynamics in the machine itself or the prototype. If the machine itself or the sensors are responsible for unexpected dynamics, a different machine and/or sensors may be sought, allowing for higher excitation profiles. Since the use of the MTS hydraulic testing equipment available incurred hourly charges, the current research scope was not able to accommodate further investigation.

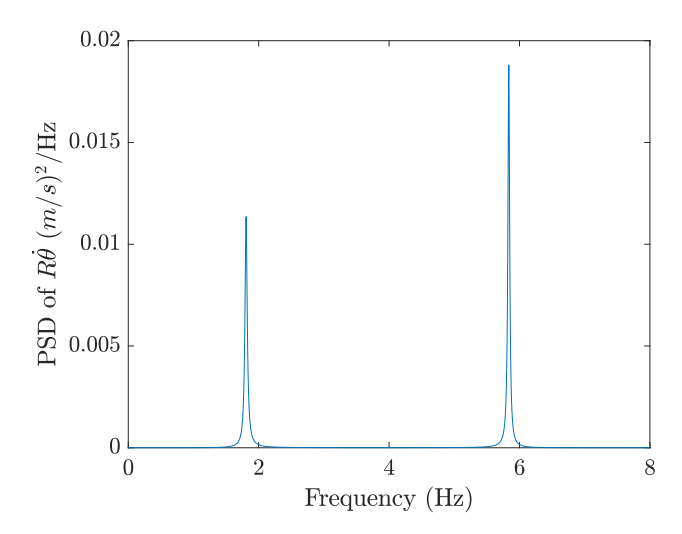


Figure 5.6 Open Circuit Linear System Displacement PSD.

Moreover, Fig. 5.6 shows a representative linear system PSD for the car body velocity when under random road excitation. It was generated with the assumption of two percent mechanical damping (ξ) and the parameters of Table 5.1. It is clear that the prominent harmonic contributions are around two and six Hertz. The harmonic fitting experiments therefore will include these frequencies in order to better represent the system dynamics, albeit with an excitation which is still not very close to the real-world excitation.

Equation (5.2) gives the idealistic view of the equations of motion associated with the system connected to the hydraulic testing machine shown in Fig. 5.7. However, the testing machine shown unfortunately is free to rotate at the bottom where the actuator connects to the shock, further complicating the experiment dynamics. As a result of this, the rotation

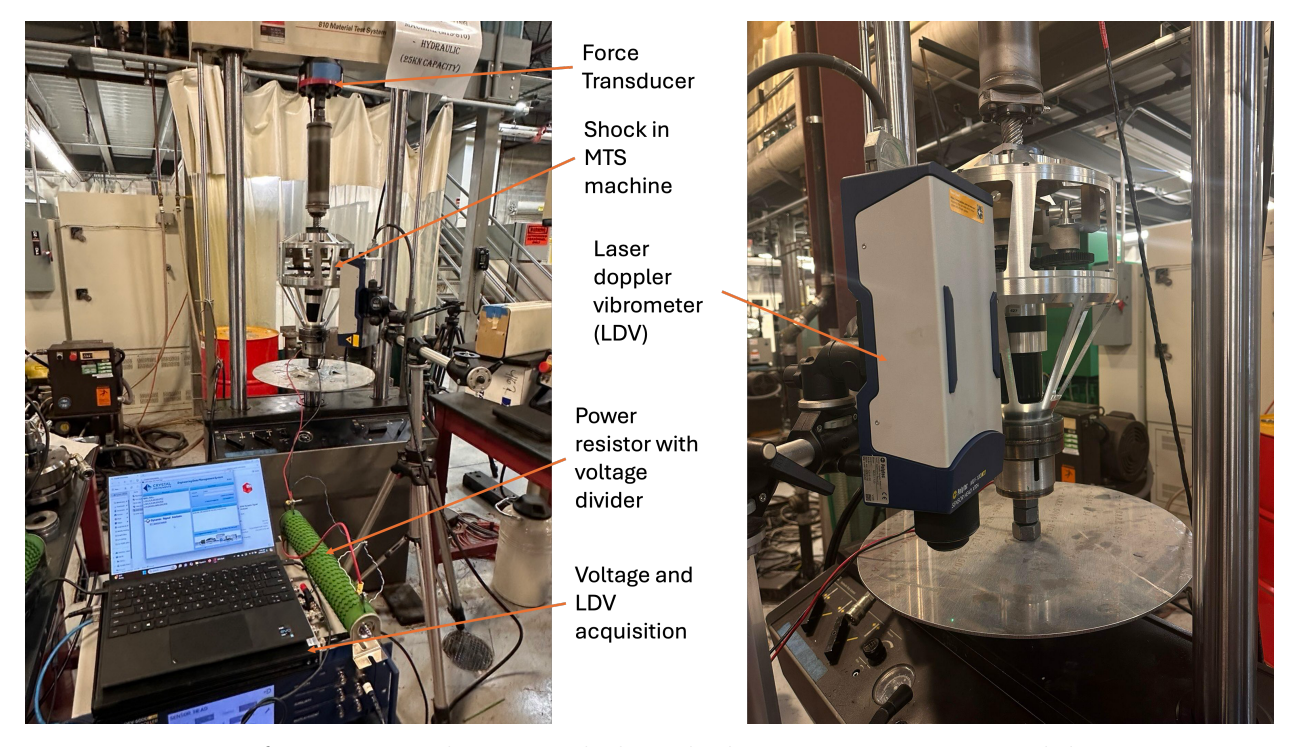


Figure 5.7 View of experimental setup including the laser, power resistor and data acquisition software.

also rotates the case which is connected to the generator housing. The mathematical model associated with this respective system including the twist is derived next in the Sec. 5.2.3

5.2.3 The experimental equations of motion including the twist degree of freedom

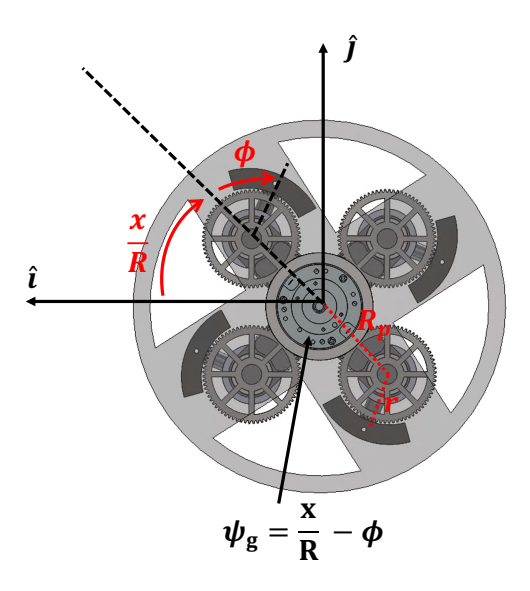


Figure 5.8 Bottom (generator side) view CAD model of the prototype with angles given.

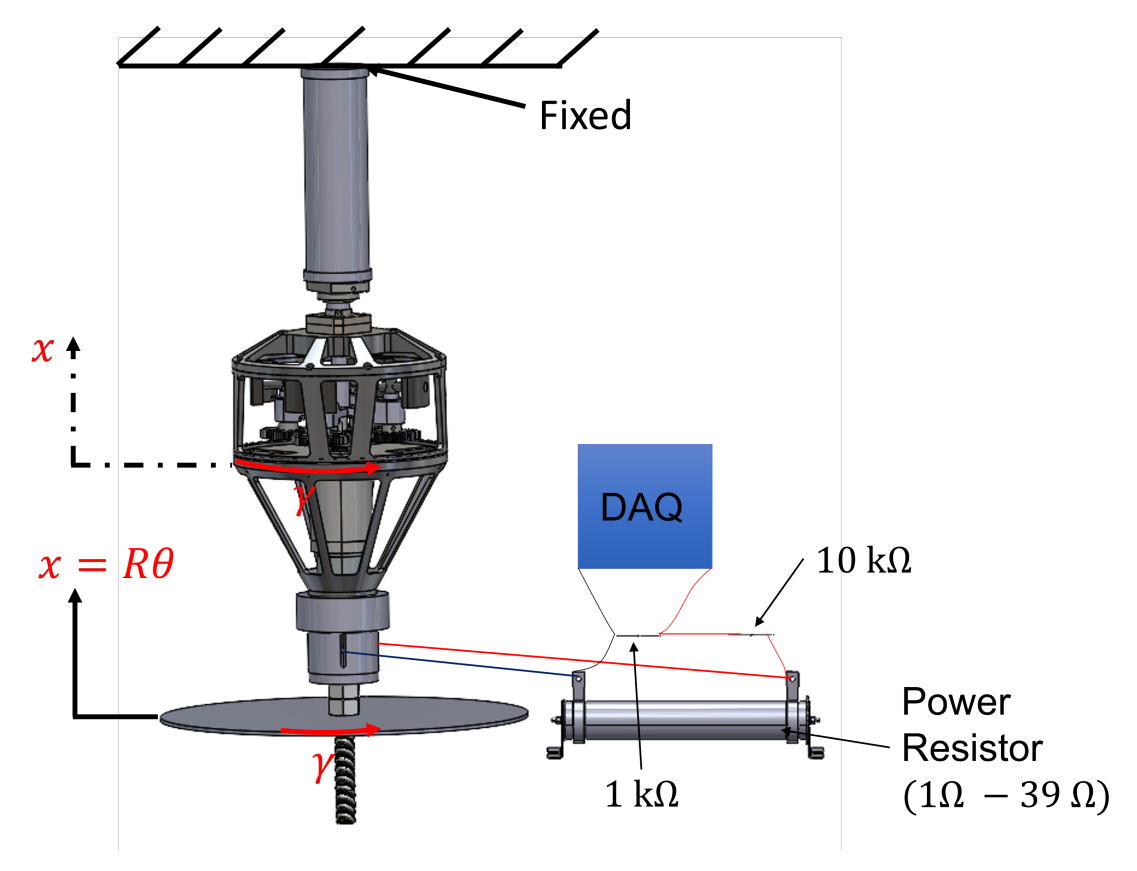


Figure 5.9 CAD model side view for the prototype with voltage divider circuit connected to DAQ.

The equations of motion now have a new angular variable γ introduced. The equations of motion are derived as follows. The position vector for the pendulum center of mass $\mathbf{r}_{\mathbf{p}}$ is

$$\mathbf{r_p} = \left(R_p \cos \left(\frac{x}{R} \right) + r \cos \left(\phi + \frac{x}{R} \right) \right) \mathbf{i}$$

$$+ \left(R_p \sin \left(\frac{x}{R} \right) + r \sin \left(\phi + \frac{x}{R} \right) \right) \mathbf{j}$$
(5.7)

where **i** and **j** are orthonormal unit vectors in the horizontal plane. This is illustrated in Fig. 5.8 which shows a cut of the prototype viewed from the bottom and looking at the generator. $x = R\theta$ is the displacement coordinate for the shock relative to the fixed end where $R = (\text{Ball Screw Lead})/(2\pi)$. Note that the pendulum angle ϕ is a measured relative to the carrier arm which rotates with angle x/R. Due to the planetary gear assembly, the generator rotor angular rotation with respect to the generator housing is then $\psi_g = x/R - \phi$. The global experimental view is then shown in Fig. 5.9 which shows the model for shock

connected to a voltage divider circuit for safe voltage measurement as well as a disk for velocity measurement with a laser doppler vibrometer (LDV).

The four pendulums then have a combined mass m and each one has a moment of inertia J_p about their vertical principal axis. The gears have mass m_{gear} and moment of inertia J_{gear} about their vertical principal axis. The case that rotates with the machine has a moment of inertia of J_{case} about the vertical axis going from the bottom connection to the top. Then all components that translate with the case have mass which sum to M_{tran} . With this in mind, the kinetic energy is written as

$$T = \frac{1}{2} \left(m \mathbf{v}_{\mathbf{p}} \cdot \mathbf{v}_{\mathbf{p}} + (4J_{p} + 4J_{gear}) \left(\dot{\phi} + \frac{\dot{x}}{R} \right)^{2} + (J_{gear}) \left(\frac{\dot{x}}{R} - \dot{\phi} \right)^{2} + (J_{c} + R_{p}^{2} m_{gear}) \left(\frac{\dot{x}}{R} \right)^{2} + M_{tran} \dot{x}^{2} + (J_{case} + J_{gen,h}) \dot{\gamma}^{2} \right)$$

$$(5.8)$$

where $\mathbf{v_p} = \frac{d}{dt}\mathbf{r_p}$ is the velocity vector for the pendulum center of mass. As a reminder, as shown in Fig. 5.8, R_p is the distance from the center of the carrier to the pendulum attachment point. J_g represents the moment of inertia for the generator rotor around its axis of rotation, $J_{gen,h}$ denotes the moment of inertia for the generator housing around its axis of rotation, and J_c represents the carrier's moment of inertia with respect to its axis of rotation.

Since there is no mechanical potential energy in the system, the next step is to write the virtual work. For simplicity in this work, only linear damping is considered; the virtual work is specifically defined to be the virtual work done by damping forces in the direction of generator motion with coefficient c_g , in the direction of pendulum motion with coefficient c_p , and in the direction of vertical translation with losses due to the ball screw and nut interface with damping coefficient c_m . Note that this c_m also includes the damping in the experiment which is inherent in the hydraulic machine actuator; the damping determined will be an overestimate. Unfortunately, determining the machine damping was not deemed possible due to limited time and is left for future work. Note there is additionally the work

due to the Lorentz force in the direction opposing generator rotor motion with coefficient c_e . Lastly, there is an assumed damping which opposes the twisting motion of the case γ with coefficient c_t , and there is a virtual work contribution from the force F(t) input to the system from the hydraulic testing machine. The virtual work is written as

$$\delta W = -(c_g + c_e) \left(\dot{x}/R - \dot{\gamma} - \dot{\phi} \right) \cdot \delta \left(x/R - \gamma - \phi \right)$$

$$+ \left(F(t) - c_m \dot{x} \right) \cdot \delta x - c_p \dot{\phi} \cdot \delta \phi - c_t \dot{\gamma} \cdot \delta \gamma$$
(5.9)

With the Euler-Lagrange equations, the equations of motion may be written as

$$\begin{pmatrix} \ddot{x} \\ \ddot{\phi} \\ \ddot{\gamma} \end{pmatrix} = \left(-\mathbf{M}^{-1} \left(\mathbf{C} \dot{\mathbf{x}} + \mathbf{g} - \mathbf{F} \right) \right)$$
 (5.10)

where $\mathbf{x} = (x, \phi, \gamma)^T$ and

$$M_{11} = \frac{\mu_p + \mu_{gear} + \alpha + \mu_{exp} + \eta^2 \mu_r + \mu_g + \mu_r + 2\eta \mu_r \cos(\phi(t))}{R}$$

$$M_{12} = \mu_p + \mu_{gear} + \eta^2 \mu_r - \mu_g + \eta \mu_r \cos(\phi(t))$$

$$M_{22} = R \left(\eta^2 \mu_r + \mu_g\right)$$

$$M_{33} = \frac{J_{case} + J_{gen,housing}}{M_e R}$$

$$\mathbf{M}(\phi) = \begin{bmatrix} M_{11} & M_{12} & 0 \\ M_{12} & M_{22} & 0 \\ 0 & 0 & M_{33} \end{bmatrix}$$

$$\mathbf{C} = \begin{bmatrix} \frac{2\omega_0(\xi_e + \xi_f + \xi_m)}{R} & -2\omega_0(\xi_e + \xi_f) & -2\omega_0(\xi_e + \xi_f) \\ -2\omega_0(\xi_e + \xi_f) & 2R\omega_0(\xi_e + \xi_f + \xi_p) & 2R\omega_0(\xi_e + \xi_f) \\ -2R\omega_0(\xi_e + \xi_f) & 2R\omega_0(\xi_e + \xi_f) & 2R\omega_0(\xi_e + \xi_f + \xi_t) \end{bmatrix}$$

$$\mathbf{g}(\phi, \dot{\phi}, \dot{x}) = \begin{bmatrix} -\frac{\eta\mu_r\dot{\phi}\sin(\phi)(R\dot{\phi} + 2\dot{x})}{R} \\ \frac{\eta\mu_r\dot{x}^2\sin(\phi)}{R} \\ 0 \end{bmatrix}, \quad \mathbf{F}(t) = \begin{bmatrix} \frac{F(t)}{M_sR} \\ 0 \\ 0 \end{bmatrix}$$

Unfortunately, the angle γ is not easily measured and the angle ϕ can be measured using the camera tracking system, but it was not feasible to modify the experimental setup within a reasonable timeline and budget; the camera may be installed in future work associated with the prototype. With that being said, the voltage V induced in the DC generator is related to the velocities with Faraday's law as given here

$$\dot{\gamma} = \left(\dot{x}/R - \dot{\phi}\right) - \frac{V}{\kappa n_g} \tag{5.11}$$

where κ and n_g are the torque constant and gear ratio, respectively, as given in Table 5.1. The relationship of (5.11) substituted into (5.10) gives a set of differential equations for x and ϕ as a function of the measured voltage (V) and input force (F). Sparing algebraic details, it is written generically in terms of some function \mathbf{f} as

$$\begin{pmatrix} \ddot{x} \\ \ddot{\phi} \end{pmatrix} = \mathbf{f} \left(\phi, \dot{x}, \dot{\phi}, V, F \right)$$
 (5.12)

In dimensionless time $\tau = \omega_0 t$, it is written as

$$\begin{pmatrix} x'' \\ \phi'' \end{pmatrix} = \frac{1}{\omega_0^2} \mathbf{f} \left(\phi, \omega_0 x', \omega_0 \phi', V, F \right)$$
 (5.13)

5.2.3.1 Fitting the model

In order to finally identify the damping parameters ξ , ξ_f , and ξ_p , an optimization routine whereby the collected data over sixty cycles (from $\tau = \tau_i$ to $\tau = \tau_f = \tau_i + 60 \times 2\pi \frac{\omega_0}{\omega}$) of input displacement $x = R\Theta \sin \omega t$ is compared to the values obtained in simulation for different electrical damping ratio values ξ_e ; an additional twenty cycles are then used to test the fitted model. The optimization routine is defined as

$$\min_{\boldsymbol{\beta}} \frac{||x'_{measured} - x'_{sim}||^2}{||x'_{measured}||^2} + w_1 \xi^2 + w_2 \xi_f^2$$

$$\boldsymbol{\beta} = [\xi, \xi_f, \xi_p, \phi'_0, \phi_0, \mu_{tran}]$$

$$s.t. \begin{pmatrix} x'' \\ \phi'' \end{pmatrix} = \frac{1}{\omega_0^2} \mathbf{f} \left(\phi, \omega_0 x', \omega_0 \phi', V(\tau), F(\tau) \right)$$

$$\begin{pmatrix} x'(0) \\ \phi(0) \\ \phi'(0) \end{pmatrix} = \begin{pmatrix} x'_{0,measured} \\ \phi_0 \\ \phi'_0 \end{pmatrix}$$

$$\tau_i \leq \tau < \tau_f$$

$$0 \leq \xi \leq 1; 0 \leq \xi_f \leq 1; 0 \leq \xi_p \leq 2$$

$$-54 \leq \phi'_0 \leq 54$$

$$-\pi \leq \phi_0 \leq \pi$$

$$0.08 \leq \mu_{tran} \leq 0.11$$

$$(5.14)$$

| Parameters | Value |
|--------------|-------|
| μ_g | 0.065 |
| μ_p | 0.05 |
| μ_{gear} | .015 |
| μ_r | 0.61 |
| α | 0.7 |
| η | 0.47 |

Table 5.3 Dimensionless Prototype Parameters.

In this work, the optimization was done with the nonlinear least squares algorithm in MATLAB; within the optimization routine the MATLAB ode45 RK4(5) integrator was used to numerically solve the coupled nonlinear odes with a relative and absolute error tolerance set to 10^{-12} . The low tolerance was deemed necessary after trial and error; it gave the most stable and consistent solution convergence.

There are few details worth mentioning regarding the optimization routine in (5.14). First, all parameters except μ_{tran} and the damping parameters were measured with a scale and measuring tools or computed with the help of *SolidWorks* CAD software; in the case of the generator parameters, the documentation was used. See Table 5.3 for the parameter values. μ_{tran} , the dimensionless quantification of translational mass, includes the mass of components that are not easily measured such as the actuator of the hydraulic machine; it was therefore left as a fitted parameter with an educated estimate of the bounds based on

the known translational masses. Next, the pendulum initial conditions are fitted as there was no collection of pendulum rotation data. As such, care must be taken when choosing the optimal parameter values from the gradient based approach in the case of multiple local minima. This was somewhat remedied in this work by adding the weighted squared damping ratio values $w_1\xi^2$ and $w_2\xi_f^2$ to the objective function; the weights were selected to keep the weighted squared values on a slightly lower order of magnitude than the term involving the error in velocity so as to not to take priority in the optimization process. This serves the purpose of forcing the optimization routine to favor solutions with lower damping. Lastly, while pendulum damping was fitted, it was determined that the the fitted values were unreasonably high; the low excitation led to very small pendulum motion, which accommodates a high damping solution. Therefore, for simulation purposes in Section 5.3, pendulum damping ξ_p is set to zero as the value determined in the small-scale experiment in Chapter 4 was negligible or zero depending on load resistance.

5.2.4 The fitted model and simulation

After the fitting process governed by the optimization routine in (5.14) a total of eighty cycles of data were used to test the associated fit; the total data set consisted of twenty cycles added to the previous sixty cycles. $\epsilon = \frac{\text{RMS}(x'_{sim} - x'_{measured})}{\text{RMS}(x'_{measured})}$ was then recorded and the fitted parameters were recorded as candidates only for the lowest two ϵ cases. These cases are given in Table 5.4 and with corresponding fitted ball screw velocity $\dot{\theta} = \dot{x}/R$ in Fig. 5.10. The measured value matches the fitted value reasonably well; error was found to be around 10% - 17% times the RMS measured velocity amplitude. At this point, it is also reiterated that the ξ damping ratio values are likely overestimates, which include the hydraulic machine damping; the values of $\xi = 0.25$ and $\xi = 0.56$ also serve as some sort of bounds on the actual damping, albeit overestimated.

| Resistance (Ω) | Frequency (Hz) | ξ | ξ_f | ξ_p | ϵ |
|-----------------------|----------------|------|---------|---------|------------|
| 1Ω | 2 Hz | 0.25 | 0 | 1.2 | 0.1730 |
| 1Ω | 4 Hz | 0.56 | 0 | 2.0 | 0.1062 |

Table 5.4 Damping solutions and corresponding ϵ for the two lowest error cases.

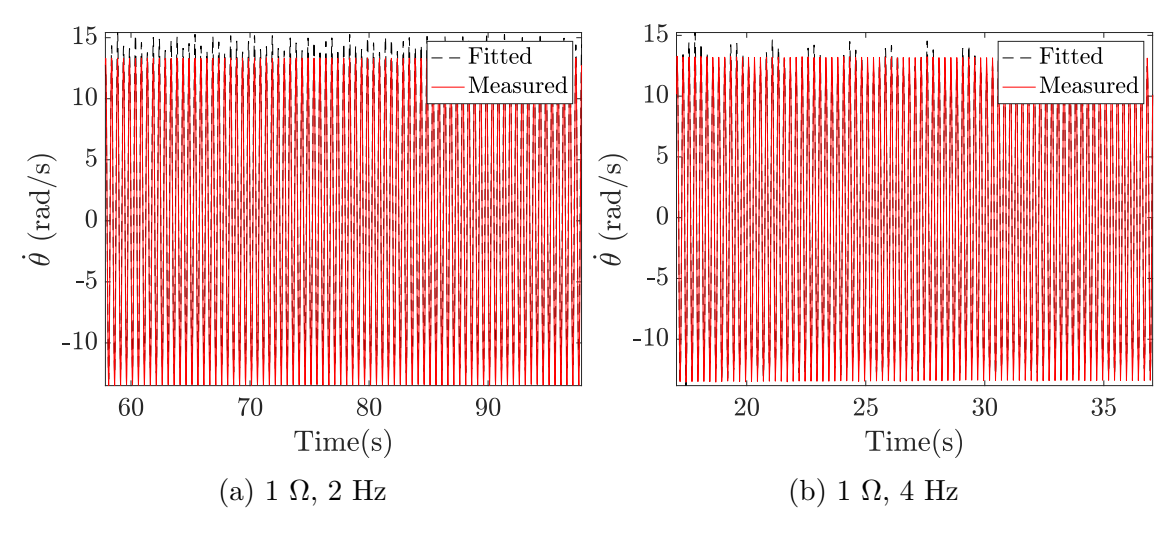


Figure 5.10 Ball screw velocity; Fitted: dashed black line; Measured: solid red line.

Since it was determined that only two of the experimental data sets were fitted with the current mathematical model reasonably well, the seemingly erratic force was further explored. As a start, the measured velocity and force corresponding to the two and four Hz cases are shown in Figs. 5.11 and 5.12, respectively. The 1 Ω case clearly exhibits the most periodic forcing; it was actually determined that it was not possible to reproduce the force in the other cases via simulation with the current mathematical model, within some reasonable error bounds. Additional unmodeled dynamics could be prominent. To further demonstrate that the measured force F(t) is not reproducible, F(t) and ϕ are herein simultaneously obtained via numerical simulation while using the optimized parameters in β and experimentally determined quantities \dot{x} , \ddot{x} , and V(t). Specifically, (5.10) and (5.11) are combined and rearranged to obtain

$$\begin{pmatrix} F(t) \\ \ddot{\phi} \end{pmatrix} = -\mathbf{A}^{-1}(\phi) \left(\mathbf{B}\dot{\mathbf{y}} + \mathbf{g_2} - \mathbf{F_2} \right)$$
 (5.15)

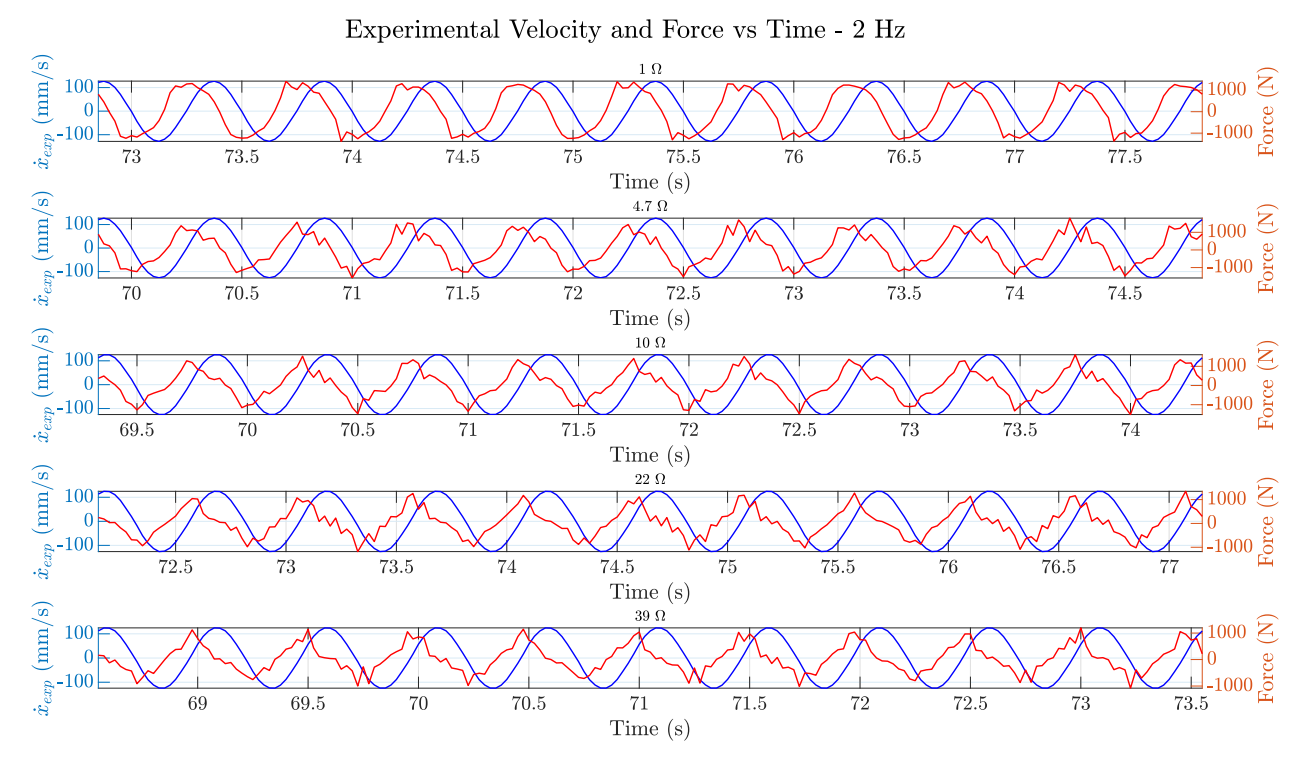


Figure 5.11 Example experiment measured velocity and force - 2 Hz displacement frequency.

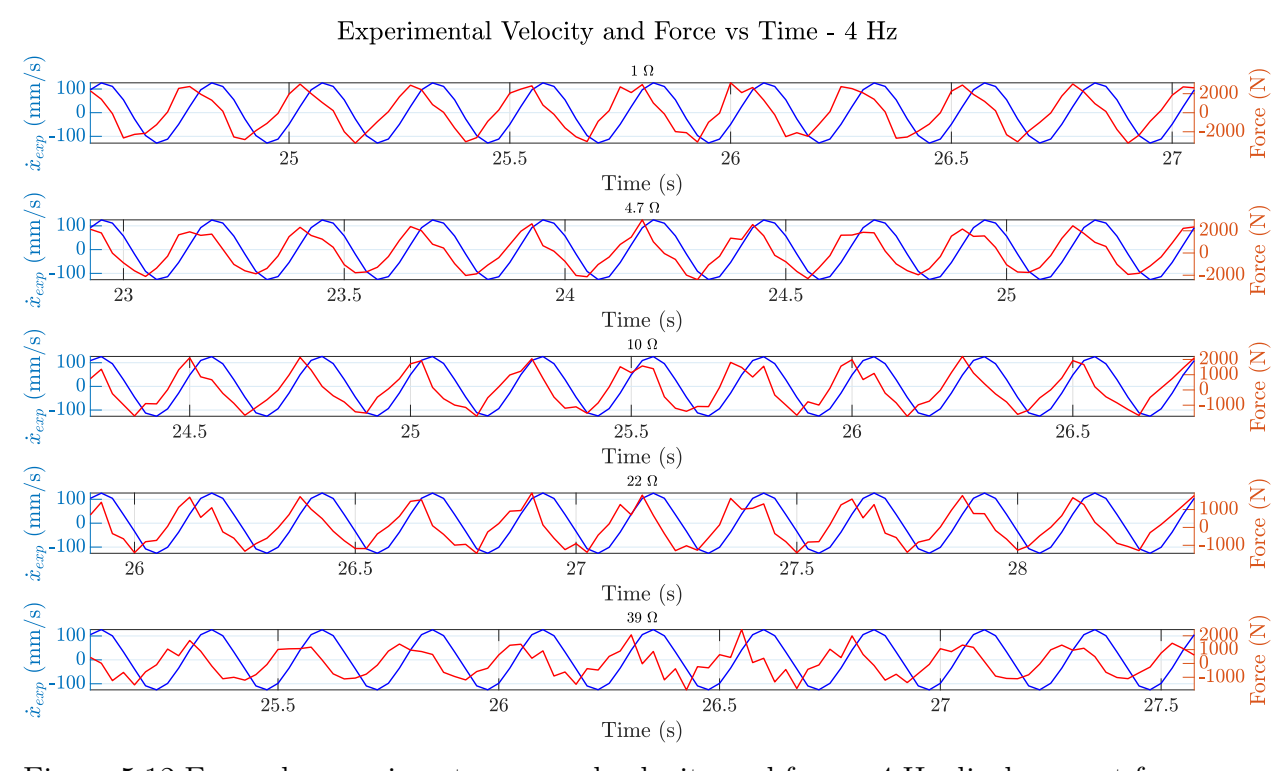


Figure 5.12 Example experiment measured velocity and force - 4 Hz displacement frequency.

with

$$\dot{\mathbf{y}} = \begin{pmatrix} \dot{x} \\ \dot{\phi} \\ \frac{\dot{x}}{R} - \dot{\phi} - \frac{V}{\kappa n_g} \end{pmatrix}$$

$$\mathbf{A} (\phi) = \begin{bmatrix} \frac{1}{M_s R} & -M_{12} \\ 0 & M_{22} \end{bmatrix}$$

$$\mathbf{B} = \begin{bmatrix} -\frac{2\omega_0(\xi_e + \xi_f + \xi_m)}{R} & 2\omega_0(\xi_e + \xi_f) & 2\omega_0(\xi_e + \xi_f) \\ -2\omega_0(\xi_e + \xi_f) & 2R\omega_0(\xi_e + \xi_f + \xi_p) & 2R\omega_0(\xi_e + \xi_f) \end{bmatrix}$$

$$\mathbf{g_2} (\phi, \dot{\phi}, \dot{x}) = \begin{pmatrix} \frac{\eta\mu_r \dot{\phi} \sin(\phi)(R\dot{\phi} + 2\dot{x})}{R} \\ \frac{\eta\mu_r \dot{x}^2 \sin(\phi)}{R} \end{pmatrix}, \quad \mathbf{F_2} = \begin{pmatrix} M_{11} \ddot{x} \\ -M_{21} \ddot{x} \end{pmatrix}$$

Finally, the resulting simulated vs. experimentally measured force for the two cases from Table 5.4 as well as two additional cases which highlight a large discrepancy between the measured and simulated force is shown in Fig. 5.13; the cases with large discrepancies correspond to the 39 Ω cases with 2 Hz and 4 Hz displacement frequencies. The large discrepancy between the experimentally measured force and the modeled force is evident in the 39 Ω cases, while the 1 Ω cases exhibit reasonable agreement.

It is also important to quantify the twist rate due to the imperfect machine. As such, the fitted pendulum angle ϕ and twist rate $\dot{\gamma}$ along with the measured force and voltage used as inputs in the EOM are shown in Fig. 5.14. It is evident that due to low excitation conditions, the pendulum velocity relative to the carrier is relatively low, while the simulated twist variable due to the unwanted twisting in the machine actuator was on the same order of magnitude as the ball screw velocity shown in Fig. 5.10. This is undesirable and is not representative of the real application in a vehicle suspension as the twist would surely be zero in that case. It is therefore difficult to make any remarks regarding performance of the shock absorber; only the determined ξ and ξ_f values from Table 5.4 are assumed to be somewhat accurate and are used in the next section for simulation purposes.

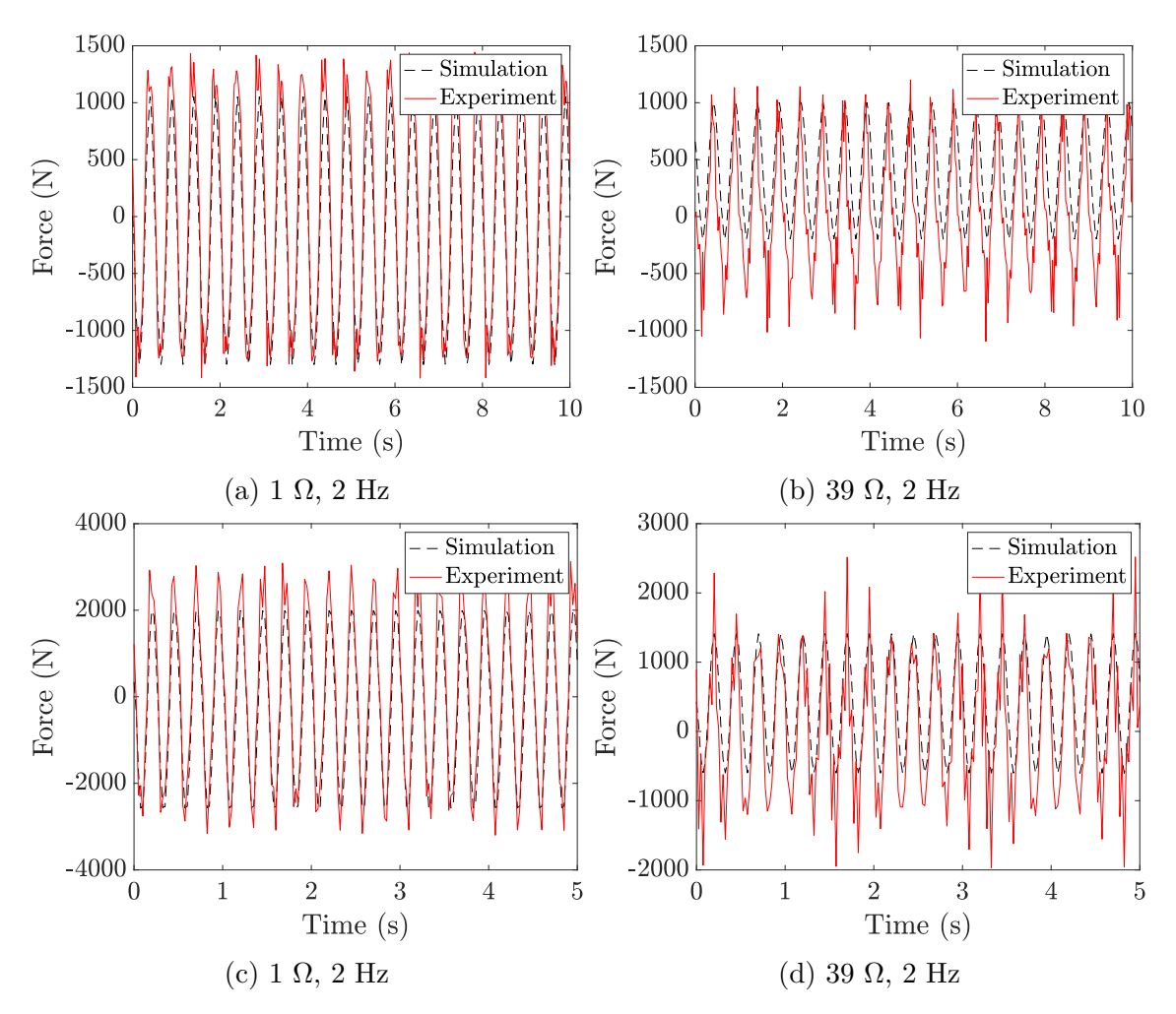


Figure 5.13 Examples of measured vs. simulated force. Simulation: dashed black line; Experiment: solid red line.

Lastly, shown in Fig. 5.15 are the associated force-velocity and force-displacement curves for the nonlinear system. The fitted force-velocity curve is relatively accurate, but this is expected since force was measured and the velocity from simulation was already shown to match the velocity from experiment with $\epsilon < 0.18$. More importantly, the force-velocity slope can give an indication of the effective linear damping constant while the area enclosed in the force-displacement curve gives an indication of total energy dissipated. The slope of the force-displacement curve is also related to the effective stiffness (positive slope) and inertia (negative slope). It is apparent, as would be expected, that the system is inertia dominant. With that being said, the final remark is that the force-velocity and force-displacement curves cannot truly give any meaningful effective damping/stiffness/inertia information regarding

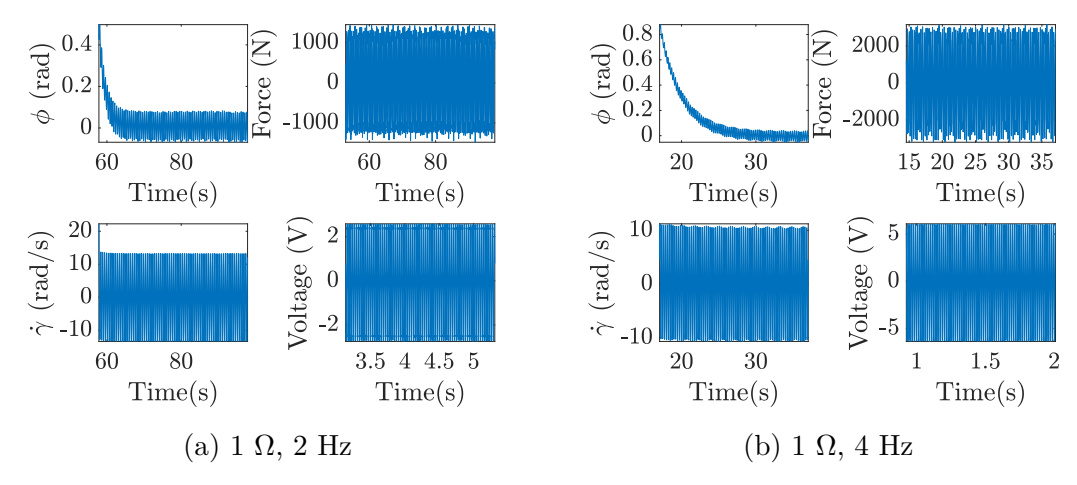


Figure 5.14 Fitted pendulum angle ϕ and twist rate $\dot{\gamma}$. Measured force and voltage were used as inputs in the EOM during fitting.

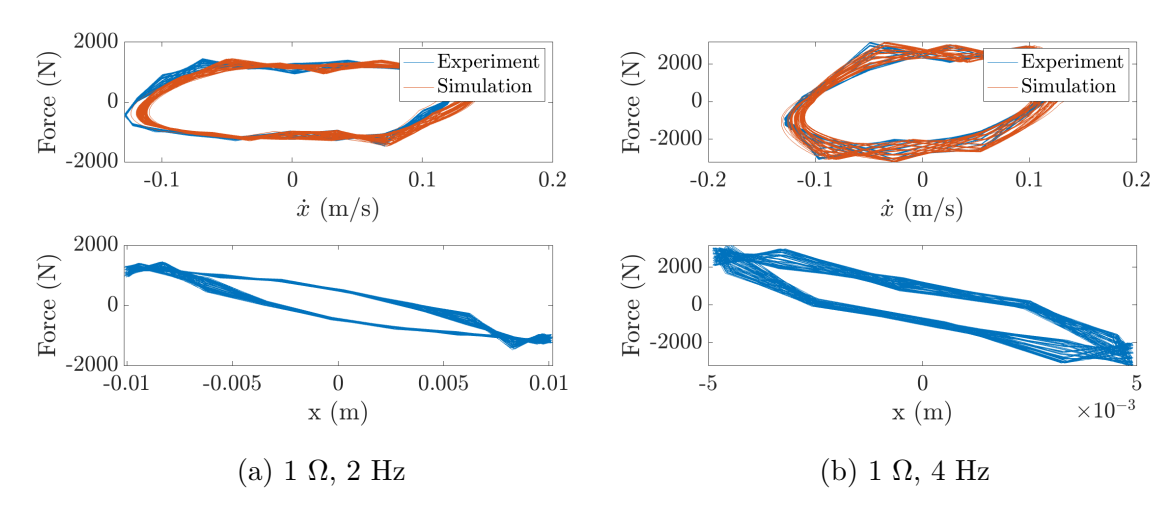


Figure 5.15 Force vs. velocity (top) and force vs. velocity (bottom)

the actual system of interest as the twist rate $\dot{\gamma}$ was too large. The plots are therefore shown mostly just for completeness. A thorough study involving the curves will be left for future work.

5.3 Simulation of the Quarter Car Model with Identified Damping

With $\mathbf{z} = [\theta, \phi, \psi_{us}]^T$, the dimensionless EOM for the shock in the quarter car model (assuming no twist) shown in Fig. 5.2 are essentially the same as in Chapter 3 with the addition of the α , μ_{gear} , and μ_p terms since these are not negligible inertia terms. Pendulum damping is also assumed to be negligible and is not included as mentioned in the previous

section. The EOM are:

$$\mathbf{Mz''} + \mathbf{Cz'} + \mathbf{Kz} = \mathbf{F}(\mathbf{z}, \mathbf{z'}, \Psi_r)$$
(5.16)

where

$$\mathbf{M} = \begin{bmatrix} M_{11} & M_{12} & 1 \\ M_{12} & M_{22} & 0 \\ 1 & 0 & u+1 \end{bmatrix}, \mathbf{C} = \begin{bmatrix} 2(\xi + \xi_{e}) & -2\xi_{e} & 0 \\ -2\xi_{e} & 2\xi_{e} & 0 \\ 0 & 0 & 0 \end{bmatrix}, \mathbf{K} = \begin{bmatrix} 1 & 0 & 0 \\ 0 & 0 & 0 \\ 0 & 0 & uv^{2} \end{bmatrix},$$

$$\mathbf{F}(\mathbf{z}, \mathbf{z}', \Psi_{r}) = \begin{pmatrix} \mu_{r} \eta (2\phi'\theta' + (\phi')^{2}) \sin(\phi) \\ -\mu_{r} \eta (\theta')^{2} \sin(\phi) \\ uv^{2}\Psi_{r} \end{pmatrix}$$
(5.17)

and

$$M_{11} = \alpha + \mu_{gear} + \mu_p + \mu_g + \mu_r \left(\eta^2 + 2\eta\cos(\phi) + 1\right) + 1$$
$$M_{12} = \mu_{gear} + \mu_p + \eta\mu_r(\eta + \cos(\phi)) - \mu_g$$
$$M_{22} = \mu_{gear} + \mu_p + \eta^2\mu_r + \mu_g$$

 Ψ_r corresponds to the dimensionless road profile acting as the excitation. The EOM for the road excitation is given here

$$\Psi_r' + v_c \Psi_r = n(\tau) \tag{5.18}$$

where the dimensionless white noise is defined thoroughly in Chapter 3. Note that in this work, cutoff frequency v_c is actually set to zero as it was shown to speed up the simulation. The role of the cutoff frequency is to keep the zero-frequency component for the road displacement bounded; the RMS road displacement will otherwise grow unbounded. However, the author, Cosner, has determined via direct simulation that the cutoff frequency has negligible effects on the overall dynamics of the system and so may be safely set to zero.

Finally, the equations of motion were solved using the parameters of Table 5.3 and Table 5.4 with $\xi_p = 0$. $u = M_{us}/M_s$ and $v = \frac{\sqrt{k_t/M_{us}}}{\sqrt{k_s/M_s}}$ were calculated with parameters in Table 5.1. For a driving speed of 5 m/s on an extremely rough road (off-road), the dimensionless

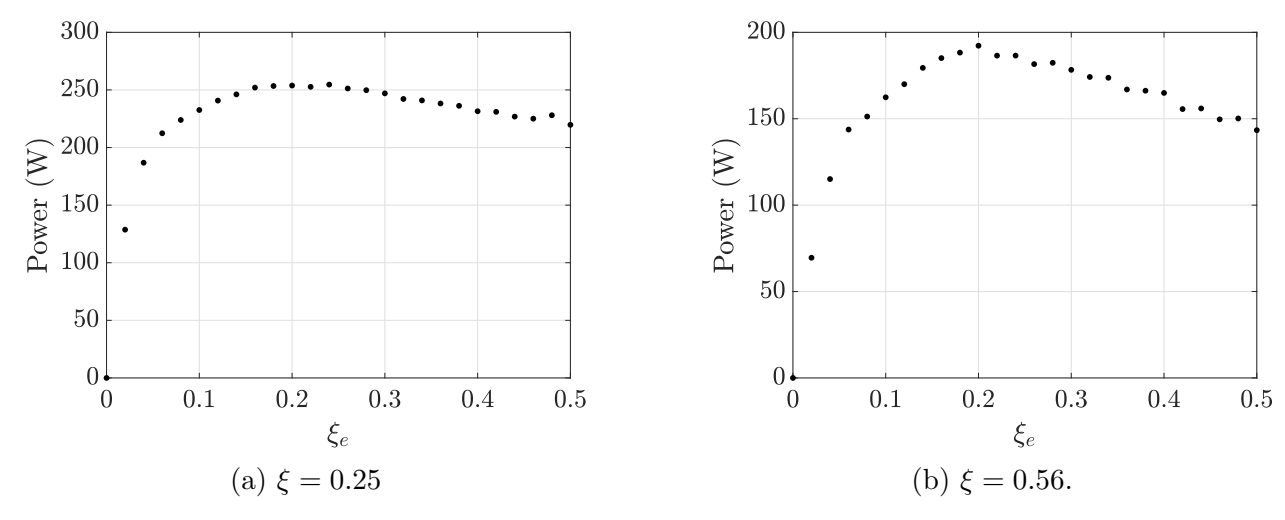


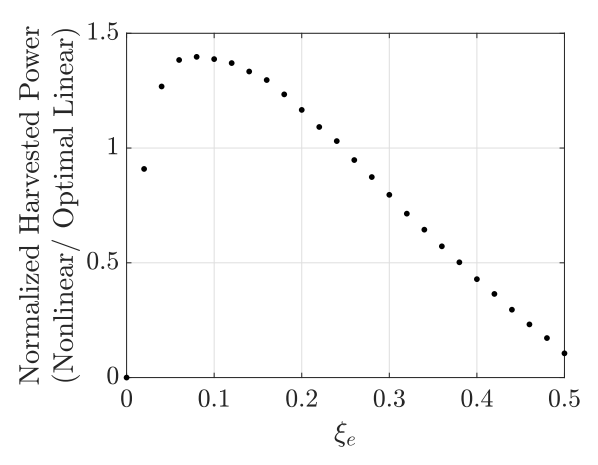
Figure 5.16 Power into electrical domain versus electrical damping ξ_e .

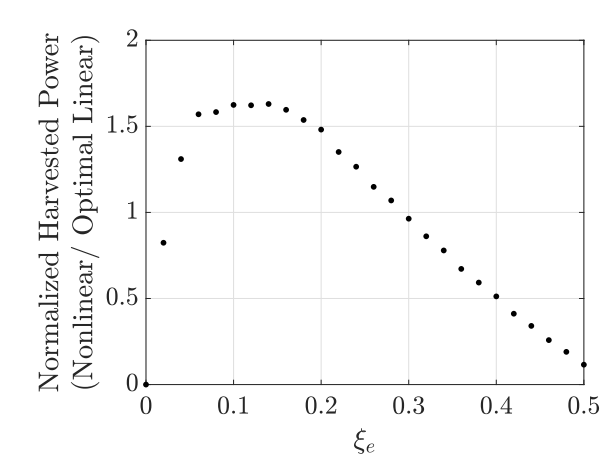
noise intensity is also taken as d=1.94. This would correspond to a reasonable driving speed on off-road style terrain. The numerical simulation was done with a Euler-Maruyama based stochastic differential equation (SDE) solver found in the MATLAB Financial Toolbox with a dimensionless time step set to 10^{-3} and total dimensionless time of 1000 units. The MCS consisted of $35(10^3)$ simulations for a range of ξ_e values on the interval [0, 0.5]; the highest value that the generator can accommodate is only very slightly higher than $\xi_e = 0.5$. It should lastly be noted that the results to be introduced in this section should give an indication of the possible bounds of performance, but they cannot be used to draw any precise conclusions since the $\xi = 0.25$ fitted model and the $\xi = 0.56$ model may lead to very different system dynamics.

5.3.1 Quarter car model simulation results

Power into the electrical domain (i.e. with no losses due to internal resistance) is shown for the $\xi = 0.25$ case in Fig. 5.16a and for the $\xi = 0.56$ case in Fig. 5.16b. The peak power occurs near $\xi_e = 0.2$ in both cases at around 250 W for $\xi = 0.25$ and slightly under 200 W for $\xi = 0.56$.

Furthermore, the optimal linear system power may be calculated and remains the same as (3.33) in Chapter 3. With electrical efficiency considerations (resistive losses) in the nonlinear system, nonlinear system harvested power is normalized with respect to the optimized linear





- (a) $\xi = 0.25$; Optimal linear power is 136 W.
- (b) $\xi = 0.56$. Optimal linear power is 81 W.

Figure 5.17 Power harvested normalized with the optimized linear system versus electrical damping ξ_e .

system and is shown for $\xi = 0.25$ in Fig. 5.17a and for $\xi = 0.56$ in Fig. 5.17b; a value greater than unity means that the power exceeds that of the optimized linear benchmark system. In fact, peak power harvested seems to exceed the linear benchmark system by around 40% for the $\xi = 0.25$ case and around 60% for the $\xi = 0.56$ case. This amounts to a power of around 190 Watts and 130 Watts respectively; the optimal damping has also shifted to around $\xi_e = 0.1$. It is apparent that the choice of the generator led to subpar efficiency. A better implementation in the future will most likely involve a customized generator that may cater to high efficiency needs.

The sprung mass acceleration normalized with respect to the linear benchmark system optimized for power is shown for the $\xi = 0.25$ case in Fig. 5.18a and for the $\xi = 0.56$ case in Fig. 5.18b. Notably, peak performance occurs again near $\xi_e = 0.1$ with around a 20% sprung mass acceleration reduction in comparison with the linear benchmark system.

The RHI, the ratio of the RMS dynamic load at the road to the vehicle weight (lower is better for road handling), is normalized with respect to the linear benchmark system optimized for power is shown for the $\xi = 0.25$ case in Fig. 5.19a and for the $\xi = 0.56$ case in Fig. 5.19b. Interestingly, the normalized RHI is very similar (to the naked eye) to the normalized sprung mass acceleration.

To gain more insight into the performance in terms of the relationship with the pendulum

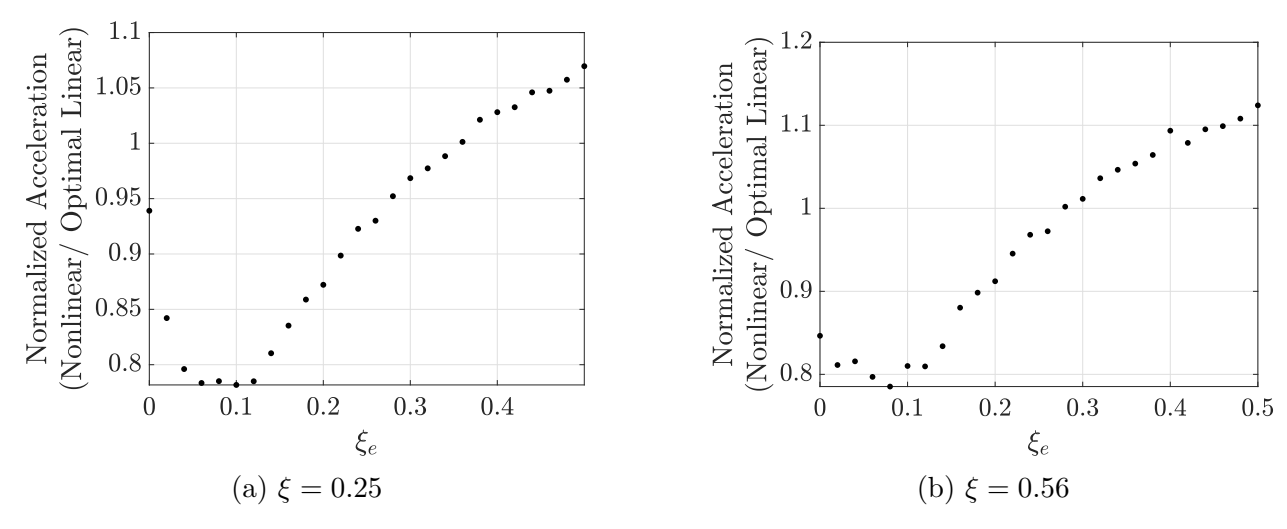


Figure 5.18 Sprung mass acceleration normalized with the optimized linear system versus electrical damping ξ_e .

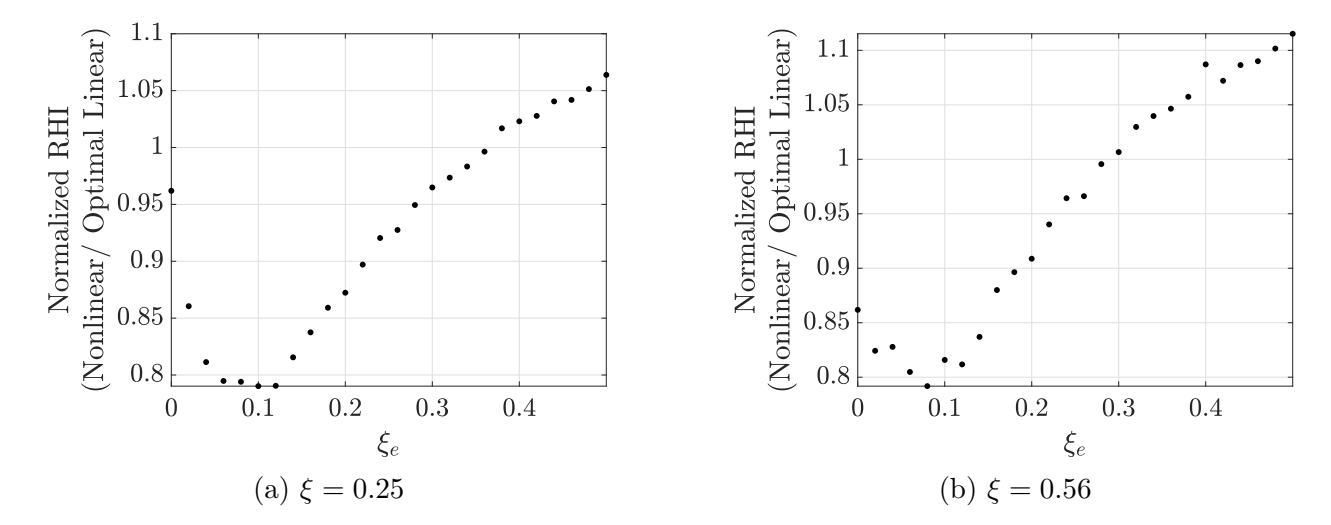


Figure 5.19 RHI normalized with the optimized linear system versus electrical damping ξ_e .

dynamics, the marginal PDF (all other states are integrated out) for the pendulum angle ϕ is shown for a few ξ_e values in Fig. 5.20. It should be noted that the wrapToPi function in *MATLAB 2023b* was used to keep the pendulum angle on the domain of $[-\pi, \pi]$; this leads to the notable separation at $\phi = \pm \pi$ when large rotations exist. Also, for each ξ case, the marginal PDFs are separated into two plots in order to more clearly observe qualitative changes with varying ξ_e . The first thing to look at is the qualitative nature of the PDFs with $\xi_e \leq 0.24$ in Figs. 5.20a and Figs. 5.20b. Once again, the optimal performance in terms of power, ride comfort, and road handling was found to occur at around $\xi_e = 0.1$. This

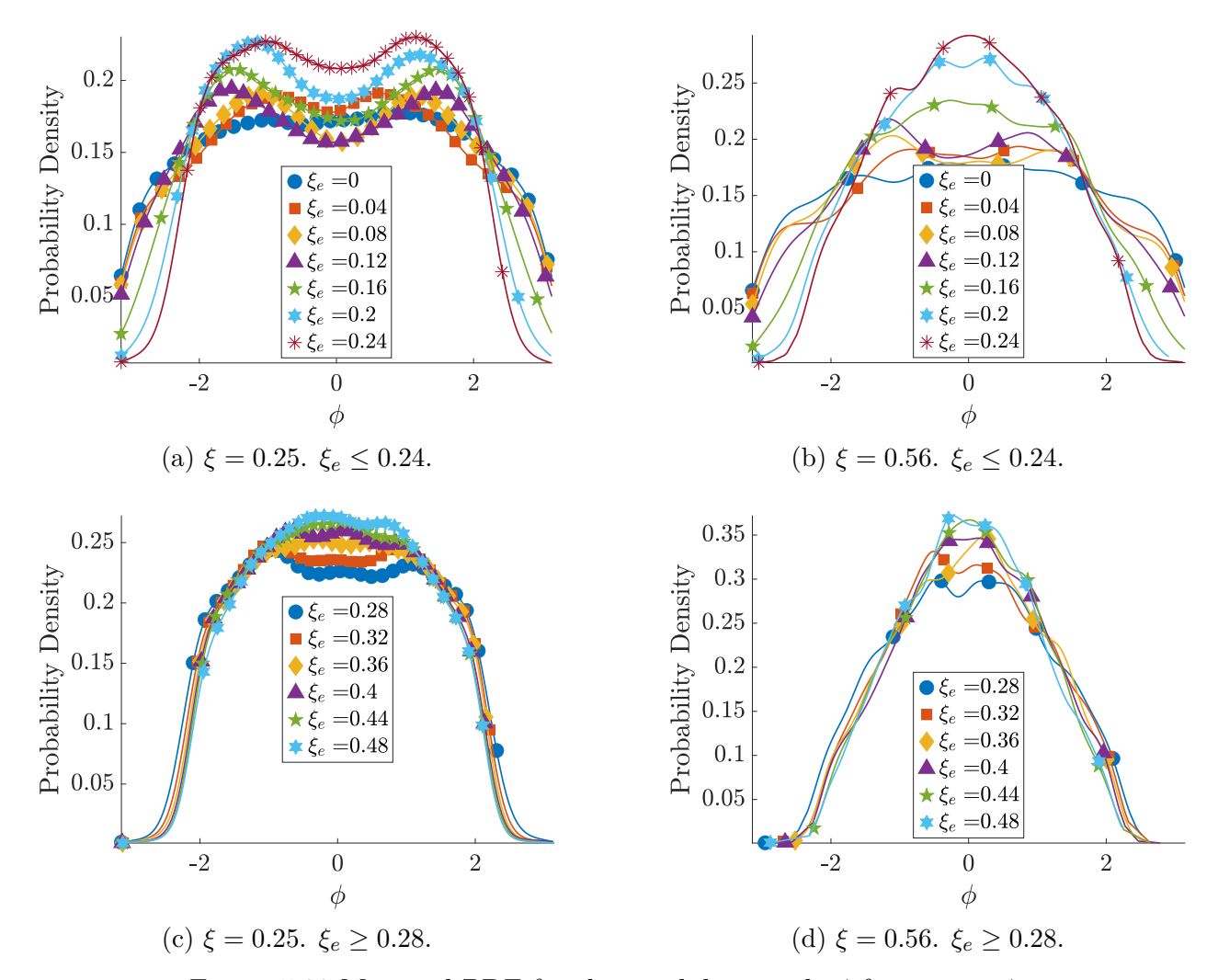


Figure 5.20 Marginal PDF for the pendulum angle ϕ for various ξ_e .

corresponds to between the triangle and diamond marked PDFs in the figures.

In the case of $\xi = 0.25$, the probability density functions around $\xi_e = 0.1$ are clearly bimodal. Additionally, the probability densities at the origin seems to remain the same, while the curvature at origin decreases with the ξ_e increase; this is accompanied by a slightly broadened set of peaks. This potentially indicates improvements are based on enhanced large jumps in the pendulum angle of oscillation.

In the case of $\xi = 0.56$, the probability density functions around $\xi_e = 0.1$ are perhaps bimodal or even have more peaks than two (multimodal). In this case, it is a little less clear. It is possible that the dynamics have become significantly more complicated at high ξ , or there were not enough simulations for convergence to stationary PDFs. Given the fact that the total simulation was well over 2.5 hours using over 7×900 GB of memory and 7×128 cpu cores on the Michigan State University ICER HPCC, more simulations would likely not be justifiable. With that aside, the most objectively determined change is that of increased probability density in the region between inner peaks for an increase in electrical damping.

Finally, in the case of $\xi = 0.25$ and $\xi = 0.56$ with $\xi_e \ge 0.28$, the main notable qualitative change is that of increasing probability density at the origin, indicating a potentially more monomodal (single peak) system.

5.4 Discussion on Findings

In concluding this chapter, it is first noted that the simulation results seemed to agree qualitatively with the overlying theme associated with the conclusions in Chapters 2, 3, and 4. That is, performance in terms of energy transfer from the structure in question to the pendulums and/or electrical domain seems to be enhanced when the system is near P-bifurcation or bimodal with small variation between peaks. Road handling specifically, quantified by the RMS tire dynamic force to gravity force ratio (lower is better) was shown to also be enhanced simultaneously in the quarter car model. This bimodality/P-bifurcation that is associated with multi-objective performance was specifically made possible with the introduction of inertial nonlinearity; in fact, the energy harvesting absorber device is free of mechanical potential energy.

Next, it is noted that future work is needed for any absolute conclusions with high objectivity regarding the quarter car model simulation results in this chapter. There are a few reasons for this. One is that the inability of the hydraulic testing machine to impose vertical displacement motion with high accuracy without inducing the added twist motion makes the results questionable. The twisting motion has a notable effect on the voltage from the generator; the voltage is in turn coupled with the rest of the system. A better/more stable machine which is more suitable for cyclic or random displacement testing will ensure higher confidence in experimental results. Another reason is that the linear damping ratios fitted to the mathematical model may have been greatly overestimated due to the hydraulic

machine damping. In the future, it may be necessary to characterize the damping from the machine independently. Also, the excitation was rather low; the dynamics might have been friction dominated and no explicit friction models were used in the mathematical model. Furthermore, either a random excitation experiment with an appropriate broad frequency bandwidth or a set of experiments with a more comprehensive set of frequencies which cover a broad bandwidth may lead to different fitted mathematical models. As an example, the work in Chapter 4 included the fitting of a FRF model using data from a sine sweep experiment. In this case, the damping ratio value that was fitted to the FRF model, albeit an almost perfect fit, was very different than fitted in the optimization routine involving the random excitation over a long runtime; as a reminder, the latter was based on fitting mean-square values between specified frequency bands. It is the opinion of the author, that this inconsistency in fitted damping ratio values may be due to the fact that complicated nonlinearities such as ball screw damping were not present in the assumed modeled. As such, the best fit to the approximate mathematical model may be more accurate when the excitation is close to that of real operation or when it is fit with the use of mean square quantities such as was done in Chapter 4. In future work, it might serve useful to add nonlinear dynamics associated with the ball screw to the mathematical model and/or implement random excitation and characterize the system in a manner similar to how it was done in Chapter 4. Lastly, the ability to perform an experiment with random excitation which is consistent with the simulation will add incredible value to the simulation results in the future.

BIBLIOGRAPHY

- [1] Smith, M. C., 2020. "The inerter: A retrospective". Annual Review of Control, Robotics, and Autonomous Systems, 3, pp. 361–391.
- [2] Masana, R., and Daqaq, M. F., 2013. "Response of duffing-type harvesters to band-limited noise". *Journal of Sound and Vibration*, 332(25), Dec., pp. 6755–6767.
- [3] Zhou, Z., Qin, W., Du, W., Zhu, P., and Liu, Q., 2019. "Improving energy harvesting from random excitation by nonlinear flexible bi-stable energy harvester with a variable potential energy function". *Mechanical Systems and Signal Processing*, **115**, pp. 162–172.
- [4] Li, X., Zhang, J., Li, R., Dai, L., Wang, W., and Yang, K., 2021. "Dynamic responses of a two-degree-of-freedom bistable electromagnetic energy harvester under filtered band-limited stochastic excitation". *Journal of Sound and Vibration*, **511**, Oct., p. 116334.
- [5] De Paula, A. S., Inman, D. J., and Savi, M. A., 2015. "Energy harvesting in a nonlinear piezomagnetoelastic beam subjected to random excitation". *Mechanical Systems and Signal Processing*, **54**, pp. 405–416.
- [6] Lan, C., and Qin, W., 2017. "Enhancing ability of harvesting energy from random vibration by decreasing the potential barrier of bistable harvester". *Mechanical Systems and Signal Processing*, **85**, Feb., pp. 71–81.
- [7] Han, Q., Xu, W., and Sun, J.-Q., 2016. "Stochastic response and bifurcation of periodically driven nonlinear oscillators by the generalized cell mapping method". *Physica A: Statistical Mechanics and Its Applications*, **458**, pp. 115–125.
- [8] Wei, W., Xu, W., and Liu, J., 2021. "Stochastic p-bifurcation analysis of a class of nonlinear markov jump systems under combined harmonic and random excitations". *Physica A: Statistical Mechanics and its Applications*, **582**, p. 126246.
- [9] International Organization for Standardization, 1995. ISO 8608:1995 Mechanical Vibration Road Surface Profiles Reporting of Measured Data. Standard.
- [10] Petromichelakis, I., Psaros, A. F., and Kougioumtzoglou, I. A., 2018. "Stochastic response determination and optimization of a class of nonlinear electromechanical energy harvesters: A Wiener path integral approach". *Probabilistic Engineering Mechanics*, 53, June, pp. 116–125.
- [11] Arnold, L., 2001. "Recent progress in stochastic bifurcation theory". In IUTAM Symposium on Nonlinearity and Stochastic Structural Dynamics, S. Narayanan and R. N. Iyengar, eds., Springer Netherlands, pp. 15–27.
- [12] Crauel, H. a., 1999. Stochastic Dynamics. New York, NY: Springer New York.
- [13] Liang, Y., and Namachchivaya, N. S., 1999. *P-Bifurcations in the Noisy Duffing-van der Pol Equation*. Springer New York, New York, NY, pp. 49–70.

- [14] Roberts, J., and Spanos, P., 2003. Random Vibration and Statistical Linearization. Dover Civil and Mechanical Engineering Series. Dover Publications.
- [15] Soong, T., and Grigoriu, M., 1993. Random Vibration of Mechanical and Structural Systems. PTR Prentice Hall.
- [16] Knobloch, E., and Wiesenfeld, K. A., 1983. "Bifurcations in fluctuating systems: The center-manifold approach". *Journal of Statistical Physics*, 33(3), Dec., pp. 611–637.
- [17] Sri Namachchivaya, N., 1990. "Stochastic bifurcation". Applied Mathematics and Computation, 38(2), pp. 101–159.
- [18] Kougioumtzoglou, I. A., and Spanos, P. D., 2014. "Nonstationary stochastic response determination of nonlinear systems: A wiener path integral formalism". *Journal of Engineering Mechanics*, **140**(9), p. 04014064.
- [19] Kougioumtzoglou, I., and Spanos, P., 2012. "An analytical Wiener path integral technique for non-stationary response determination of nonlinear oscillators". *Probabilistic Engineering Mechanics*, 28, Apr., pp. 125–131.
- [20] Kougioumtzoglou, I. A., and Spanos, P. D., 2009. "An approximate approach for non-linear system response determination under evolutionary stochastic excitation". Current Science, 97(8), pp. 1203–1211.
- [21] Ikago, K., Saito, K., and Inoue, N., 2012. "Seismic control of single-degree-of-freedom structure using tuned viscous mass damper". *Earthquake Engineering & Structural Dynamics*, **41**(3), pp. 453–474.
- [22] Wang, F.-C., Liao, M.-K., Liao, B.-H., Su, W.-J., and Chan, H.-A., 2009. "The performance improvements of train suspension systems with mechanical networks employing inerters". *Vehicle System Dynamics*, 47(7), pp. 805–830.
- [23] Marian, L., and Giaralis, A., 2014. "Optimal design of a novel tuned mass-damper—inerter (tmdi) passive vibration control configuration for stochastically support-excited structural systems". *Probabilistic Engineering Mechanics*, 38, pp. 156–164.
- [24] Hu, Y., and Chen, M. Z., 2015. "Performance evaluation for inerter-based dynamic vibration absorbers". *International Journal of Mechanical Sciences*, **99**, pp. 297–307.
- [25] Joubaneh, E. F., and Barry, O. R., 2019. "On the improvement of vibration mitigation and energy harvesting using electromagnetic vibration absorber-inerter: Exact h2 optimization". *Journal of Vibration and Acoustics*, **141**(6).
- [26] Tai, W.-C., 2020. "Optimum design of a new tuned inerter-torsional-mass-damper passive vibration control for stochastically motion-excited structures". *Journal of Vibration and Acoustics*, **142**(1).
- [27] Haxton, R. S., and Barr, A. D. S., 1972. "The autoparametric vibration absorber". Journal of Engineering for Industry, 94(1), 02, pp. 119–125.

- [28] Hatwal, H., Mallik, A., and Ghosh, A., 1982. "Non-linear vibrations of a harmonically excited autoparametric system". *Journal of Sound and Vibration*, 81(2), pp. 153–164.
- [29] Song, Y., Sato, H., Iwata, Y., and Komatsuzaki, T., 2003. "The response of a dynamic vibration absorber system with a parametrically excited pendulum". *Journal of Sound and Vibration*, **259**(4), pp. 747–759.
- [30] Warminski, J., and Kecik, K., 2009. "Instabilities in the main parametric resonance area of a mechanical system with a pendulum". *Journal of Sound and Vibration*, **322**(3), pp. 612–628.
- [31] Ibrahim, R. A., and Roberts, J. W., 1976. "Broad band random excitation of a two-degree-of-freedom system with autoparametric coupling". *Journal of Sound and Vibration*, 44(3), Feb., pp. 335–348.
- [32] Ibrahim, R. A., and Heo, H., 1986. "Autoparametric vibration of coupled beams under random support motion". *Journal of Vibration, Acoustics, Stress, and Reliability in Design*, **108**(4), 10, pp. 421–426.
- [33] Yan, Z., and Hajj, M. R., 2015. "Energy harvesting from an autoparametric vibration absorber". Smart Materials and Structures, 24(11), p. 115012.
- [34] Yan, Z., and Hajj, M. R., 2017. "Nonlinear performances of an autoparametric vibration-based piezoelastic energy harvester". *Journal of Intelligent Material Systems and Structures*, 28(2), pp. 254–271.
- [35] Kecik, K., 2018. "Assessment of energy harvesting and vibration mitigation of a pendulum dynamic absorber". *Mechanical Systems and Signal Processing*, **106**, pp. 198–209.
- [36] Felix, J. L. P., Balthazar, J. M., Rocha, R. T., Tusset, A. M., and Janzen, F. C., 2018. "On vibration mitigation and energy harvesting of a non-ideal system with autoparametric vibration absorber system". *Meccanica*, 53(13), pp. 3177–3188.
- [37] Tan, T., Yan, Z., Zou, Y., and Zhang, W., 2019. "Optimal dual-functional design for a piezoelectric autoparametric vibration absorber". *Mechanical Systems and Signal Processing*, **123**, pp. 513–532.
- [38] IEA, 2024. Quarterly electric car sales by region, 2021-2024. https://www.iea.org/data-and-statistics/charts/quarterly-electric-car-sales-by-region-2021-2024.
- [39] IEA, 2024. Global ev outlook. https://www.iea.org/reports/global-ev-outlook-2024.
- [40] International Council on Clean Transportation, 2024. Zero-emission vehicle phase-ins: Passenger cars and vans/light trucks (July 2024). https://theicct.org/zero-emission-vehicle-phase-ins-passenger-cars-and-vans-light-trucks-july-2024/.
- [41] Goldner, R., Zerigian, P., and Hull, J., 2001. "A preliminary study of energy recovery in vehicles by using regenerative magnetic shock absorbers". *SAE Technical Paper*(2001-01-2071).

- [42] Karnopp, D., 1989. "Permanent Magnet Linear Motors Used as Variable Mechanical Dampers for Vehicle Suspensions". Vehicle System Dynamics, 18(4), Jan., pp. 187–200.
- [43] Abdelkareem, M. A., Xu, L., Ali, M. K. A., Elagouz, A., Mi, J., Guo, S., Liu, Y., and Zuo, L., 2018. "Vibration energy harvesting in automotive suspension system: A detailed review". Applied Energy, 229, Nov., pp. 672–699.
- [44] Daqaq, M. F., Masana, R., Erturk, A., and Dane Quinn, D., 2014. "On the Role of Nonlinearities in Vibratory Energy Harvesting: A Critical Review and Discussion". *Applied Mechanics Reviews*, **66**(4), July, p. 040801.
- [45] Harne, R. L., and Wang, K. W., 2013. "A review of the recent research on vibration energy harvesting via bistable systems". *Smart Materials and Structures*, **22**(2), Feb., p. 023001.
- [46] Chen, C., Chan, Y. S., Zou, L., and Liao, W.-H., 2018. "Self-powered magnetorheological dampers for motorcycle suspensions". *Proceedings of the Institution of Mechanical Engineers*, Part D: Journal of Automobile Engineering, 232(7), June, pp. 921–935.
- [47] Singh, S., and Satpute, N. V., 2015. "Design and analysis of energy-harvesting shock absorber with electromagnetic and fluid damping". *Journal of Mechanical Science and Technology*, **29**(4), Apr., pp. 1591–1605.
- [48] Zuo, L., Scully, B., Shestani, J., and Zhou, Y., 2010. "Design and characterization of an electromagnetic energy harvester for vehicle suspensions". *Smart Materials and Structures*, **19**(4), Apr., p. 045003.
- [49] Jin-qiu, Z., Zhi-zhao, P., Lei, Z., and Yu, Z., 2013. "A review on energy-regenerative suspension systems for vehicles". In Proceedings of the world congress on engineering, Vol. 3, pp. 3–5.
- [50] Li, P., and Zuo, L., 2017. "Influences of the electromagnetic regenerative dampers on the vehicle suspension performance". Proceedings of the Institution of Mechanical Engineers, Part D: Journal of Automobile Engineering, 231(3), Feb., pp. 383–394.
- [51] Abdelkareem, M. A., Xu, L., Guo, X., Ali, M. K. A., Elagouz, A., Hassan, M. A., Essa, F., and Zou, J., 2018. "Energy harvesting sensitivity analysis and assessment of the potential power and full car dynamics for different road modes". Mechanical Systems and Signal Processing, 110, Sept., pp. 307–332.
- [52] Huang, B., Hsieh, C.-Y., Golnaraghi, F., and Moallem, M., 2015. "Development and optimization of an energy-regenerative suspension system under stochastic road excitation". *Journal of Sound and Vibration*, **357**, pp. 16–34.
- [53] Casavola, A., Di Iorio, F., and Tedesco, F., 2018. "A multiobjective H∞ control strategy for energy harvesting in regenerative vehicle suspension systems". *International Journal* of Control, 91(4), Apr., pp. 741–754.

- [54] Andren, P., 2006. "Power spectral density approximations of longitudinal road profiles". *International Journal of Vehicle Design*, **40**(1-3), pp. 2–14.
- [55] Li, M., Liu, D., and Li, J., 2023. "Stochastic analysis of vibro-impact bistable energy harvester system under colored noise". *Nonlinear Dynamics*, **111**(18), July, pp. 17007–17020.
- [56] He, Q., and Daqaq, M. F., 2015. "New Insights Into Utilizing Bistability for Energy Harvesting Under White Noise". Journal of Vibration and Acoustics, 137(2), Apr., p. 021009.
- [57] Mirzakhalili, E., and Epureanu, B. I., 2019. "Probabilistic Analysis of Bifurcations in Stochastic Nonlinear Dynamical Systems". *Journal of Computational and Nonlinear Dynamics*, 14(8), 06, p. 081009.
- [58] Cosner, J. A., and Tai, W.-C., 2023. "P-Bifurcation Analysis of a Quarter-Car Model With Inerter-Based Pendulum Vibration Absorber: A Wiener Path Integration Approach". *Journal of Computational and Nonlinear Dynamics*, 19(2), 12, p. 021004.
- [59] Daqaq, M. F., 2012. "On intentional introduction of stiffness nonlinearities for energy harvesting under white Gaussian excitations". Nonlinear Dynamics, 69(3), Aug., pp. 1063–1079.
- [60] Cosner, J. A., and Tai, W.-C., 2022. "Stochastic bifurcation and energy transfer in an inerter-based pendulum vibration absorber". *Journal of Computational and Nonlinear Dynamics*, 17(8), p. 081003.
- [61] Psaros, A. F., Kougioumtzoglou, I. A., and Petromichelakis, I., 2018. "Sparse representations and compressive sampling for enhancing the computational efficiency of the Wiener path integral technique". Mechanical Systems and Signal Processing, 111, Oct., pp. 87–101.
- [62] Hajidavalloo, M. R., Cosner, J., Li, Z., Tai, W.-C., and Song, Z., 2022. "Simultaneous suspension control and energy harvesting through novel design and control of a new nonlinear energy harvesting shock absorber". *IEEE transactions on vehicular technology*, 71(6), pp. 6073–6087.
- [63] Li, Y., Wu, Z., Zhang, G., Wang, F., and Wang, Y., 2019. "Stochastic P-bifurcation in a bistable Van der Pol oscillator with fractional time-delay feedback under Gaussian white noise excitation". Advances in Difference Equations, 2019(1), Dec., p. 448.
- [64] Zhang, Y., Jin, Y., Xu, P., and Xiao, S., 2020. "Stochastic bifurcations in a nonlinear tri-stable energy harvester under colored noise". *Nonlinear Dynamics*, **99**, pp. 879–897.
- [65] Xu, Y., Gu, R., Zhang, H., Xu, W., and Duan, J., 2011. "Stochastic bifurcations in a bistable duffing—van der pol oscillator with colored noise". *Physical Review E*, **83**(5), p. 056215.

- [66] Kumar, P., Narayanan, S., and Gupta, S., 2017. "Bifurcation analysis of a stochastically excited vibro-impact duffing-van der pol oscillator with bilateral rigid barriers". *International Journal of Mechanical Sciences*, 127, pp. 103–117.
- [67] Sun, Y.-H., Sun, Y., Yang, Y.-G., and Xu, W., 2023. "Bifurcation and stability analysis of a hybrid energy harvester with fractional-order proportional-integral-derivative controller and Gaussian white noise excitations". *Probabilistic Engineering Mechanics*, 73, July, p. 103464.
- [68] Cai, Q., and Zhu, S., 2022. "The nexus between vibration-based energy harvesting and structural vibration control: A comprehensive review". Renewable and Sustainable Energy Reviews, 155, Mar., p. 111920.
- [69] Vakakis, A. F., 2001. "Inducing Passive Nonlinear Energy Sinks in Vibrating Systems". Journal of Vibration and Acoustics, 123(3), July, pp. 324–332.
- [70] Xue, J.-R., Zhang, Y.-W., Niu, M.-Q., and Chen, L.-Q., 2023. "Harvesting electricity from random vibrations *via* a nonlinear energy sink". *Journal of Vibration and Control*, **29**(23-24), Dec., pp. 5398–5412.
- [71] Kumar, P., Narayanan, S., and Gupta, S., 2016. "Investigations on the bifurcation of a noisy duffing—van der pol oscillator". *Probabilistic Engineering Mechanics*, 45, pp. 70–86.
- [72] Zhou, S., Cao, J., Inman, D. J., Lin, J., Liu, S., and Wang, Z., 2014. "Broadband tristable energy harvester: Modeling and experiment verification". *Applied Energy*, 133, Nov., pp. 33–39.
- [73] Zhang, T., and Jin, Y., 2024. "An improved coupled tri-stable energy harvesting system with spring stops for passive control". Communications in Nonlinear Science and Numerical Simulation, 135, Aug., p. 108050.
- [74] Zhou, Z., Qin, W., and Zhu, P., 2017. "A broadband quad-stable energy harvester and its advantages over bi-stable harvester: Simulation and experiment verification". *Mechanical Systems and Signal Processing*, 84, Feb., pp. 158–168.
- [75] Daqaq, M. F., 2011. "Transduction of a bistable inductive generator driven by white and exponentially correlated Gaussian noise". *Journal of Sound and Vibration*, **330**(11), May, pp. 2554–2564.
- [76] Sharif-Bakhtiar, M., and Shaw, S. W., 1992. "Effects of nonlinearities and damping on the dynamic response of a centrifugal pendulum vibration absorber". *Journal of Vibration and Acoustics*, 114(3), 07, pp. 305–311.
- [77] Huang, Z., Zhu, W., and Suzuki, Y., 2000. "Stochastic averaging of strongly non-linear oscillators under combined harmonic and white-noise excitations". *Journal of Sound and Vibration*, 238(2), pp. 233–256.

- [78] Soong, T. T., and Grigoriu, M., 1993. "Random vibration of mechanical and structural systems". NASA STI/Recon Technical Report A, 93, Jan., p. 14690.
- [79] Namachchivaya, N. S., 1990. "Stochastic bifurcation". Applied Mathematics and Computation, 38(2), pp. 101–159.
- [80] Bover, D., 1978. "Moment equation methods for nonlinear stochastic systems". *Journal of Mathematical Analysis and Applications*, **65**(2), Sept., pp. 306–320.
- [81] Higgins, B. G., and Binous, H., 2010. "A Simple Method for Tracking Turning Points in Parameter Space". *JOURNAL OF CHEMICAL ENGINEERING OF JAPAN*, **43**(12), pp. 1035–1042.
- [82] Sun, J.-Q., and Hsu, C. S. "Cumulant-neglect closure method for nonlinear systems under random excitations". pp. 649–655.
- [83] Wojtkiewicz, S., Spencer Jr, B., and Bergman, L., 1996. "On the cumulant-neglect closure method in stochastic dynamics". *International journal of non-linear mechanics*, 31(5), pp. 657–684.
- [84] Kecik, K., and Borowiec, M., 2013. "An autoparametric energy harvester". *The European Physical Journal Special Topics*, **222**(7), pp. 1597–1605.
- [85] Okada, Y., 2002. "Variable resistance type energy regenerative damper using pulse width modulated step-up chopper". J. Vib. Acoust, 14, pp. 110–115.
- [86] Zuo, L., and Zhang, P.-S., 2013. "Energy Harvesting, Ride Comfort, and Road Handling of Regenerative Vehicle Suspensions". *Journal of Vibration and Acoustics*, 135(1), Feb., p. 011002.
- [87] Psaros, A. F., and Kougioumtzoglou, I. A., 2020. "Functional series expansions and quadratic approximations for enhancing the accuracy of the wiener path integral technique". *Journal of Engineering Mechanics*, **146**(7), p. 04020065.
- [88] Petromichelakis, I., Psaros, A. F., and Kougioumtzoglou, I. A., 2020. "Stochastic response determination of nonlinear structural systems with singular diffusion matrices: A Wiener path integral variational formulation with constraints". *Probabilistic Engineering Mechanics*, 60, Apr., p. 103044.
- [89] Kougioumtzoglou, I. A., Di Matteo, A., Spanos, P. D., Pirrotta, A., and Di Paola, M., 2015. "An efficient wiener path integral technique formulation for stochastic response determination of nonlinear mdof systems". *Journal of Applied Mechanics*, 82(10), p. 101005.
- [90] Sundararajan, P., and Noah, S. T., 1997. "Dynamics of Forced Nonlinear Systems Using Shooting/Arc-Length Continuation Method—Application to Rotor Systems". *Journal of Vibration and Acoustics*, 119(1), 01, pp. 9–20.

- [91] Li, Z., Zuo, L., Luhrs, G., Lin, L., and Qin, Y.-x., 2013. "Electromagnetic Energy-Harvesting Shock Absorbers: Design, Modeling, and Road Tests". *IEEE Transactions on Vehicular Technology*, **62**(3), Mar., pp. 1065–1074.
- [92] Huang, B., Hsieh, C.-Y., Golnaraghi, F., and Moallem, M., 2015. "Development and optimization of an energy-regenerative suspension system under stochastic road excitation". *Journal of Sound and Vibration*, **357**, pp. 16–34.
- [93] Liu, X., Li, Y., Cheng, Y., and Cai, Y., 2023. "Sparse identification for ball-screw drives considering position-dependent dynamics and nonlinear friction". *Robotics and Computer-Integrated Manufacturing*, **81**, June, p. 102486.
- [94] Bowen, L., Vinolas, J., and Olazagoitia, J. L., 2019. "The influence of friction parameters in a ball-screw energy-harvesting shock absorber". *Nonlinear Dynamics*, **96**(4), June, pp. 2241–2256.
- [95] González, A., Olazagoitia, J. L., Viñolas, J., Ulacia, I., and Izquierdo, M., 2022. "An innovative energy harvesting shock absorber system for motorbikes". *IEEE/ASME Transactions on Mechatronics*, **27**(5), pp. 3110–3120.

APPENDIX A: DRIFT AND DIFFUSION COMPONENTS OF MOMENT EQUATIONS

The third and fourth components of the drift vector in (4.15) were derived and are given here.

$$a_{3} = \frac{(\eta + \cos(\psi)) \left(2\dot{\phi}\xi_{p} + \eta\dot{\theta}^{2}\mu_{r}\sin(\psi)\right)}{A} \\ - \frac{\eta \left(\theta + 2\dot{\theta}\left(\xi - \eta\dot{\phi}\mu_{r}\sin(\psi)\right) - \eta\dot{\phi}^{2}\mu_{r}\sin(\psi)\right)}{A} \\ a_{4} = (-\mu_{r}\eta A)^{-1} \left[2\dot{\phi}\xi_{p} + 2\eta^{2}\dot{\phi}\xi_{p}\mu_{r} + 4\eta\dot{\phi}\xi_{p}\mu_{r}\cos(\psi) + 2\dot{\phi}\xi_{p}\mu_{r} - 2\eta^{2}\dot{\theta}\xi\mu_{r} + \eta^{3}\dot{\theta}^{2}\mu_{r}^{2}\sin(\psi) + 2\eta^{3}\dot{\theta}\dot{\phi}\mu_{r}^{2}\sin(\psi) + \eta^{2}\dot{\theta}^{2}\mu_{r}^{2}\sin(2(\psi)) + \eta^{2}\dot{\theta}\dot{\phi}\mu_{r}^{2}\sin(2(\psi)) + \eta^{3}\dot{\phi}^{2}\mu_{r}^{2}\sin(\psi) - 2\eta\dot{\theta}\xi\mu_{r}\cos(\psi) + \eta^{2}\dot{\phi}^{2}\mu_{r}^{2}\sin(\psi)\cos(\psi) + \eta\dot{\theta}^{2}\mu_{r}^{2}\sin(\psi) - \eta\theta\mu_{r}(\eta + \cos(\psi))\right](A.1)$$

where $A = -\eta (\mu_r \cos^2 (\psi) - \mu_r - 1)$. The drift vector, **a**, is then given by

$$\mathbf{a} = \begin{pmatrix} \dot{\theta} \\ \dot{\phi} \\ a_3 \\ a_4 \end{pmatrix} \tag{A.2}$$

Likewise, Σ in (4.15) is a 4 × 1 diffusion matrix consisting of the stochastic components of the system. It is found by collecting coefficients of W and multiplying by the standard deviation, σ , of the white noise. Namely, $\sigma = \sqrt{2D}$, where D is the intensity of the white noise; that is,

$$\Sigma = \begin{pmatrix} 0 \\ 0 \\ \frac{\sigma}{\mu_r \sin^2(\psi) + 1} \\ -\frac{\sigma(\eta + \cos(\psi))}{\eta + \eta \mu_r \sin^2(\psi)} \end{pmatrix}$$
(A.3)

Eqn. (4.14) can then be integrated numerically with appropriate solvers to generate realizations in the time domain.

APPENDIX B: CLOSURE TECHNIQUES

B.1 Gaussian Closure

The generated moment equations (2.12) are dependent on moments of higher order than n=2. One course of action is to use a technique called Gaussian Closure in order to relate the higher order moments to moments of first and second order in order to "close" the system. We more precisely assume

$$\langle y_{i}y_{j}y_{k}y_{l}\rangle \simeq -2 \langle y_{i}\rangle \langle y_{j}\rangle \langle y_{k}\rangle \langle y_{l}\rangle + \langle y_{i}y_{l}\rangle \langle y_{j}y_{k}\rangle$$

$$+ \langle y_{i}y_{k}\rangle \langle y_{j}y_{l}\rangle + \langle y_{i}y_{j}\rangle \langle y_{k}y_{l}\rangle$$

$$\langle y_{i}y_{j}y_{k}\rangle \simeq \langle y_{i}\rangle \langle y_{l}\rangle \langle y_{j}y_{k}\rangle - 2 \langle y_{i}\rangle \langle y_{j}\rangle \langle y_{k}\rangle + \langle y_{k}\rangle \langle y_{i}y_{j}\rangle$$

$$+ \langle y_{j}\rangle \langle y_{i}y_{k}\rangle$$
(B.1)

Substituting (B.1) into (2.12) leads to a set of fourteen nonlinear equations coupled through first and second-order moments.

B.2 Cumulant neglect

For the computation of mean-squares, a cumulant neglect procedure was used to derive stationary moment equations with moments $m_{pqrs} = \langle y_1^p y_2^q y_3^r y_4^s \rangle$ up to order n = 4. We accomplish this by first writing the characteristic function $F_{\mathbf{y}}(\mathbf{u})$ in terms of cumulants $\lambda_k(p,q,r,s)$ of order k. Specifically,

$$F_{\mathbf{y}}(\mathbf{u}) = \exp\left(\sum_{k=1}^{\infty} \frac{i^k}{k!} \sum_{p,q,r,s=1}^{n} \lambda_k(p,q,r,s) u_1^p u_2^q u_3^r u_4^s\right)$$
(B.2)

where $i = \sqrt{-1}$ and p + q + r + s = k. Moments m_{pqrs} are then related to the characteristic function by

$$m_{pqrs} = (-i)^{\zeta} \left[\frac{\partial^{\zeta} F_{\mathbf{y}}(\mathbf{u})}{\partial u_{1}^{p} \partial u_{2}^{q} \partial u_{3}^{r} \partial u_{4}^{s}} \right]_{\mathbf{u} = \mathbf{0}}$$
(B.3)

where $\zeta = p + q + r + s$. We can then set cumulant orders $\lambda_k = 0$ for k > 4 allowing us to establish a set of equations relating moments of fifth order and higher to lower orders. The

resultant relationships and (2.18) are substituted back into stationary moment equations (2.12), giving 69 algebraic equations.

APPENDIX C: LINEAR SYSTEM RESPONSE

In order to quantify the vibration suppression imposed by the IPVA, the closed form solution for the system without the IPVA is derived. The moment differential equations are used to determine the solution for the mean square velocity. The equation of motion for the linear system is given by

$$\theta'_l = \Omega$$

$$\Omega' = W - 2\hat{\xi}\Omega - \theta_l$$
 (C.1)

Additionally, the white noise input follows a Gaussian distribution with covariance matrix

$$\Sigma \Sigma^{\mathrm{T}} = \begin{pmatrix} 0 & 0 \\ 0 & \sigma^2 \end{pmatrix} \tag{C.2}$$

Lastly, from (C.1), the drift components are

$$\alpha_1 = \Omega$$

$$\alpha_2 = -2\hat{\xi}\Omega - \theta_l \tag{C.3}$$

One can finally input (C.2) and (C.3) into (2.12) to obtain the closed-form solution for the dimensionless mean square velocity given here.

$$\left\langle \theta_l^{\prime 2} \right\rangle = \frac{D}{2\hat{\xi}} \tag{C.4}$$

APPENDIX D: LINEAR SYSTEM RHI ANALYTICAL SOLUTION

In this section, the closed-form linear system solution for the road handling index is derived using power spectral density integration. To this end, the tire displacement $R(\psi_{us} - \psi_r)$ is transformed into the frequency domain, and the ratio of tire displacement to dimensionless input road velocity is determined. Note that for the remainder of this section, we will set $\hat{\omega} = \omega/\omega_0$. Then,

$$\frac{R(\psi_{us}(\hat{\omega}) - \Psi_r(\hat{\omega}))}{\Psi_r'(\hat{\omega})} = R \frac{N_1 + N_2 + N_3}{D_1 + D_2 + D_3 + D_4 + D_5},$$
 (D.1)

with

$$\begin{split} N_1 &= (-iu - i)\,\hat{\omega}, \\ N_2 &= \hat{\omega}^2 \left(2u\xi + 2u\xi_e + 2\xi + 2\xi_e\right), \\ N_3 &= \hat{\omega}^3 \left(i\eta^2\mu_r + 2i\eta\mu_r + i\mu_g + i\mu_r + i\eta^2\mu_r u + 2i\eta\mu_r u + i\mu_g u + i\mu_r u + iu\right), \\ D_1 &= uv^2, \\ D_2 &= \hat{\omega} \left(2iuv^2\xi + 2iuv^2\xi_e\right), \\ D_3 &= \hat{\omega}^2 \left(-\eta^2\mu_r uv^2 - 2\eta\mu_r uv^2 - \mu_g uv^2 - \mu_r uv^2 - uv^2 - u - 1\right), \\ D_4 &= \hat{\omega}^3 \left(-2iu\xi - 2iu\xi_e - 2i\xi - 2i\xi_e\right), \\ D_5 &= \hat{\omega}^4 \left(\eta^2\mu_r + 2\eta\mu_r + \mu_g + \mu_r + \eta^2\mu_r u + 2\eta\mu_r u + \mu_g u + \mu_r u + u\right) \end{split}$$

with $i = \sqrt{-1}$. Then using the dimensionless power spectral density of the road velocity as $S_{\Psi'_r} = d$ with the principle of H_2 norm and integration formula from [14], the road handling index becomes

$$\gamma_{RHI} = \frac{R}{g\left(M_s + M_{us}\right)} \sqrt{\frac{1}{2\pi} \int_{-\infty}^{\infty} d\left| \frac{\left(\psi_{us}\left(\hat{\omega}\right) - \Psi_r\left(\hat{\omega}\right)\right)}{\Psi_r'(\hat{\omega})} \right|^2 d\hat{\omega}}$$
(D.2)

Finally,

$$\gamma_{RHI} = \frac{R}{g(M_s + M_{us})} \left[\frac{1}{4u^2v^4(\xi + \xi_e)} \left(1 + u(3 + v^2(4(\xi + \xi_e)^2 - 2\mu_g - 2(1 + \eta)^2\mu_r)) + u^2(3 + 2v^2(-1 + 4(\xi + \xi_e)^2 - 2\mu_g - 2(1 + \eta)^2\mu_r) \right) \right]$$

+
$$v^4(\mu_g + (1+\eta)^2\mu_r)(1+\mu_g + (1+\eta)^2\mu_r))$$

+ $u^3(1+v^4(1+\mu_g + (1+\eta)^2\mu_r)^2$
+ $v^2(4(\xi+\xi_e)^2 - 2(1+\mu_g + (1+\eta)^2\mu_r)))$] $^{\frac{1}{2}}$ (D.3)

APPENDIX E: DAMPING AND FRICTION FITTING IN THE TIME DOMAIN FOR THE SDOF SYSTEM EXPERIMENT

Pendulum bearing damping c_p was also determined using a fitting procedure, but this time in the time domain. To do this, the gears were removed and the pendulums were simply given an initial velocity while keeping the carrier fixed and the time response was measured. The equation of motion for the pendulums in this case is

$$(J_{pendulum})\ddot{\psi} + c_p\dot{\psi} = 0 \tag{E.1}$$

where $J_{pendulum}$ is the pendulum's principal moment of inertia about the pivot point of the pendulums. For simplicity, only the pendulum vertical shafts were used in the experiment and then $J_{pendulum}$ was equal to the moment of inertia of the vertical shaft about its vertical axis. The equation used for fitting with MATLAB was then

$$\dot{\psi}(t) = \dot{\psi}(0) \exp\left[-\frac{c_p t}{(J_{pendulum})}\right]$$
 (E.2)

A similar experiment was done for the generator mechanical damping c_{gm} . This time the generator and sun gear were disconnected from the prototype and a time response to an initial condition was measured. The solution in this case is

$$\dot{\psi}_g(t) = \dot{\psi}_g(0) \exp\left[-\frac{c_{gm}t}{n_g^2 J_r + J_{pg}}\right]$$
 (E.3)

Finally, with pendulums and planetary gear reattached and the carrier held fixed, the same experiment was done to determine the friction term T_f . The EOM in this case is given by

$$(2J_{pg} + J_{sg} + n_g^2 J_r + 2J_{pendulum}) \ddot{\psi} + (c_p + c_{gm}) \dot{\psi} = -T_f \frac{\psi}{|\dot{\psi}|}$$
 (E.4)

For a monotonically decreasing $\dot{\psi}$, the solution to (E.4) is then

$$\dot{\psi}(t) = \left(\frac{T_f}{(c_p + c_{gm})} + \dot{\psi}(0)\right) \exp\left[-\frac{(c_p + c_{gm})t}{(J_{total})}\right] - \frac{T_f}{(c_p + c_{gm})}$$
(E.5)

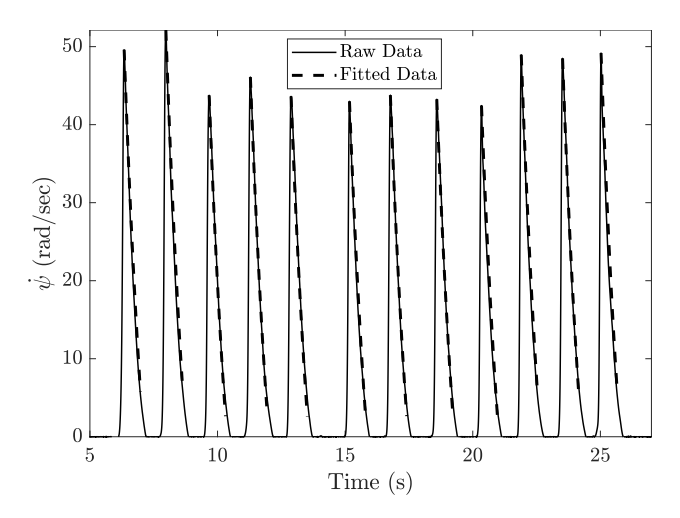


Figure E.1 Raw data for twelve sequential experiments (solid line). Fit based on (E.5) (dashed line).

with

$$J_{total} = 2J_{pg} + J_{sg} + n_g^2 J_r + 2J_{pendulum}$$

Twelve sequential experiments of this kind were done to accommodate potential variability in the data and the resultant mean fit using (E.5) is shown in Fig. E.1.

Finally, fitted parameters and measured parameters used in this work are given in Table E.1. Note that μ_r was measured directly and SolidWorks was used to compute μ_p as well as η . Note that ξ_p was determined to be negligible and was set to zero.

| Dimensionless Parameters | Value |
|--|-------|
| μ_r | 2.43 |
| $\mid \eta \mid$ | 0.45 |
| μ_p | 0.38 |
| $egin{array}{c} \mu_p \ \mu_g \ \xi \end{array}$ | 0.28 |
| $ \xi $ | 0.063 |
| $ \xi_{gm} $ | 0.004 |
| α | 5.93 |
| \hat{T}_f | 0.004 |

Table E.1 Dimensionless Parameters of Experimental IPVA system.